Doctoral Dissertation

Study on Malabaricone C Isolated From the Mace of *Myristica fragrans* as Natural Antiviral Against SARS-CoV-2 and Discovery of Its Mechanism of Actions

（香辛料由来マラバリコーン C による SARS-CoV-2 感染阻害とその機構解明）

MUTMAINAH

Graduate School of Life Science, Hokkaido University

2025 March

Table of Contents

Abbreviation **3**

Thesis Abstract **4**

Chapter 1 Introduction **5**

1.1 SARS-CoV-2 *6*

1.2 Lipid Raft *8*

1.3 Sphingomyelin Synthase (SMS) *10*

1.4 Natural Products as Antiviral Agents *14*

1.5 References *15*

Chapter 2 Discovery of Malabaricone C as SARS-CoV-2 Inhibitor from Spices **20**

2.1 Abstract *21*

2.2 Introduction *21*

2.3 Results and Discussion *24*

2.4 Conclusion *31*

2.5 Experimental Section *31*

2.6 References *78*

Chapter 3 The Discovery of the Mechanism of Malabaricone C as an Antiviral for SARS-CoV-2 **82**

3.1. Abstract *83*

3.2. Introduction *83*

3.3. Results and Discussion *85*

3.4. Conclusion *90*

3.5. Experimental Section *91*

3.6. References *93*

Acknowledgement **97**

Publications **98**

Abbreviation

ACE2: angiotensin-converting enzyme 2

AD: Alzheimer's disease

$CHCl_3$: chloroform

CC_{50}: cytotoxic concentration 50%

COVID-19 : coronavirus disease 2019

EC_{50}: half maximal effective concentration

EtOAc: ethyl acetate

GA: ginkgolic acid

HEK293T: human embryonic kidney cell line

HMPA: hexamethylphosphoramide

HPLC: high-performance liquid chromatography

HRMS: high-resolution mass spectrometry

IBX: 2-iodoxybenzoic acid

IC_{50}: half maximal inhibitory concentration

LDA: lithium diisopropylamide

MeOH: methanol

NMR: nuclear magnetic resonance

Pd/C: palladium on carbon

pTsOH: p-Toluenesulfonic acid

RBD: receptor binding domain

SAR: structural activity relationship

SARS-CoV-2: several acute respiratory syndrome coronavirus 2

SM: sphingomyelin

SMS: sphingomyelin synthase

TBAF: tetra-N-butyl ammonium fluoride

$TCID_{50}$: 50% tissue culture infectious dose

THF: tetrahydrofuran

TLC: thin layer chromatography

TMPRSS2: transmembrane protease serine 2

Thesis Abstract

SARS-CoV-2, or Severe Acute Respiratory Syndrome-Coronavirus-2, is an enveloped beta coronavirus responsible for a global health crisis. The disease it causes, COVID-19, manifests respiratory symptoms such as cough, fever, and severe pneumonia, which can result in death. Similar to its predecessor, SARS-CoV-1, which occurred two decades earlier, this novel coronavirus invades human cells by attaching its spike protein to Angiotensin-Converting Enzyme-2 (ACE2) receptors. However, while SARS-CoV-1 uses endocytosis to enter host cells, SARS-CoV-2 favors a route through transmembrane serine protease 2 (TMPRSS2)-mediated membrane fusion. Although new vaccines and antiviral drugs have been created to combat SARS-CoV-2, the need for additional COVID-19 treatments remains due to limited options. From a safety perspective, bioactive compounds from foods and edible plants present potential and challenges as new therapeutic agents against SARS-CoV-2. This study highlights the efficacy of malabaricone C, a naturally occurring compound, along with its synthetic derivatives, in inhibiting SARS-CoV-2 infection. The first chapter introduces SARS-CoV-2 and recent treatment advancements, including a review of natural antiviral agents and their mechanisms for inhibiting infections.

The second chapter centers on malabaricone C, a compound derived from nutmeg, identifying it as a novel natural inhibitor of SARS-CoV-2. Malabaricone C and its derivatives demonstrated an EC_{50} range of 1–1.5 μM against SARS-CoV-2 and its variants in mammalian cells, indicating its potential as a safe therapeutic candidate for treating and preventing COVID-19. Additionally, the chapter will present a novel method for visualizing virus-assisted cell fusion.

The third chapter explores various possible mechanisms for malabaricone C inhibiting SARS-CoV-2 infection in vitro. Potential targets include disrupting the interaction between Spike RBD and ACE2, inhibiting TMPRSS2, and interfering with lipid raft assembly on the cell membrane. This study suggests that malabaricone C inhibits SARS-CoV-2 entry primarily by affecting lipid raft assembly in the host cell membrane.

Chapter 1

Introduction

1.1 SARS-CoV-2

Structure and Characteristics of SARS-CoV-2

Severe Acute Respiratory Syndrome Coronavirus 2 (SARS-CoV-2), the virus responsible for the COVID-19 outbreak, is a member of the Coronaviridae family and is classified as a beta-coronavirus. The virus is characterized by a single-stranded RNA genome that ranges from approximately 29.9 kb in length, which encodes several structural and non-structural proteins essential for its replication and pathogenicity[1]. The primary structural proteins include the spike (S) protein, envelope (E) protein, membrane (M) protein, and nucleocapsid (N) protein (Figure 1)[2]. The spike protein, in particular, serves a critical function in the virus's entry into host cells by binding to the Angiotensin-Converting Enzyme 2 (ACE2) receptor, a mechanism that is enhanced by host proteases such as TMPRSS2[3].

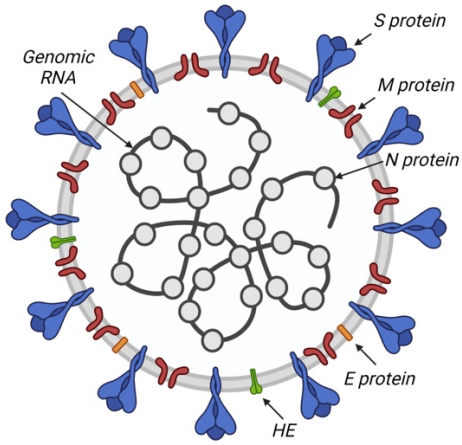

Figure 1. Coronavirus structure: S, E, M, N proteins and genomic RNA are indicated

The spike protein is a trimeric glycoprotein that protrudes from the viral envelope, giving the virus its crown-like appearance when viewed under electron microscopy[4]. The S protein consists of two functional subunits: S1, which contains the receptor-binding domain (RBD), and S2, responsible for membrane fusion. Various strains of SARS-CoV-2 have emerged, displaying modifications in the RBD that could enhance their ability to bind to ACE2. This may result in increased transmission rates and could impact the effectiveness of vaccines[5]. Grasping these structural changes is essential for the development of vaccines and treatment strategies.

The viral envelope and its structural proteins are crucial to the virus's stability and infection capability. The E and M proteins are essential for assembling and releasing new virions. In contrast, the N protein is critical for encapsulating the viral RNA, forming a nucleocapsid that protects the genetic material[6]. The encapsidation preserves the stability of the viral RNA and is essential to the virus's life cycle. In addition, the lipid bilayer, which comes from the host cell membrane, creates a protective shield in the budding process during viral replication.

Virus-Host Cell Interaction

The interaction between SARS-CoV-2 and host cells is fundamental to the virus's ability to establish infection and propagate. The process begins with the S protein of SARS-CoV-2, which binds to the ACE2 receptor in human cells, particularly those in the respiratory tract[3]. This initial attachment is facilitated by the protease TMPRSS2, which cleaves the S protein, enabling the virus to enter the host cell through membrane fusion or endocytosis[1]. Figure 2 shows the fusion pathways of SARS-CoV-2 through the host cell.

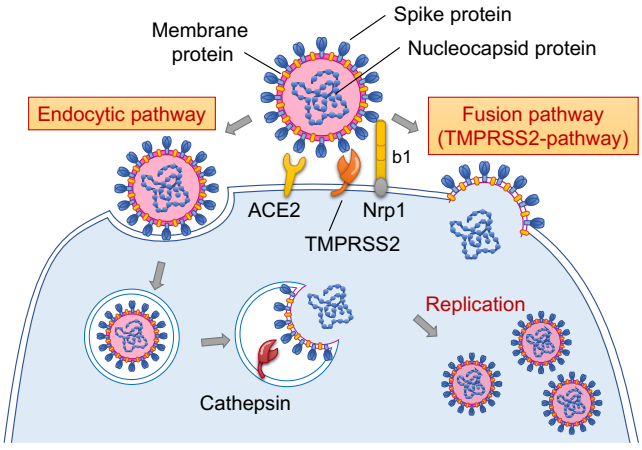

Figure 2. Fusion of SARS-CoV-2 occurs through endocytic and fusion pathways

Once inside the host cell, the viral RNA is released into the cytoplasm, synthesizing viral proteins and genome replication. The virus utilizes the host's ribosomes, endoplasmic reticulum, and Golgi apparatus to produce its components, highlighting its dependence on the host cellular machinery for proliferation[7]. The viral

proteins can also disrupt normal cellular functions, including immune signaling pathways, thereby hindering the host's antiviral defenses[8]. As a result, this interaction supports viral replication and contributes to the pathogenesis of COVID-19, causing severe inflammatory responses in infected individuals.

1.2 Lipid Raft

Lipid rafts are specialized microdomains within cellular membranes that play a critical role in various biological processes. Composed of a unique composition of cholesterol, sphingolipids, and proteins, these rafts are thought to facilitate the organization of signaling molecules, thereby enhancing cellular communication and signaling pathways. Lipid rafts are typically enriched in saturated fatty acids and exhibit a more ordered structure than the surrounding membrane. This distinct composition allows lipid rafts to serve as platforms for the clustering of signaling receptors, guanine nucleotide-binding (G) proteins, and other membrane-associated proteins, which can lead to the activation of intracellular signaling cascades[9]. Additionally, lipid rafts are implicated in processes such as endocytosis, exocytosis, and pathogen entry into cells, making them essential for maintaining cellular homeostasis and responding to external stimuli.

Recent studies have highlighted the significance of lipid rafts in the context of various diseases, including cancer and infectious diseases. For instance, lipid rafts have been linked to cancer cell proliferation and metastasis, as many growth factor receptors and signaling molecules reside within these microdomains[10]. Furthermore, lipid rafts are critical for the entry of specific pathogens, such as viruses and bacteria, into host cells. For example, studies have shown that HIV and SARS-CoV2 utilize lipid raft domains to facilitate their infection process[11,12].

Both SARS-CoV and SARS-CoV-2 have the capability for cell-to-cell transmission, which allows the virus to avoid contact with antibodies[13,14]. This transmission occurs through the formation of channels or syncytia and relies on intact lipid rafts[15]. Consequently, at least four stages of the SARS-CoV-2 lifecycle—initial binding, activation, internalization, and cell-to-cell transmission—depend on functional host lipid rafts (Figure 3)[16]. This indicates that targeting host lipid rafts may

be a promising approach to reduce the infectivity of SARS-CoV-2, a strategy that has been experimentally confirmed in vitro for SARS-CoV[17].

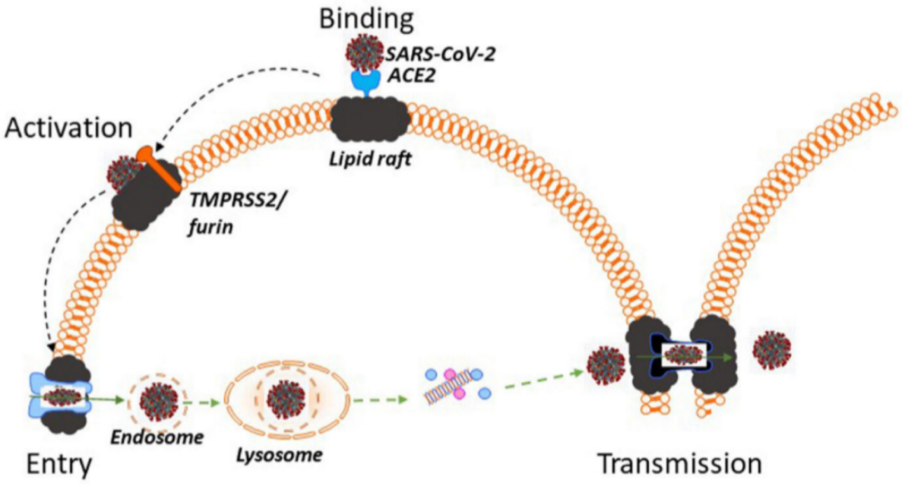

Figure 3. Lipid rafts and pathogenesis of SARS-CoV-2

The molecular pathogenesis of SARS-CoV-2 is schematically presented in Figure 3. SARS-CoV-2 attaches to ACE2, a protein associated with lipid rafts. Following this binding, the S protein within the viral envelope undergoes enzymatic activation by TMPRSS2 or furin, likely located in lipid rafts. The endocytosis of SARS-CoV-2 follows this via a raft-dependent endocytic pathway. Once inside the cell, SARS-CoV-2 experiences intracellular trafficking within endosomes, fuses with mature lysosomes, and releases its viral RNA genome into the host cytoplasm. One route of virus transmission, known as cell-to-cell transmission, occurs through the formation of intercellular channels or syncytia and necessitates intact lipid rafts. Therefore, at least four stages of the SARS-CoV-2 lifecycle—initial binding, activation, internalization, and cell-to-cell transmission—require intact host rafts to proceed. If other viruses are any indication, disrupting lipid rafts through lipid raft therapy may help mitigate the infection[16].

Lipid rafts affecting drugs, alone or in combination with other compounds, may play a role in antiviral activity. Barman and Nayak[18] demonstrated that lipid raft disruption by MβCD-mediated cholesterol depletion is able to reduce influenza virus infectivity. In addition, cholesterol depletion on the host plasma membrane makes it less vulnerable to influenza virus infection[19]. Overall, the study of lipid rafts continues

to evolve, revealing their multifaceted roles in cellular function and disease progression.

1.3 Sphingomyelin Synthase (SMS)

Sphingomyelin synthases (SMS) are crucial enzymes responsible for the biosynthesis of sphingomyelin, a significant component of cell membranes that play key roles in cell signaling, membrane structure, and lipid metabolism. These enzymes catalyze the transfer of a phosphocholine head group to ceramide, forming sphingomyelin[20]. Sphingomyelin synthases, specifically the isoforms SMS1, SMS2, and SMS-related protein (SMSr), are essential enzymes responsible for the biosynthesis of sphingomyelin and ceramide phosphoethanolamine, components crucial for cell membrane integrity and lipid metabolism. SMS1 is mainly expressed in the liver, where it synthesizes sphingomyelin from long-chain ceramides. In contrast, SMS2 is distributed across a wider range of tissues and helps maintain membrane dynamics. Although SMSr does not have sphingomyelin synthase activity, it plays a role in regulating ceramide levels. Disruptions in SMS1, SMS2, or SMSr functions may contribute to various metabolic and neurodegenerative diseases[21]. Moreover, the differential regulation of sphingomyelin synthase isoforms highlights their potential as therapeutic targets in diseases characterized by lipid dysregulation.

SMS Related Disorders

Dysregulation of SMS activity, particularly of its isoforms (SMS1 and SMS2), has been linked to various diseases, underscoring this enzyme's importance in human health. Studies have increasingly highlighted how alterations in SMS levels and function can contribute to the pathogenesis of neurodegenerative diseases, metabolic disorders, and certain types of cancer. SMS has been involved in many disorders, especially in metabolic disorders such as obesity, insulin resistance, fatty liver formation, and type 2 diabetes[22].

SMS2 is a proposed potential therapeutic target for obesity and insulin resistance[23]. Downregulation of SMS2 activity results in protective effects against obesity, atherosclerosis and diabetes and makes SMS2 inhibitors potential medicines[24]. Mitsutake et al. found that a lack of SMS2 leads to a reduction in the formation of fatty liver. Experiments involving SMS2 knockout (KO) mice on a high-

fat diet reveal a significant decrease in fat accumulation around the liver compared to their wild-type counterparts. Additionally, SMS2 KO mice show a marked reduction in liver triglyceride levels in comparison to wild-type mice, and their triglyceride levels are similar to those of SMS2 KO mice on a normal diet[22]. The relationship between sphingolipid metabolism and metabolic health highlights the potential advantages of targeting SMS for treating metabolic diseases. Recently, malabaricone C has been identified as a natural inhibitor of sphingomyelin. Similar to previous findings involving SMS KO studies[22], malabaricone C has also been shown to help reduce body weight gain, improve glucose tolerance, and lower lipid accumulation in the liver in vivo[25].

Dysregulation of sphingomyelin and ceramide metabolism has emerged as a key factor in the pathophysiology of Alzheimer's disease (AD)[26]. A central element in this process is the accumulation of the amyloid-β (Aβ) peptide, a 42-residue protein that is believed to play a critical role in triggering the development of AD. Within the brain, the concentration of Aβ is meticulously regulated through various production and clearance mechanisms[27].

Research conducted by K. Yuyama and colleagues[28] has shown that the activity of sphingolipid-metabolizing enzymes, particularly neutral sphingomyelinase 2 (nSMase2) and SMS2, significantly influences the secretion of neuronal exosomes. In their studies, enhancing exosome secretion from neuronal cells through treatment with SMS2 siRNA resulted in increased uptake of Aβ by microglial cells, leading to a marked reduction in extracellular Aβ levels.

Furthermore, recent investigations have indicated that sphingomyelins could serve as potential biomarkers for neurodegeneration and neuroinflammation, suggesting their relevance beyond just Alzheimer's disease. This highlights the intricate interplay between sphingolipid metabolism and neurodegenerative processes, warranting further exploration in the context of AD and related conditions[29].

SMS2 plays a significant role in various processes related to sphingomyelin metabolism and is involved in inflammation, atherosclerosis, cell proliferation, apoptosis, and other biological functions. A study by Zheng et al. suggested that SMS2 promotes the proliferation and migration of breast cancer cells[30]. Additionally, SMS2 upregulates the expression of flotillin-2 and enhances the stemness of breast cancer

cells through the nuclear factor-kappa B (NF-κB) signaling pathway, resulting in increased resistance to the chemotherapeutic drug adriamycin[31].

Another study conducted by He and colleagues found that the mRNA expression of SMS 2 positively correlates with tumor-associated macrophages, the immunosuppressive microenvironment, and poor prognosis in patients with pancreatic ductal adenocarcinoma. Moreover, it was confirmed that the deficiency of SMS 2 has an inhibitory effect on the growth of orthotopic PANC-02 tumors in vivo[32].

SMS Activity and Viral Entry

The lipid composition of the host cell membrane is one of the key determinants of the entry of enveloped viruses into cells. An entry assay using pseudotyped vesicular stomatitis virus possessing rubella virus (RuV) envelope proteins revealed that sphingomyelin generated by SMSs is crucial for at least RuV entry. This indicates that sphingomyelin produced by SMSs is essential for the formation of membrane pores after hemifusion occurs during RuV entry[33]. Sphingomyelin formed by sphingomyelin synthases contributes towards the formation of pores in the host cell membrane following viral binding, aiding in the entry process[33].

Sphingomyelinase activation plays a crucial role in facilitating the pH and clathrin-dependent entry and replication of the Japanese encephalitis virus (JEV) in tissue cultures[34]. Notably, sphingomyelin synthesized by SMS1 is essential for JEV attachment and subsequent infection. Research by Taniguchi et al. (2016) revealed that a deficiency in SMS1 in mice resulted in a significant reduction of JEV infection in vivo, underscoring the importance of sphingomyelin in viral pathogenesis[35]. Furthermore, optimal membrane fusion mediated by HIV-1 gp41 has been shown to depend on the activity of SMS2. This finding suggests that the presence of sphingomyelin, rather than the accumulation of ceramide, is critical for this fusion process[36].

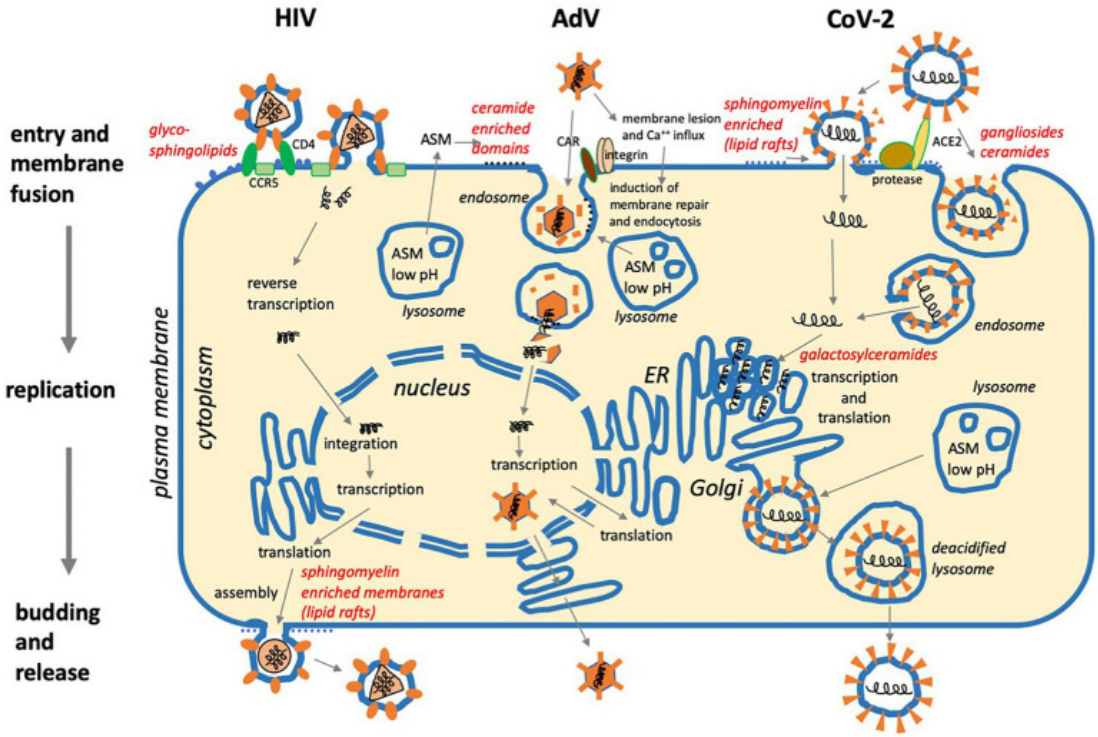

Figure 4. Three examples of viral replication cycle and involvement of sphingolipids, Human immunodeficiency virus (HIV), Adenovirus (AdV), and SARS Coronavirus 2 (SARS-CoV-2)

Three examples of viral replication cycles and the role of sphingolipids are presented in Figure 4[37]. (1) The human immunodeficiency virus (HIV) binds to glycosphingolipids, CD4, and the co-receptors CCR5 or CXCR4 before fusion occurs at the plasma membrane. After reverse transcription of its positive-strand RNA genome and integration into the host cell's DNA, the virus utilizes the cellular machinery for transcription and translation. Assembly and budding occur at the plasma membrane, involving sphingomyelin-enriched membrane domains known as lipid rafts. (2) Adenovirus (AdV) attaches to CAR and integrins, causing membrane lesions that induce Ca^{++} influx and initiate membrane repair. This process requires the involvement of lysosomes and ASM activity, which assists with viral uptake through endocytosis. Once the viral capsid disintegrates, the viral DNA is transported to the nucleus, where transcription and translation occur. Viral particles are assembled in the nucleus and eventually released. (3) SARS coronavirus-2 (CoV-2) requires protease activity and binds to ACE2, aided by sialic acid in ganglioside-rich membrane domains before cell entry through membrane fusion or endocytosis. Transcription and

translation occur on the endoplasmic reticulum's cytoplasmic face (ER). Galactosylceramide supports viral replication. After assembly, virus particles are transported to lysosomes for release via lysosomal exocytosis[37].

1.4 Natural Products as Antiviral Agents

Since ancient times, natural products have been a significant source of drugs. Newman et al. reported that, over the past 28 years, 63.1% of all small-molecule drugs developed were based on natural products[38]. These natural products hold great potential for the development of new antiviral medications due to their unique structures and wide-ranging antiviral activities. Numerous active components derived from natural products—such as alkaloids, quinones, flavonoids, terpenoids, glycans, organic acids, and others—exhibit antiviral properties[39].

In recent decades, advanced scientific research has led to the discovery of many synthetic antiviral agents effective against various viral infectious diseases. Unfortunately, these synthetic drugs often come with numerous adverse effects and can become ineffective against emerging viral-resistant strains[40]. Consequently, there has been increased interest in medicinal plants and their bioactive metabolites as potential sources of effective and affordable treatments[41]. The search for novel antiviral agents now emphasizes both synthetic combinations and plant-derived metabolites. Various plant metabolites can impede viral replication without negatively impacting host physiology or with minimal side effects[42,43]

Quercetin, a flavonoid found abundantly in fruits and vegetables, is known for its antioxidant, antiviral, antimicrobial, and anti-inflammatory properties[44]. Quercetin has demonstrated efficacy against SARS and MERS due to its various beneficial effects. It may also hold therapeutic potential against SARS-CoV-2, as it inhibits several stages of the viral life cycle[45].

During the COVID-19 pandemic, numerous natural products have been reported to possess anti-SARS-CoV-2 activities. Huang et al. found that an alkaloid compound significantly inhibited SARS-CoV-2 replication in Vero E6 cells at nanomolar concentrations, with relatively low toxicity[46]. Hesperidin, a glycoside formed from hesperetin and rhamnoglucoside, is a dihydroflavonoid derivative. Meneguzzo and colleagues suggested that Hesperidin could disrupt various stages of coronavirus

invasion and replication, demonstrating strong binding capacity to SARS-CoV-2 receptors[47]. Additionally, oral or nasal sprays containing kappa gum have been shown to inactivate SARS-CoV-2 in cultures of human airway epithelial cells[48].

1.5 References

1. Zhou, P., Yang, XL., Wang, XG., Hu, B., Zhang, L., *et al.* A pneumonia outbreak associated with a new coronavirus of probable bat origin. *Nature* **2020**, 579, 270-273.
2. Mingaleeva, RN., Nigmatulina, NA., Sharafetdinova, LM., Romozanova, AM, Gabdoulkhakova, AG., *et al*. Biology of the SARS-CoV-2 Coronavirus. *Biochemistry (Mosc)* **2022**, 87, 1662-1678.
3. Hoffmann, M., Weber, HK., Schroeder, S., Kruger, N., Herrler, T., et al. SARS-CoV-2 Cell Entry Depends on ACE2 and TMPRSS2 and Is Blocked by a Clinically Proven Protease Inhibitor. *Cell* **2020**, 181, 271-280.
4. Cai, Y., Zhang, J., XIAO, T., Lavine, C., Rawson, S., *et al*. Structural Basis for Enhanced Infectivity and Immune Evasion Of SARS-Cov-2 Variants. *Science* **2021**, 373, 642-648.
5. Huang, Y., Yang, C., Xu, XF., Xu, W., Liu, SW. Structural and functional properties of SARS-CoV-2 spike protein: potential antivirus drug development for COVID-19. *Acta Pharmacol Sin* **2020**, 41, 1141–1149.
6. Snijder, EJ., Limpens, RWAL., Wilde, AH., Jong, AWM., Maier, HJ., *et al.* A Unifying Structural and Functional Model of the Coronavirus Replication Organelle: Tracking Down RNA Synthesis. *PLOS Biol* **2020**, 18, e3000715.
7. Wu, F., Zhao, S., Yu, B., Chen, YM., Wang, W. et al. A new coronavirus associated with human respiratory disease in China. *Nature* **2020**, 579, 265–269.
8. Melo, DB., Payant, BEN., Liu,WC., Uhl,S., Hoagland, D. et al. Imbalanced Host Response to SARS-CoV-2 Drives Development of COVID-19. *Cell* **2020**, 181, 1036-1045.
9. Simons, K., Ikonen, E. Functional Rafts in Cell Membranes. *Nature* **2020**, 387, 569–572.
10. Murai, T., The Role of Lipid Rafts in Cancer Cell Adhesion and Migration. *Int. J. Cell Biol.* **2012**, 1-6.

11. Cui, HL., Grant, A., Mukhamedova, N., Pushkarsky, T., Jennelle, L. *J. Lipid Res.* **2012**, 53, 696-708.
12. Bakillah, A., Hejji, FA., Almasaud, A., Jami, HA., Hawwari, A. Lipid Raft Integrity and Cellular Cholesterol Homeostasis Are Critical for SARS-CoV-2 Entry into Cells. *Nutrients* **2022**, 14, 3417.
13. Li W, Moore MJ., Vasilieva N, Sui J, Wong SK. Angiotensin-converting Enzyme 2 is a Functional Receptor for the SARS Coronavirus. *Nature* **2003,** 426. 450-454.
14. Musarrat, F., Chouljenko, V., Dahal, A., Nabi, R., Chouljenko, T. The Anti-HIV Drug Nelfinavir Mesylate (Viracept) is a Potent Inhibitor of Cell Fusion Caused by the SARSCoV-2 Spike (S) Glycoprotein Warranting Further Evaluation as an Antiviral Against COVID-19 Infections. *J Med Virol*. **2020**, 92, 2087-2095.
15. Niyogi ,K., Hildreth, JE. Characterization of New Syncytium-inhibiting Monoclonal Antibodies Implicates Lipid Rafts in Human T-cell Leukemia Virus Type 1 Syncytium Formation. *J Virol.* **2001**, 75, 7351-61.
16. Sviridov, D., Miller, YI., Ballout, RA., Remaley, AT., Bukrinsky, M. Targeting Lipid Rafts-A Potential Therapy for COVID-19. *Front Immunol*. **2020**, 11, 574508.
17. Li, GM., Li, YG., Yamate, M., Li, SM., Ikuta, K.. Lipid Rafts Play an Important Role in the Early Stage of Severe Acute Respiratory Syndrome-Coronavirus Life Cycle. *Microbes Infect.* **2007**, 9, 96-102.
18. Barman, S., Nayak, DP. Lipid raft disruption by cholesterol depletion enhances influenza A virus budding from MDCK cells. *J Virol*. **2007**, 81, 12169-78.
19. Sorice, M., Misasi, R., Riitano, G., Manganelli, V., Martellucci, S, et al. Targeting Lipid Rafts as a Strategy Against Coronavirus. *Front Cell Dev Biol.* **2021**, 4, 618296.
20. Taniguchi, M., Okazaki, T., The Role of Sphingomyelin Synthase in Cell Death, Proliferation and Migration from Cell and Animal Models to Human Disorders. *Biochim. Biophys. Acta Mol. Cell Biol. Lipids.* **2014**, 1841, 692-703.
21. Jiang, XC., Chiang, YP., Sphingomyelin Synthase Family and Phospholipase Cs. *Adv Exp Med Biol.* **2022**, 1372, 77-86.

22. Mitsutake, S., Zama, K., Yokota, H., Yoshida, T., Tanaka, M., et al. Dynamic Modification of Sphingomyelin in Lipid Microdomains Controls Development of Obesity, Fatty Liver, and Type 2 Diabetes. *J Biol Chem*. **2011**, 286, 28544-28555.
23. Sugimoto, M., Shimizu, Y., Zhao, S., Ukon, N., Nishijima, KI., et al. Characterization of the Role of Sphingomyelin Synthase 2 in Glucose Metabolism in Whole-body and Peripheral Tissues in Mice, *Biochim. Biophys. Acta, Mol. Cell Bio Lip.* **2016**, 1861, 688-702.
24. Chen, Y., Cao, Y. The Sphingomyelin Synthase Family: Proteins, Diseases, and Inhibitors, *Biological Chemistry*, **2017** 398, 1319-1325.
25. Othman, MA., Yuyama, K., Murai, Y., Igarashi, Y., Mikami, D., et al. Malabaricone C as Natural Sphingomyelin Synthase Inhibitor against Diet-Induced Obesity and Its Lipid Metabolism in Mice. *ACS Med Chem Lett*. **2019** 10, 1154-1158.
26. Baloni, P., Arnold, M., Buitrago, L., Nho, K., Moreno, H. et al. Multi-Omic Analyses Characterize the Ceramide/Sphingomyelin Pathway as a Therapeutic Target in Alzheimer's disease. *Commun Biol.* **2022**, 5, 1074
27. .Zukowska, J., Moss, SJ., Subramanian, V., Acharya, KR., Molecular Basis of Selective Amyloid-β Degrading Enzymes in Alzheimer's Disease, *The FBS Journal*, **2023**, 291, 2999-3029.
28. Yuyama, K., Sun, H., Mitsutake, S., and Igarashi, Y., Sphingolipid-modulated Exosome Secretion Promotes Clearance of Amyloid-β by Microglia, *J. Biol. Chem*., **2012**, 287, 10977-10989.
29. Morrow, A., Panyard, DJ., Deming, YK., Jonaitis, E., Dong, R., et al. Cerebrospinal Fluid Sphingomyelins in Alzheimer's Disease, Neurodegeneration, and Neuroinflammation, *J Alzheimers Dis*. **2022**, 90, 667-680.
30. Zheng, K., Chen, Z., Feng, H., Chen, Y., Zhang, C., et al., Sphingomyelin Synthase 2 Promotes an Aggressive Breast Cancer Phenotype by Disrupting the Homoeostasis of Ceramide and Sphingomyelin. *Cell Death Dis*, **2019** 10, 157.
31. Feng, H., Dong, Y., Chen, K., You, Z., Weng, J. et al. Sphingomyelin Synthase 2 Promotes the Stemness of Breast Cancer Cells via Modulating NF-κB Signaling Pathway. *J Cancer Res Clin Oncol*, **2024**, 150, 46.

32. He, S., Gu, X., Yang, J., Xu, F., Hu, J., et al. Sphingomyelin Synthase 2 is a Positive Regulator of the CSF1R-STAT3 Pathway in Pancreatic Cancer-Associated Macrophage, *Front Pharmacol*. **2022**, 17, 902016.
33. Mori, Y., Sakata, M., Sakai, S., Okamoto, T., Nakatsu, Y., Membrane Sphingomyelin in Host Cells Is Esential for Nucleocapsid Penetration into the Cytoplasm after Hemifusion during Rubella Virus Entry, *mBio*, **2022**, 13, 6.
34. Tani, H., Shiokawa, M., Kaname, Y., Kambara, H., Mori, Y., Abe, T., et al. Involvement of Ceramide in the Propagation of Japanese Encephalitis Virus. *J Virol.* **2010**, 84, 2798-2807.
35. Taniguchi, M., Tasaki, T., Ninomiya, H., ueda, Y., Kuremoto, KI., et al. Sphingomyelin Generated by Sphingomyelin Synthase 1 is Involved in Attachment and Infection with Japanese Encephalitis Virus. *Sci Rep*, **2016**, 6, 37829.
36. Hayashi, Y., Nemoto-Sasaki, Y., Tanikawa, T., Oka, S., Tsuchiya, K., et al. Sphingomyelin Synthase 2, but not Sphingomyelin Synthase 1, is Involved in HIV-1 Envelope-mediated Membrane Fusion. *J Biol Chem*. **2014**, 289, 30842-30856.
37. Avota, E., Bodem, J., Chithelen, J., Mandasari, P., Beyersdorf, N., et al. The Manifold Roles of Sphingolipids in Viral Infections, *Front Physiol*, **2021**, 12, 715527.
38. Newman, DJ., Cragg, GM., Natural Products as Sources of New Drugs over the Nearly Four Decades from 01/1981 to 09/2019, *J Nat Prod*, **2020**, 83, 770-803.
39. Sayed, KAE., Natural Products as Antiviral Agents, *Studies in Nat Prod Chem*, **2007**, 24, 473-572.
40. Kurokawa, M., Shimizu, T., Watanabe, W., Shiraki, K., Development of New Antiviral Agents from Natural Products, *Antimicrob Agents*, **2010**, 2, 49-57.
41. Perera, C., Efferth, T. Antiviral Medicinal Herbs and Phytochemicals. *J. Pharmacogn*. **2012**. 3, 45–48.
42. Martin, KW., Ernst, E., Antiviral Agents from Plants and Herbs: A Systematic Review, *Antivir Ther*, **2003**, 8, 77-90.
43. Hussain, W., Haleem, KS., Khan, I., Tauseef, I, Qayyum, S., et al. Medicinal Plants: A Repository of Antiviral Metabolites, *Future Virol*, **2017**, 12, 299-308.

44. Di Petrillo, A., Orrù, G., Fais, A., Fantini, MC.. Quercetin and Its Derivates as Antiviral Potentials: A Comprehensive Review, *Phytother Res*. **2022**, 36, 266-278.
45. Gasmi, A., Mujawdiya, P. K., Lysiuk, R., Shanaida, M., Peana, M., et al. Quercetin in the Prevention and Treatment of Coronavirus Infections: A Focus on SARS-CoV-2. *Pharmaceuticals*, **2022**, 15, 1049.
46. Huang, CT., Chao, TL., Kao, HC., Pang, YH., Lee, WH., et al. Enhancement of the IFN-β-induced Host Signature Informs Repurposed Drugs for COVID-19, *Heliyon*, **2020**, 6, e05646.
47. Meneguzzo, F., Ciriminna, R., Zabini, F., Pagliaro, M. Review of Evidence Available on Hesperidin-Rich Products as Potential Tools against COVID-19 and Hydrodynamic Cavitation-Based Extraction as a Method of Increasing Their Production. *Processes*, **2020**, 8, 549.
48. Schutz, D., Conzelmann, C., Fois, G., Groß, R., Weil, T., et al. Carrageenan-containing over-the-counter nasal and oral sprays inhibit SARS-CoV-2 infection of airway epithelial cultures. Am. J. Physiology-Lung Cell. Mol. *Physiology*, **2021**, 320, 750–756.

Chapter 2

Discovery of Malabaricone C as SARS-CoV-2 Inhibitor from Spices

2.1 Abstract

SARS-CoV-2 is one of the coronaviruses responsible for the worldwide outbreak of a respiratory illness termed COVID-19, which caused a pandemic infectious disease situation at the end of 2019. Although the SARS-CoV-2 epidemic worldwide has gradually decreased, the situation has not yet been stamped in some areas and has become a global health emergency. It is possible that we could again be threatened by a new coronavirus. Therefore, new nucleotide analog drugs and vaccines or drug repositioning for SARS-CoV-2 are still being developed, yet their safety and efficacy against COVID-19 remain underexplored. Readily available compounds from edible plants, which can provide a safe alternative for drugs with lesser side effects, may become one promising source of anti-viral reagents. In this study, we identified malabaricone C, found in edible plants such as the mace spice of nutmeg, as the first natural inhibitor of SARS-CoV-2. Malabaricone C and its chemical derivatives showed EC_{50} values of 1–1.5 μM against SARS-CoV-2 and its variants in mammalian cells. Thus, the nontoxic malabaricone C is a suitable candidate as a drug that can be employed in the treatment and prevention of COVID-19.

2.2 Introduction

Severe Acute Respiratory Syndrome Coronavirus 2 (SARS-CoV-2) is an enveloped beta coronavirus with positive-sense, single-stranded RNA. Identified as the third most pathogenic coronavirus after SARS-CoV and Middle East respiratory syndrome coronavirus (MERS-CoV) in the 21st century, it emerged in Wuhan, China, in late 2019 and rapidly became a global health emergency[1]. The disease it causes, Coronavirus Disease 2019 (COVID-19), presents with respiratory symptoms such as cough, fever, and severe pneumonia, which can lead to death[2,3]. While the incidence of COVID-19 has declined globally, some areas continue to experience outbreaks of new variants.

During the SARS-CoV-2 pandemic, the molecular mechanisms of infection of SARS-CoV-2 in host cells were gradually elucidated. In the initial step, the surface unit S1 of the virus spike (S) glycoprotein is cleaved and binds to angiotensin-converting enzyme 2 (ACE2). In the second step, to provide unit S2 for fusion to host cell membranes, S1/S2 and S2' sites of S glycoproteins need to be proteolytically

cleaved by the host cell protease transmembrane serine protease 2 (TMPRSS2-pathway) [4]. In addition, other candidates, such as neuropilin 1 as a co-receptor, and cathepsin L, TMPRSS11D, and TMPRSS13, have been proposed to be related to SARS-CoV-2 infection as well[5-8]. However, the details regarding the pathogenesis of SARS-CoV-2 remain unclear. Therefore, the accurate inhibition of SARS-CoV-2 infection remains a challenge.

The development of new mRNA vaccines has provided considerable advantages in combating SARS-CoV-2, although these vaccines are associated with side effects, including headache, skin discoloration, fatigue, and allergic reactions[9]. In addition, antiviral drugs against SARS-CoV-2 are still in developmental stages. However, several approved repositioned materials and investigational drugs have been used for their antiviral activities against SARS-CoV-2. For example, remdesivir (GS5734), a monophosphoramidate prodrug with an adenosine analog for Ebola[10] and Marburg viruses, has been recognized as effective against enveloped viruses like SARS-CoV and MERS-CoV[11] *in vivo*. Xiao et al. reported that remdesivir exhibits potent antiviral activity against SARS-CoV-2 at low micromolar concentrations (EC_{50} = 0.77 μM) in Vero E6 cells[12]. Before long, the use of remdesivir in COVID-19 had received emergency use authorization from the FDA. However, owing to limited alternatives and high-risk side effects, the development of improved therapeutic agents is urgently required.

Apart from FDA-approved drugs, natural products have gained considerable attention for their medicinal properties. Bioactive compounds found in food and edible sources are promising candidates for new SARS-CoV-2 therapies. Research is underway to investigate various naturally occurring compounds for their potential in inhibiting SARS-CoV-2 infection. For example, Rao et al. reported that the phytochemical shikonin could be a promising drug target against the main protease of SARS-CoV-2, which regulates viral replication and transcription[13]. In another study, flavonoids, including myricitrin and licoleafol, were introduced as inhibitors of the chymotrypsin-like protease of SARS-CoV-2 based on the predicted 3D structure[14].

Panduratin A extracted from *Boesenbergia rotunda*, a promising anti-SARS-CoV-2 agent, was also reported by using a high-content imaging system coupled with a plaque reduction assay, has also been reported by Borwornpinyo and

Thitithanyanont[15]. In addition, there have been reports on the search for inhibitors from natural products to create more effective inhibitors for new coronavirus variants that must emerge in the future[16-19]. However, although these results are encouraging, there is insufficient safety data to confirm the benefits and potential of these materials. In addition, naturally occurring compounds in foods are recognized as SARS-CoV-2 drug targets[16].

Recently, gingkolic acid, a natural compound isolated from *Ginkgo biloba*, has been shown to inhibit the cell fusion of enveloped viruses and viral DNA and protein synthesis[17]. We have also demonstrated that ginkgolic acid has highly potent inhibitory activity towards sphingomyelin synthase (SMS), modulating sphingomyelin levels in lipid membrane fluidity and signal transduction[20], by our group[21]. In addition, SMS is related to the generation and release of influenza virus particles in the human haploid cell line[22] and is involved in HIV-1 Env-mediated membrane fusion[23]. Therefore, modulation of SMS activity could be a novel therapeutic approach for enveloped viral infections.

To date, we have reported naturally occurring SMS modulatory compounds, daurichromenic acid from the Chinese traditional medicinal plant *Rhododendron dauricum*[24], and malabaricone C from the fruits of *Myristica cinnamomea*[25]. The latter inhibitors may be especially safe, with fewer side effects than other SMS inhibitors because they were isolated from an edible fruit. In the present study, we demonstrated the ability of malabaricone C and its organic synthesis derivatives to inhibit SARS-CoV-2 infection and fusion with Vero E6/TMPRSS2 cells, as determined by MTT and fusion assays. Our new findings demonstrate the potential ability of malabaricones to inhibit SARS-CoV-2 infection, which could attract much interest in the development of prospective drugs for SARS-CoV-2.

2.3 Results and Discussion

SAR Study of Malabaricone C and Its Derivatives as Potential Anti SARS-CoV-2

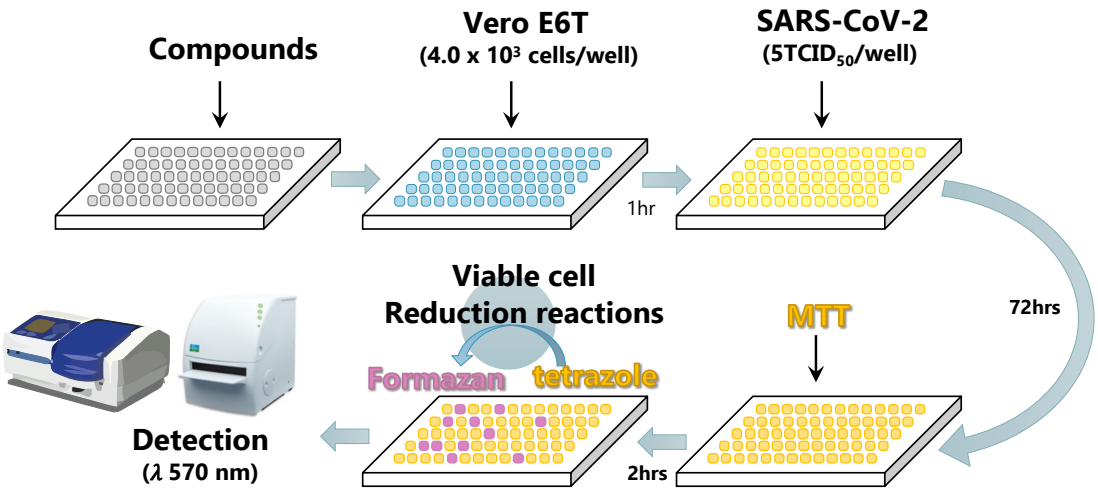

Figure 1. Flowchart for SARS-CoV-2 entry inhibition MTT assay

In order to find a novel antivirus for SARS-CoV-2, several natural products that are already reported to have inhibition activities were subjected to an MTT asay. To measure the inhibitory activities of ginkgolic acid, malabaricone C, and daurichromenic acid towards SARS-CoV-2 (WK-521), an MTT assay was conducted by using VeroE6 cells that stably express TMPRSS2 (VeroE6/TMPRSS2) are highly susceptible to SARS-CoV-2 infection[26] (Figure 1). Ginkgolic acid showed moderate inhibition of SARS-CoV-2 infection in VeroE6/TMPRSS2 cells, with an EC_{50} of 7.9 μM. Malabaricone C showed potential inhibitory activity against SARS-CoV-2 (WK-521) entry into VeroE6/TMPRSS2 cells (EC_{50} = 1.5 μM, Figure 2).

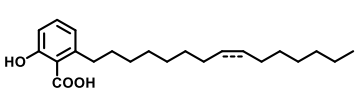

Ginkgolic acid

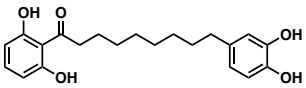

Malabaricone C

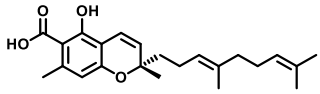

Daurichromenic acid

Compound	EC_{50} (nM)	CC_{50} (nM)	Selectivity Index
ginkgolic acid	7852	39951	5.1
malabaricone C	1498	14592	9.7
daurichromenic acid	$>CC_{50}$	36923	N.D.
remdesivir	503	>10000	>19.9

Figure 2. Preliminary MTT assay for inhibitory activities towards SARS-CoV-2 with phytochemical compounds: ginkgolic acid and daurichromenic acid.

Next, to investigate the possibility of a highly potent inhibitory activity against SARS-CoV-2, structure-activity relationship (SAR) studies of the malabaricone C scaffold were performed. The reduction of the carbonyl group (2) and various modifications, such as esterification (acetyl (3, 4) and benzoyl (5, 6)) and etherification (methyl and benzyl) of the hydroxy groups on the aromatics, was achieved (Figure 3). The details of the derivatization scheme are presented in the experimental section, Scheme 1. Furthermore, the SAR of the chain length between the two aromatic rings could be another point of interest for the altered activity. Malabaricone C with shorter and longer alkyl chains of malabaricone C was synthesized as reported by Tsuda et al.[27] with slight modifications (Experimental Section Scheme 2).

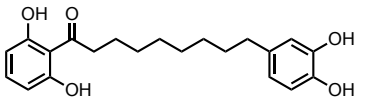

malabaricone C (**1**)

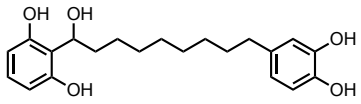

2

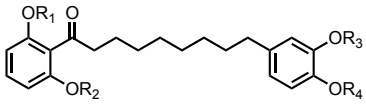

Compound	R_1	R_2	R_3	R_4
3	Ac	Ac	Ac	Ac
4	Ac	Ac	Ac (H)	H (Ac)
5	Bz	Bz	Bz	Bz
6	Bz	Bz	Bz (H)	H (Bz)
7	Me	Me	Me	Me
8	Me	Me	Me (H)	H (Me)
9	H	Bn	Bn	Bn
10	Bn	Bn	Bn (H)	H (Bn)

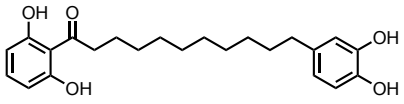

11

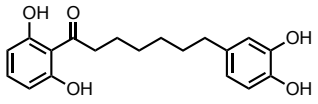

12

Figure 3. Derivatization of malabaricone C for SAR study

The antiviral activity of the derivatized malabaricone C compounds was evaluated using the same MTT assay. The reduced carbonyl group compound 2 exhibited slightly decreased activity compared with malabaricone C. Esterification and etherification of the hydroxy group compounds (3, 4, 6, and 8) retained SARS-CoV-2 inhibitory activity. Interestingly, the modification of both hydroxyl groups on the catechol ring (5 and 7) reduced their inhibitory activities, suggesting that the hydroxyl groups of the catechol ring have a significant effect on its activity. In contrast, the tetrabenzylated compound (9) showed a dramatic loss of activity. Partial benzyl modification (10) also reduced the antiviral activity (Table 1, Figure 4). However, this mechanism remains unclear, suggesting the need for further detailed investigation.

Additionally, the chain length between the two aromatic rings significantly affected the activity; the two-carbon longer chain 11 dramatically showed less potent antiviral activity than the two-carbon shorter chain 12. Therefore, the carbonyl group and the appropriate chain length between the two aromatic rings are essential for the inhibition of SARS-CoV-2 entry. Moreover, the esterification and etherification of malabaricone C had little effect on its inhibitory activity.

Compound	SARS-CoV-2 (WK-521)		
	EC_{50} (μM)	CC_{50} (μM)	Selectivity Index
1	1.5	14	9.7
2	5.4	>40	>7.4
3	1.3	16	12
4	1.5	15	10
5	14	>40	>2.8
6	1.0	6.8	6.8
7	6.0	27	4.6
8	1.5	5.5	3.7
9	n.d.	n.d.	-
10	21	>40	>1.8
11	14	32	2.3
12	2.9	41	14.2
remdesivir	0.5	>10	>19.9
molnupiravir	0.15	5.3	33.8

Table 1: The Structure-activity relationship of malabaricone C derivatives in the inhibition of SARS-CoV-2 (WK-521) infection. The concentration numbers indicate the EC_{50}, CC_{50}, and selectivity index values, respectively. These values were calculated using an MTT assay system. (n.d. = not determined)

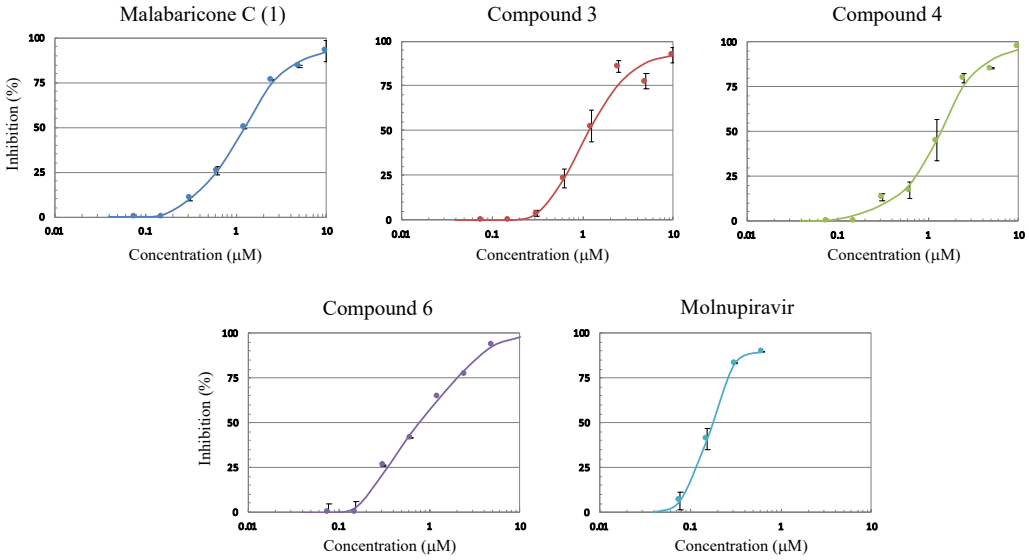

Figure 4. Curve of CC_{50} value of malabaricone C and its potent anti-SARS-CoV-2 derivatives. Results are presented as means, and experiments were repeated at least 3 times.

Anti-SARS-CoV-2 Variants Effect of Malabaricone C in Human Embryonic Kidney Cells 293

To explore the inhibition of SARS-CoV-2 entry by malabaricone C and its derivatives during human infection, we examined their antiviral activity against the UK SARS-CoV-2 α (B.1.1.7), Brazilian SARS-CoV-2 γ (P.1), and Indian SARS-CoV-2 δ variants (B.1.617.2) using human embryonic kidney cells 293 (HEK293TA) through the MTT assay. As with WK-521, malabaricone C and some of its derivatives also exhibited potent anti-SARS-CoV-2 activity with an EC_{50} of 1.5 – 2.0 μM (Table 2).

Compound	UK SARS-CoV-2 α variant			Brazilian SARS-CoV-2 γ variant			Indian SARS-CoV-2 δ variant		
	EC_{50} (μM)	CC_{50} (μM)	Selectivity Index	EC_{50} (μM)	CC_{50} (μM)	Selectivity Index	EC_{50} (μM)	CC_{50} (μM)	Selectivity Index
1	1.9	5.2	2.6	1.7	6.2	3.6	1.9	6.5	3.4
2	7.3	12	1.7	6.8	16	2.4	8.3	23	2.7
3	1.4	6.2	4.3	1.5	6.4	4.3	1.4	6.4	4.5
4	1.4	6.1	4.1	1.3	6.6	4.8	1.6	6.7	4.1
6	1.5	3.2	2.1	1.6	2.9	1.7	0.71	2.9	4
11	5.2	24	4.7	16	22	1.4	7.3	19	2.6
12	2.9	6.5	2.2	7.2	10	1.5	4.3	10	2.3
remdesivir	<0.078	0.5	>6.7	<0.078	0.7	>9.3	<0.078	0.7	>9.3
molnupiravir	0.4	6.1	14.7	0.5	6.7	13	0.45	5.9	13

Table 2: Malabaricone C and its derivatives in the inhibition of infection by SARS-CoV-2 variants. The concentration numbers indicate the EC_{50}, CC_{50} and selectivity index values, respectively. These values were calculated using an MTT assay system. Results are presented as means, and experiments were repeated at least 2–3 times.

Novel Visualization of Fusion Assay for SARS-CoV-2

Furthermore, we established a novel cell-to-cell fusion assay to establish a visual evaluation system for the inhibitory effect of inhibitors against SARS-CoV-2 entry into uninfected cells. For this purpose, a persistent SARS-CoV-2 infected cell line and a HEK293TA cell line expressing green fluorescent protein (GFP) or mCherry protein were prepared. Figure 5A illustrates the underlying concept wherein yellow hypertrophy cells appear when cell-to-cell fusion occurs, whereas green and red-

colored HEK293 cells are observed when inhibition by antiviral agents occurs. Thus, the inhibitory effect can be evaluated using the number and total area of cells emitting yellow fluorescence as indices, compared to the virus control in the presence of SARS-CoV-2 without inhibitors (VC).

Next, to investigate the inhibitory effect of malabaricones on the fusion assay, cells were treated with malabaricone C and its derivatives (3 and 6) at concentrations ranging from 0.8 to 25 μM. The inhibition of cell fusion increased in a dose-dependent manner, as determined by calculating the intensity of yellow hypertrophic cells (Figure 5B, C). The EC_{50} values of all inhibitors were similar to those in the MTT assay. In addition, these compounds prevented the Indian SARS-CoV-2δ variant as well. Therefore, this cell-cell fusion assay is a simple and versatile tool for studying SARS-CoV-2 mediated fusion.

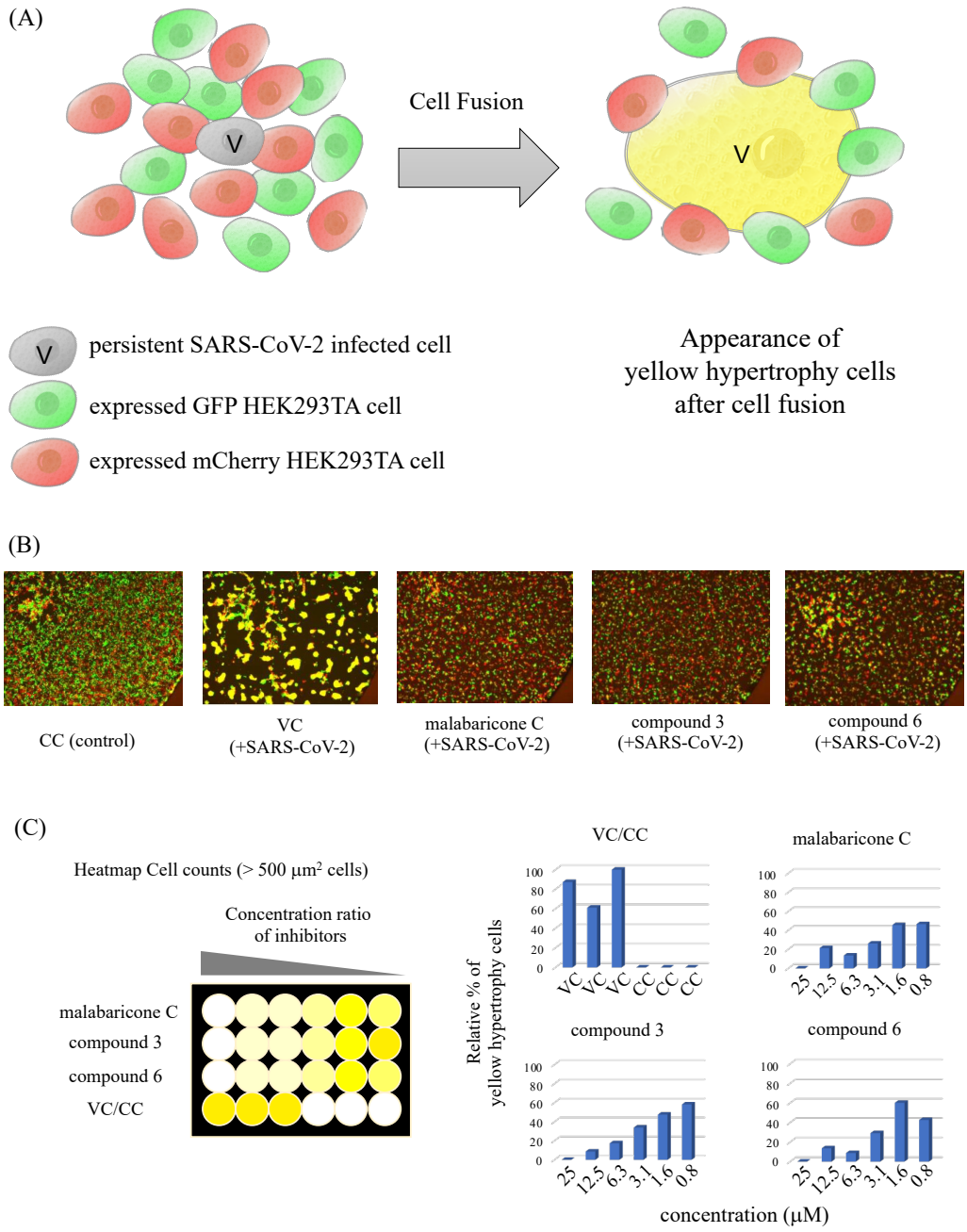

Figure 5. Illustration of the fusion assay for SARS-CoV-2. (A) Concept of the visualized fusion assay for SARS-CoV-2. The persistent cells were turned yellow and hypertrophied by cell fusion with two types of cells that introduced GFP and mCherry. (B) Scanning micrographs (x 40) of the fusion assay in the presence of each inhibitor at 12.5 μM after 24 h. (C) The fusion inhibition of Malabaricone C and its derivatives was measured by counting the number of yellow hypertrophy cells (> 500 μm^2) (n = 2 biological replicates).

2.4 Conclusion

We have identified malabaricone C and its derivatives as natural inhibitors of anti-SARS-CoV-2 (WK-521) agents, similar to remdesivir, in VeroE6/TMPRSS2 cells. In particular, malabaricone C and compounds (3), (4), and (6) had a large selective index of over five values between EC_{50} and CC_{50}. Interestingly, those compounds exhibited potent antiviral effect against SARS-CoV-2 variants with an EC_{50} of 1.5–2.0 μM, and their antiviral activities were equal to or even more potent than those of chloroquine and hydroxychloroquine, the anti-SARS-CoV-2 drugs that have been FDA-approved for COVID-19 treatment[28-30]. The anti-SARS-CoV-2 variants activity of malabaricone C and its derivatives were investigated in human embryonic kidney cells HEK293TA cell lines. These results emphasize the potential implications of malabaricone C and its derivatives as novel anti-SARS-CoV-2 candidates for the treatment of COVID-19. In addition, we established a novel visualized cell fusion assay for SARS-CoV-2 with SARS-CoV-2 persistently infected HEK293TA-G cells (green fluorescence) and HEK293TA-M cells (red fluorescence). This simple cell-cell fusion assay provides a versatile tool for study SARS-CoV-2 mediated fusion. Finally, because malabaricone C is present in various edible plants to prevent COVID-19, it can be safely and easily administered to the elderly and small children. This finding could be a valuable approach for new drug development based on the malabaricone C structure, which has developed rapidly in recent years.

2.5 Experimental Section

Malabaricone C (1) isolation from mace (net-like skin that covers the seed of *Myristica fragrans*)

Mace (50 g) was roughly ground and macerated in methanol (200 ml x 3) for 24. After concentration of the combined methanol extract, 90% of methanol was added and then extracted several times with hexane. The methanol phase was then evaporated and the residue was distributed between ethyl acetate and water. The organic layer was dried, evaporated, and passed through silica gel column with gradient solvent $CHCl_3$: MeOH (100:1 to 50:1) to give compound **1** (187 mg, 0.374%, Rf = 0.2 ($CHCl_3$: MeOH 9:1)). ^{1}H NMR (500 MHz, CD_3OD) d 7.19 (t, *J* = 8.18 Hz, 1H), 6.65 (d, *J* = 8.06 Hz, 1H), 6.60 (d, *J* = 1.71 Hz, 1H), 6.47 (dd, *J* = 1.71, 8.06 Hz, 1H), 6.34 (d, *J* = 8.31 Hz, 2H),

3.11 (t, *J* = 7.45 Hz, 2H), 2.44 (t, *J* = 7.57 Hz, 2H), 1.67 (t, *J* = 7.09 Hz, 2H), 1.49 - 1.60 (m, 2H), 1.24 - 1.43 (m, 8H). ESI-MS(m/z): 381.22700 $[M+Na]^+$.

Synthesis of Malabaricone C Derivatives

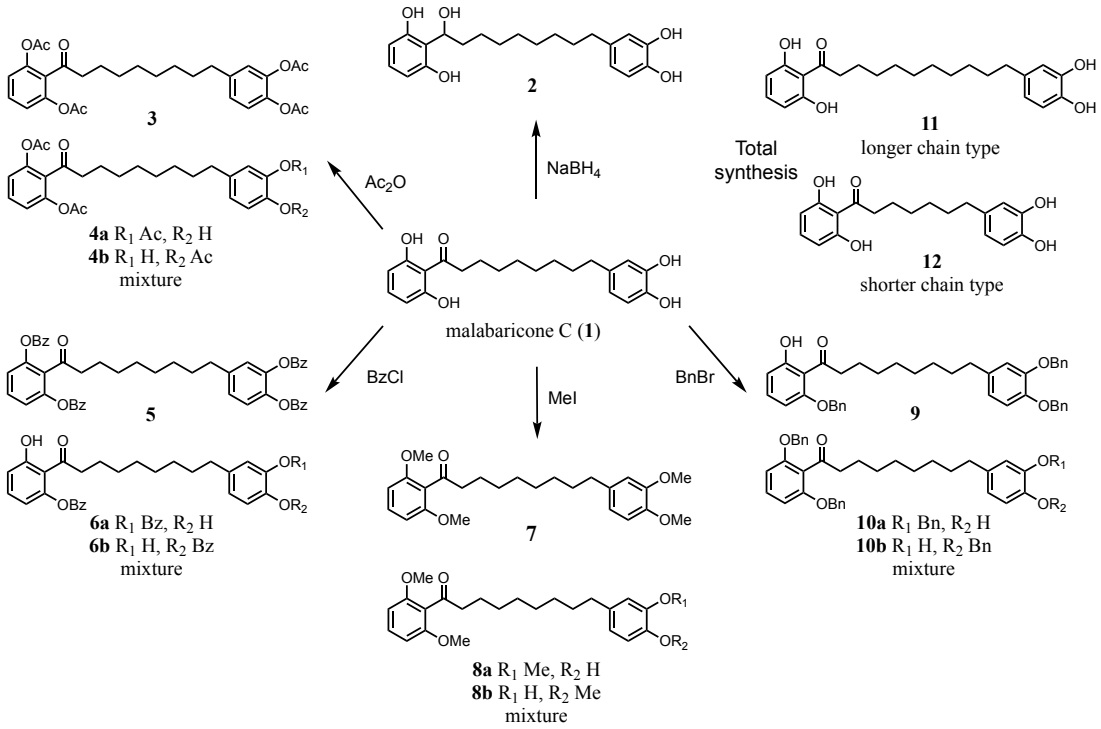

Scheme 1. Synthesis of malabaricone C derivates for SAR study

4-(9-(2,6-dihydroxyphenyl)-9-hydroxynonyl)benzene-1,2-diol ***2***

To a solution of malabaricone C (34 mg, 0.095 mmol) in MeOH (1 mL) was added sodium borohydride (7 mg, 0.19 mmol) at 0 °C. The reaction mixture was stirred for 4 h at 0 °C. The reaction was monitored by TLC ($CHCl_3$/MeOH = 10:1). Distilled water (3 mL) was added to the reaction, and the reaction mixture was extracted with EtOAc. The combined organic layer was washed with brine and dried with $MgSO_4$. The solvent was removed under reduced pressure to give compound **2** (26 mg, 76%). ^{1}H NMR (500 MHz,CD_3OD) δ6.85 (t, J = 8.06 Hz, 1H), 6.64 (d, J = 8.06 Hz, 1H), 6.59 (s, 1H), 6.47 (d, J = 8.06 Hz, 1H), 6.22 - 6.30 (m, 2H), 5.17 - 5.24 (m, 1H), 2.43 (t, J = 7.57 Hz, 2H), 1.75 - 1.86 (m, 21H), 1.63 - 1.75 (m, 1H), 1.49 - 1.58 (m, 2H), 1.30 (br. s., 10H). ^{13}C NMR (126 MHz, CD_3OD) δ160.5, 158.8, 157.1, 155.7, 155.5,

144.5, 139.8, 134.4, 127.5, 119.2, 115.5, 115.1, 114.8, 106.7, 68.9, 36.4, 34.8, 31.5, 29.3, 29.2, 29.1, 28.9, 25.2. ESI-MS(m/z): 383.187 $[M+Na]^+$.

*4-(9-(2,6-diacetoxyphenyl)-9-oxononyl)-1,2-phenylene diacetate **3***

To a solution of malabaricone C (35 mg, 0.098 mmol) in pyridine (1 mL) was added Ac_2O (1.5 mL) at 70 °C and stirred overnight at 70 °C. The reaction mixture was extracted with EtOAc and washed with brine. The organic phase was dried by $MgSO_4$ and evaporated with reduced pressure. The crude product was purified by silica gel column chromatography (*n*-hexane/EtOAc = 4:1) to obtain compound **3** (45 mg, 87%). ^1H NMR (500 MHz, $CDCl_3$) δ 7.41 (t, J = 8.31 Hz, 1H), 7.02 - 7.09 (m, 4H), 6.98 (d, J = 1.71 Hz, 1H), 2.72 (t, J = 7.33 Hz, 2H), 2.58 (t, J = 7.50 Hz, 2H), 2.27 (d, J = 1.71 Hz, 6H), 2.25 (s, 6H), 1.62 - 1.67 (m, 2H), 1.57 - 1.61 (m, 2H), 1.31 (s, 8H). ^{13}C NMR (126 MHz, $CDCl_3$) δ201.3, 168.6, 168.5, 168.4, 162.8, 161.1, 147.6, 141.7, 139.8, 130.3, 128.0, 126.4, 123.1, 122.9, 120.4, 44.0, 35.3, 31.0, 29.3, 29.2, 23.6, 20.9, 20.6. ESI-MS(m/z): 549.317 $[M+Na]^+$.

*2-(9-(4-acetoxy-3-hydroxyphenyl)nonanoyl)-1,3-phenylene diacetate **4a** and 2-(9-(3-acetoxy-4-hydroxyphenyl)nonanoyl)-1,3-phenylene diacetate **4b***

To a stirred solution of malabaricone C (52 mg, 0.15 mmol) in CH_3CN (2 mL) was added K_2CO_3 (60 mg, 0.43 mmol) at room temperature. The reaction mixture was stirred for 15 min. The temperature was reduced to 0 °C, and Ac_2O (41 µL, 0.44 mmol) was added. The mixture was stirred for 1 h. The mixture was extracted with EtOAc and washed with brine. The organic phase was dried by $MgSO_4$ and evaporated with reduced pressure. The crude product was purified by silica gel column chromatography (*n*-hexane/EtOAc = 4:1) to obtain a mixture of Compound **4** (18 mg, 26%).

^1H NMR (500 MHz, $CDCl_3$) δ 7.42 (t, J = 8.18 Hz, 1H), 7.06 (d, J = 8.31 Hz, 2H), 6.98 (d, J = 8.31 Hz, 1H), 6.88 - 6.94 (m, 1H), 6.82 (d, J = 1.95 Hz, 1H), 6.72 (dd, J = 2.08, 8.18 Hz, 1H), 2.69 - 2.75 (m, 2H), 2.50 - 2.56 (m, 2H), 2.33 - 2.35 (m, 3H), 2.25 - 2.27 (m, 6H), 1.62 – 1.67 (m, 2H), 1.55 – 1.60 (m, 2H), 1.31 (m, 8H). ^{13}C NMR (126 MHz, $CDCl_3$) δ 201.5, 177.7, 168.7, 168.6, 162.8, 161.1, 159.4, 147.6, 146.5, 144.6, 142.0, 136.5, 135.9, 130.4, 127.9, 126.8, 122.0, 121.9, 120.9, 120.4, 117.6, 117.5,

44.0, 35.3, 34.9, 31.3, 31.0, 29.3, 29.2, 29.1, 29.0, 23.6, 21.0, 20.9. ESI-MS(m/z): 507.231 $[M+Na]^+$.

4-(9-(2,6-bis(benzoyloxy)phenyl)-9-oxononyl)-1,2-phenylene dibenzoate ***5***

To a solution of malabaricone C (50 mg, 0.14 mmol) in pyridine (1 mL) was added BzCl (65 μL, 0.56 mmol) at room temperature. The reaction mixture was stirred overnight at room temperature. The reaction mixture was extracted with EtOAc and washed with brine. The organic phase was dried by $MgSO_4$ and evaporated with reduced pressure. The crude product was purified by silica gel column chromatography (*n*-hexane/EtOAc = 4:1) to obtain compound **5** (66 mg, 61%).

^1H NMR (500 MHz, $CDCl_3$) δ 8.14 (dd, J = 1.10, 8.18 Hz, 4H), 8.03 - 8.08 (m, 4H), 7.61 - 7.67 (m, 2H), 7.48 - 7.55 (m, 7H), 7.37 (dt, J = 2.44, 7.82 Hz, 4H), 7.28 (d, J = 8.06 Hz, 1H), 7.24 (d, J = 8.31 Hz, 2H), 7.17 (d, J = 1.95 Hz, 1H), 7.12 (dd, J = 1.83, 8.18 Hz, 1H), 2.76 (t, J = 7.33 Hz, 2H), 2.59 (t, J = 7.57 Hz, 2H), 1.50 - 1.58 (m, 4H), 1.16 - 1.23 (m, 2H), 1.06 - 1.14 (m, 6H). ^{13}C NMR (126 MHz, $CDCl_3$) δ 201.3, 164.5, 164.3, 162.8, 161.1, 147.9, 142.2, 141.8, 140.3, 134.0, 133.6, 133.5, 130.4, 130.3, 130.1, 128.9, 128.7, 128.4, 126.5, 123.2, 123.1, 120.6, 44.1, 35.4, 31.1, 29.2, 29.1, 29.0, 23.5. ESI-MS (m/z): 797.378 $[M+Na]^+$.

2-(9-(4-(benzoyloxy)-3-hydroxyphenyl)nonanoyl)-3-hydroxyphenyl benzoate ***6a*** *and 2-(9-(3-(benzoyloxy)-4-hydroxyphenyl)nonanoyl)-3-hydroxyphenyl benzoate* ***6b***

To a solution of malabaricone C (50 mg, 0.14 mmol) in pyridine (2 mL) was added BzCl (33 μL, 0.28 mmol) at 0 °C. The reaction was stirred for 30 min at 0 °C and monitored by TLC (*n*-hexane/EtOAc = 3:2). The reaction mixture was extracted with EtOAc and washed with brine. The organic phase was dried by $MgSO_4$ and evaporated with reduced pressure. The crude product was purified by silica gel column chromatography (*n*-hexane/EtOAc = 4:1) to obtain a mixture of compound **6** (22 mg, 28%).

^1H NMR (500 MHz, $CDCl_3$) δ 12.73 (br. s., 1H), 8.18 - 8.25 (m, 4H), 7.63 - 7.70 (m, 2H), 7.49 - 7.57 (m, 4H), 7.41 - 7.48 (m, 1H), 7.09 (d, J = 8.31 Hz, 1H), 6.92 - 7.01 (m, 2H), 6.87 (d, J = 1.71 Hz, 1H), 6.76 (dd, J = 1.83, 8.18 Hz, 1H), 6.67 (dd, J = 2.81, 7.94 Hz, 1H), 2.89 (dt, J = 4.89, 7.45 Hz, 2H), 2.49 - 2.56 (m, 2H), 1.56 - 1.64 (m,

2H), 1.48 - 1.56 (m, 2H), 1.03 - 1.23 (m, 8H). ^{13}C NMR (126 MHz, $CDCl_3$) δ 206.0, 165.1, 163.8, 162.8, 161.1, 151.3, 146.8, 145.0, 142.2, 135.1, 134.3, 134.0, 130.4, 130.3, 128.9, 128.7, 127.0, 122.1, 122.0, 121.1, 117.9,116.5, 114.7, 114.2, 44.0, 35.3, 34.9, 31.3, 31.1, 29.2, 29.0, 28.9, 23.9. ESI-MS (m/z): 589.264 $[M+Na]^+$.

1-(2,6-dimethoxyphenyl)-9-(3,4-dimethoxyphenyl)nonan-1-one ***7,*** *1-(2,6-dimethoxyphenyl)-9-(3-hydroxy-4-methoxyphenyl)nonan-1-one* ***8a*** *and 1-(2,6-dimethoxyphenyl)-9-(4-hydroxy-3-methoxyphenyl)nonan-1-one* ***8b***

To a stirred solution of malabaricone C (50 mg, 0.14 mmol) in 5 mL of DMF was added K_2CO_3 (97 mg, 0.70 mmol) and MeI (34.86 μL, 0.56 mmol). The reaction was stirred at room temperature for 24 h, and the resulting mixture was extracted with EtOAc. The organic layer was dried with $MgSO_4$ and evaporated. The purification using silica gel column chromatography (EtOAc/$CHCl_3$/*n*-hexane = 1:1:2) obtained compound **7** (17.8 mg) and a mixture of compound **8** (10 mg)

Compound **7**: ^{1}H NMR (500 MHz, $CDCl_3$) δ 7.22 - 7.26 (1H, m), 6.77 – 6.79 (1H, m), 6.70 – 6.71 (2H, m), 6.54 (d, J = 8.6 Hz, 2H), 3.87 (s, 3H), 3.85 (s, 3H), 3.77 (s, 6H), 2.73 (t, J = 7.5 Hz, 2H), 2.54 (t, J = 10 Hz, 2H), 1.66 (t, J = 7.2, 2H), 1.59 (m, 2H), 1.32 (br. s. 8H). ^{13}C NMR (125 MHz, $CDCl_3$) δ 205.5, 162.8, 161.1, 156.6, 148.7, 147.0, 135.6, 130.3, 120.7, 120.1, 111.7, 111.1, 104.0, 55.9, 55.8, 55.8, 55.8, 44.8, 35.6, 31.7, 29.4, 29.4, 29.3, 29.1, 23.5. ESI MS(m/z): 437.245 $[M+Na]^+$.

Compound **8**: ^{1}H NMR (500 MHz, $CDCl_3$) δ 7.23 - 7.26 (m, 1H), 6.75 - 6.82 (m, 1H), 6.65 - 6.68 (m, 2H), 6.54 (d, J = 8.6 Hz, 2H), 3.87 (d, J = 9 Hz, 3H), 3.77 (s, 6H), 2.73 (t, J = 7.5 Hz, 2H), 2.51 (dt, J = 12.2, 7.8 Hz, 2H), 1.66 (td, J = 7.1, 3.2 Hz, 2H), 1.56 - 1.58 (m, 2H), 1.31 (d, J = 6.6 Hz, 8H). ^{13}C NMR (125 MHz, $CDCl_3$) δ 205.5, 162.8, 161.1, 156.7, 146.3, 134.9, 130.3, 120.8, 119.6, 114.6, 114.0, 110.9, 104.0, 55.8, 55.8, 55.8, 44.8, 35.6, 31.8, 29.4, 29.4, 29.2, 29.1, 23.5. ESI MS(m/z): 423.245 $[M+Na]^+$.

1-(2-(benzyloxy)-6-hydroxyphenyl)-9-(3,4-bis(benzyloxy)phenyl)nonan-1-one 9, 9-(4-(benzyloxy)-3-hydroxyphenyl)-1-(2,6-bis(benzyloxy)phenyl)nonan-1-one ***10a*** *and 9-(3-(benzyloxy)-4-hydroxyphenyl)-1-(2,6-bis(benzyloxy)phenyl)nonan-1-one* ***10b***

Sodium hydride 60% in oil (11.2 mg, 0.28 mmol) was added to a stirred solution of malabaricone C (50 mg, 0.14 mmol) in 5 mL DMF at 0 °C. After stirring for 1 h,

benzyl bromide (66 μL, 0.28 mmol) was added dropwise, and the solution was stirred at room temperature for 24 h. The reaction was quenched with MeOH, evaporated, and extracted with EtOAc. The organic layer was dried with magnesium sulfate and evaporated. The purification using silica gel column chromatography (*n*-hexane/EtOAc = 4:1) gave compound **9** (8.9 mg) and a mixture of **10** (4.5 mg).

Compound **9**: ^{1}H NMR (500 MHz, $CDCl_3$) δ 13.28 (s, 1H), 7.25 - 7.45 (m, 16H), 6.85 (d, J = 8.1 Hz, 1H), 6.78 (m, 1H), 6.67 - 6.69 (m, 1H), 6.59 (d, J = 8.6 Hz, 1H), 6.46 (d, J = 8.3 Hz, 1H), 5.14 (s, 2H), 5.12 (s, 2H), 5.09 (s, 2H), 2.96 (t, J = 7.5 Hz, 2H), 2.48 (t, J = 7.7 Hz, 2H), 1.50 - 1.57 (m, 4H), 1.09 - 1.21 (m, 8H). ^{13}C NMR (125 MHz, $CDCl_3$) δ 208.0, 164.7, 160.4, 148.8, 147.1, 137.6, 137.5, 138.5, 135.7, 135.7, 128.7, 128.7, 128.5, 128.4, 128.4, 128.4, 128.2, 128.2, 127.7, 127.7, 127.4, 127.4, 127.3, 127.3, 127.3, 121.2, 115.7, 115.3, 111.1, 105.0, 102.2, 71.6, 71.4, 71.2, 45.3, 35.4, 31.5, 29.3, 29.3, 29.2, 29.1, 24.5. ESI MS(m/z): 651.406 $[M+Na]^+$.

Compound **10**: ^{1}H NMR (500 MHz, $CDCl_3$) δ 7.17 - 7.42 (m, 16H), 6.82 - 6.85 (m, 1H), 6.75 - 6.78 (m, 1H), 6.67 - 6.69 (m, 1H), 6.59 (d, J = 8.3 Hz, 1H) 5.08 (s, 2H), 5.07 (s, 4H), 2.76 (t, J = 7.5 Hz, 2H), 2.48 (t, 7.5 Hz, 2H), 1.61 - 1.64 (m, 2H), 1.51 - 1.54 (m, 2H), 1.21 - 1.25 (m, 8H). ^{13}C NMR (125 MHz, $CDCl_3$) δ 206.4, 161.1, 159.4, 157.7, 155.8, 136.6, 136.6, 136.5, 130.3, 130.3, 128.7, 128.7, 128.5, 128.5, 128.5, 128.3, 127.8, 127.8, 127.8, 127.8, 127.0, 127.0, 127.0, 127.0, 127.0, 121.3, 119.6, 114.8, 114.3, 112.4, 105.8, 71.3, 71.1, 70.4, 44.8, 35.6, 29.4, 29.3, 29.2, 27.9, 27.8, 23.5. ESI MS(m/z): 651.406 $[M+Na]^+$.

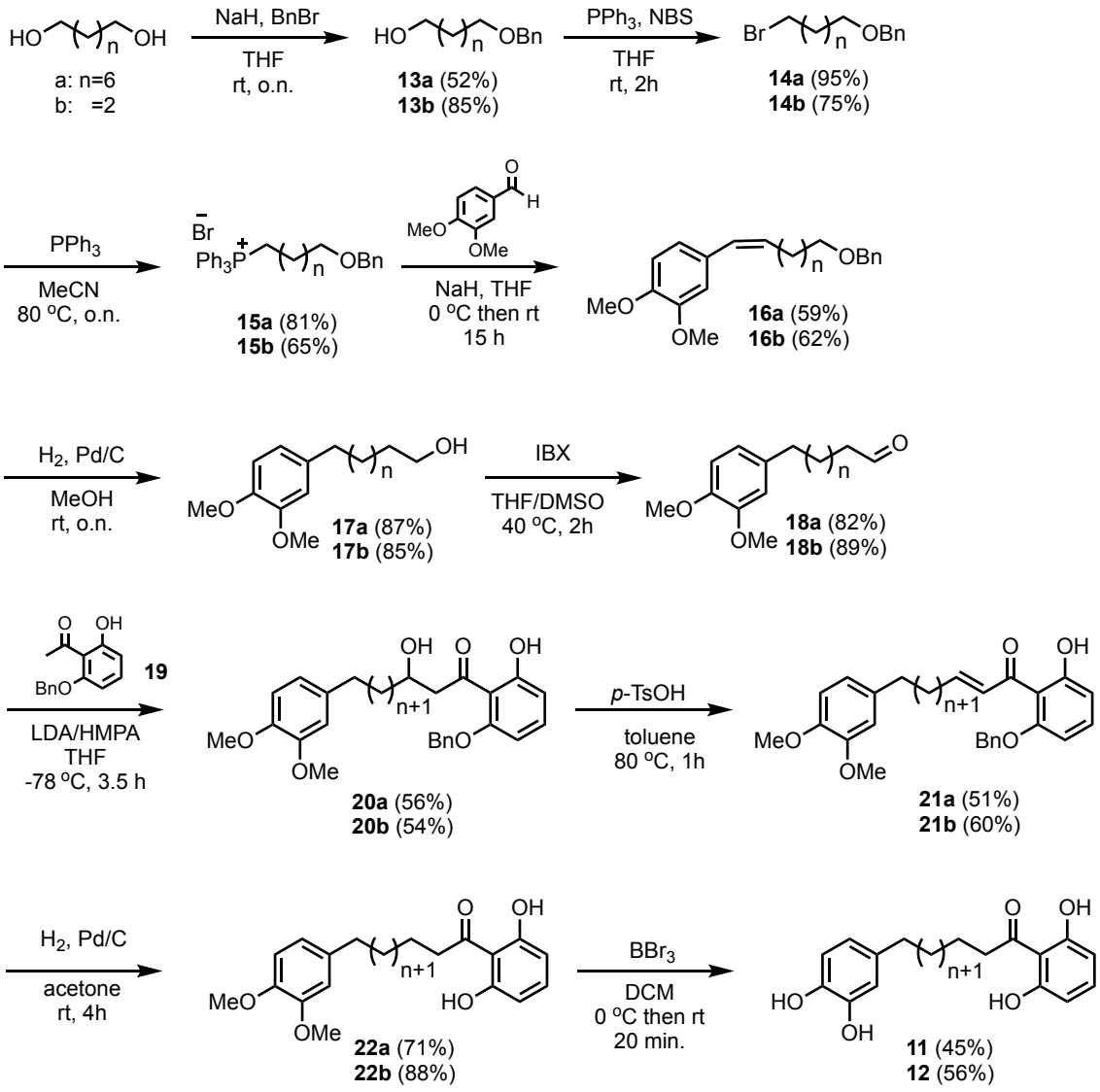

Scheme 2: Synthetic route for the longer and shorter alkyl-chain type malabaricone C

8-(benzyloxy)octan-1-ol ***13a***

Octane-1,8-diol (12.2 g, 84 mmol) was diluted in DMF (100 mL) and cooled to 0 °C and NaH (3.36 g, 84 mmol; 60% dispersion in mineral oil) was added to the mixture. The mixture was then brought to room temperature and stirred for 30 min. Benzyl bromide (10 mL, 84 mmol) was added dropwise to the re-cooled mixture, and the resulting mixture was then continuously stirred at room temperature for 24 h. After completion, the mixture was then quenched with citric acid, evaporated, and extracted with diethyl ether. The organic layer was washed with $NaHCO_3$, dried over $MgSO_4$, and evaporated. The crude products were purified with silica gel column

chromatography (*n*-hexane/EtOAc = 4:1) to give compound **13a** (10.3 g, 52%) as a yellow oil.

^{1}H NMR (500 MHz, $CDCl_3$) δ 7.23 - 7.38 (m, 5H), 4.50 (s, 2H), 3.63 (t, J = 6.6 Hz, 2H), 3.47 (t, J = 6.6 Hz, 2H), 1.52 - 1.68 (m, 4H), 1.33 - 1.46 (m, 8H). ^{13}C NMR (126 MHz, $CDCl_3$) *δ* 138.7, 128.3, 127.6, 127.5, 72.8, 70.5, 62.9, 32.7, 29.7, 29.4, 29.3, 26.1, 25.7. ESI MS(m/z): undetected, Calcd for $C_{15}H_{24}O_2$: 236.1776

Compound **13b**: yellow oil, 84% yield.

^{1}H NMR (500 MHz, $CDCl_3$) δ 7.23 - 7.37 (m, 5H), 4.50 (s, 2H), 3.59 (t, J = 6.11 Hz, 2H), 3.49 (t, J = 6.11 Hz, 2H), 1.58 - 1.74 (m, 4H). ^{13}C NMR (126 MHz, $CDCl_3$) *δ* 138.2, 128.4, 127.8, 127.7, 127.7, 127.7, 73.0, 70.4, 70.3, 70.3, 62.6, 62.5, 62.4, 30.0, 26.6. ESI MS(m/z): undetected, Calcd for $C_{11}H_{16}O_2$: 180.1150

*(((8-bromooctyl)oxy)methyl)benzene **14a***

To a stirred solution of **13a** (7.9 g, 33.5 mmol) in THF at 0 °C was added *N*-bromosuccinimide (12 g, 67 mmol) and triphenylphosphine (17.5 g, 67 mmol) portionwise. The reaction mixture was then brought to room temperature and stirred for 2 h. After completion, 10 mL MeOH was added to the reaction mixture and the reaction mixture was concentrated to half the initial volume and diluted with *n*-hexane. The precipitate was removed by filtration and the filtrate was concentrated to leave a residue, which was chromatographed (*n*-hexane/EtOAc = 9:1) to give corresponding compound **14a** (9.5 g, 95%) as a colorless oil.

^{1}H NMR (500 MHz, $CDCl_3$) δ 7.24 - 7.36 (m, 5H), 4.50 (s, 2H), 3.46 (t, J = 6.60 Hz, 2H), 3.40 (t, J = 6.84 Hz, 2H), 1.84 (quin, J = 6.96 Hz, 2H), 1.61 (quin, J = 6.84 Hz, 2H), 1.27 - 1.46 (m, 8H). ^{13}C NMR (126 MHz, $CDCl_3$) *δ* 128.3, 127.6, 127.5, 77.3, 77.0, 76.8, 72.9, 70.4, 49.5, 34.0, 32.8, 29.7, 29.2, 28.7, 28.1, 26.1. ESI MS(m/z): undetected, Calcd for $C_{15}H_{23}BrO$: 298.0932

Compound **14b**: colorless oil, 75% yield.

^{1}H NMR (500 MHz, $CDCl_3$) δ 7.23 - 7.37 (m, 5H), 4.50 (s, 2H), 3.50 (t, J = 6.23 Hz, 2H), 3.43 (t, J = 6.72 Hz, 2H), 1.93 - 2.01 (m, 2H), 1.71 - 1.80 (m, 2H). ^{13}C NMR (126 MHz, $CDCl_3$) *δ* 138.5, 128.4, 127.6, 127.6, 72.9, 69.3, 33.8, 29.7, 28.4. ESI MS(m/z): undetected, Calcd for $C_{11}H_{15}BrO$: 242.0306

*(8-(benzyloxy)octyl)triphenylphosphonium **15a***

Triphenylphosphine (14.4 g, 55 mmol) and 13a (5.4 g, 18 mmol) were diluted in CH_2Cl_2 and heated at 80 °C for 24 h. After completion, the solvent was evaporated and the reaction mixture was passed through a short silica gel column eluted first with $CHCl_3$ to remove triphenylphosphine and then with $CHCl_3$/MeOH = 9:1 to give compound **15a** (8.2 g, 81%) as a colorless gel.

^{1}H NMR (500 MHz, $CDCl_3$) δ 7.67 - 7.90 (m, 15H), 7.22 - 7.36 (m, 5H), 4.47 (s, 2H), 3.76 - 3.85 (m, 2H), 3.42 (t, J = 6.60 Hz, 2H), 1.48 - 1.69 (m, 6H), 1.18 - 1.34 (m, 6H). ^{13}C NMR (126 MHz, $CDCl_3$) *δ* 135.0, 135.0, 133.6, 133.5, 130.5, 130.4, 128.3, 127.6, 127.4, 118.6, 117.9, 72.8, 70.4, 49.5, 47.8, 30.3, 30.2, 29.6, 29.0, 28.9, 26.0, 23.0, 22.6. ESI MS(m/z): 481.14 $[M-Br]^+$.

Compound **15b**: white solid, 65% yield.

^{1}H NMR (500 MHz, $CDCl_3$) δ 7.62 - 7.86 (m, 15H), 7.19 - 7.33 (m, 5H), 4.46 (s, 2H), 3.70 - 3.82 (m, 2H), 3.60 (t, J = 5.62 Hz, 2H), 1.94 - 2.07 (m, 2H), 1.73 - 1.89 (m, 2H). ^{13}C NMR (126 MHz, $CDCl_3$) *δ* 138.4, 135.0, 135.0, 134.3, 134.2, 133.6, 133.5, 130.5, 130.4, 130.2, 130.1, 128.3, 127.6, 127.5, 118.5, 117.8, 72.7, 68.8, 29.5, 22.3, 19.6. ESI MS(m/z): 425.08 $[M-Br]^+$.

*(Z)-4-(9-(benzyloxy)non-1-en-1-yl)-1,2-dimethoxybenzene **16a***

In a round bottom flask under nitrogen gas, phosphonium salt **15a** (4 g, 7.12 mmol) and sodium hydride (1.42g, 35.6 mmol; 60% dispersion in mineral oil) were diluted in dry THF (100 mL). The mixture was stirred at 0 °C for 2 h to form a ylide. A solution of 3,4-dimethoxy benzaldehyde (1.54 g, 9.3 mmol) in THF (5 mL) was added to the reaction mixture dropwise. The mixture was then brought to room temperature and stirred for 3 h. The reaction mixture was poured into ice water, acidified with aqueous HCl, and extracted with $CHCl_3$. The organic layer was washed with $NaHCO_3$ and dried to obtain a yellow crude oil. The crude product was purified by silica gel column chromatography (*n*-hexane/EtOAc = 4:1), giving **16a** (1.54 g, 59%) as a yellow oil.

^{1}H NMR (500 MHz, $CDCl_3$) δ 7.20 - 7.37 (m, 5H), 6.78 - 6.92 (m, 3H), 6.33 (d, J = 11.48 Hz, 1H), 5.58 (d, J = 11.73 Hz, 1H), 4.49 (s, 2H), 3.85 - 3.92 (m, 6H), 3.45 (t, J = 6.60 Hz, 2H), 2.33 (dd, J = 1.59, 7.45 Hz, 2H), 1.55 - 1.66 (m, 2H), 1.41 - 1.50 (m, 2H), 1.21 - 1.40 (m, 8H). ^{13}C NMR (126 MHz, $CDCl_3$) *δ* 148.5, 147.7, 138.7, 131.9,

130.8, 128.5, 128.4, 128.3, 127.6, 127.5, 121.3, 112.1, 112.1, 72.9, 70.5, 55.9, 55.8, 30.0, 29.8, 29.8, 29.4, 28.7, 26.2, 26.2. ESI MS(m/z): 390.79 $[M+Na]^+$.

Compound **16b**: yellow oil, 62% yield.

^{1}H NMR (500 MHz, $CDCl_3$) δ 7.23 - 7.38 (m, 5H), 6.78 - 6.90 (m, 3H), 6.30 - 6.39 (m, 1H), 6.08 (td, J = 6.96, 15.63 Hz, 1H), 4.52 (s, 2H), 3.83 - 3.92 (m, 6H), 3.52 (td, J = 6.35, 10.26 Hz, 2H), 2.27 - 2.34 (m, 2H), 1.75 - 1.84 (m, 2H). ^{13}C NMR (126 MHz, $CDCl_3$) *δ* 148.5, 147.8, 138.6, 130.9, 129.0, 128.7, 127.6, 127.6, 127.3, 126.8, 126.3, 121.3, 112.1, 110.9, 72.9, 69.8, 55.9, 55.9, 30.1, 25.4. ESI MS(m/z): 334.97 $[M+Na]^+$.

*9-(3,4-dimethoxyphenyl)nonan-1-ol **17a***

A solution of **16a** (737 mg, 2 mmol) in methanol (25 ml) was hydrogenated over 5% Pd/C (0.3 g) at room temperature under hydrogen gas for 24 h. After completion of the reaction, the catalyst and solvent were removed. The crude product was purified by silica gel column chromatography (*n*-hexane/EtOAc = 3:1) to obtain compound **17a** (488 mg, 87%) as a colorless oil.

^{1}H NMR (500 MHz, $CDCl_3$) δ 6.77 - 6.84 (m, 1H), 6.70 - 6.77 (m, 2H), 3.88 (s, 3H), 3.89 (s, 3H), 3.66 (t, J = 6.60 Hz, 2H), 2.53 - 2.59 (m, 2H), 1.54 - 1.64 (m, 4H), 1.26 - 1.41 (m, 10H). ^{13}C NMR (126 MHz, $CDCl_3$) *δ* 148.7, 146.9, 135.5, 120.1, 111.8, 111.2, 62.5, 55.8, 55.7, 35.5, 32.6, 31.7, 29.5, 29.4, 29.3, 25.8. ESI MS(m/z): 302.93 $[M+Na]^+$.

Compound **17b**: colorless oil, 85% yield.

^{1}H NMR (500 MHz, $CDCl_3$) δ 6.78 - 6.83 (m, 1H), 6.71 - 6.76 (m, 2H), 3.87 (s, 3H), 3.89 (s, 3H), 3.65 (t, J = 6.60 Hz, 2H), 2.56 - 2.61 (m, 2H), 1.58 - 1.70 (m, 4H), 1.37 - 1.46 (m, 2H). ^{13}C NMR (126 MHz, $CDCl_3$) *δ* 148.7, 147.0, 135.2, 120.2, 111.8, 111.7, 62.9, 55.9, 55.8, 49.5, 35.5, 32.6, 25.4. ESI MS(m/z): 246.82 $[M+Na]^+$.

*9-(3,4-dimethoxyphenyl)nonanal **18a***

To a stirred solution of **17a** (420 mg, 1.5 mmol) in 25 ml THF/DMSO (4:1, v/v) was added IBX (840 mg, 3 mmol). The reaction mixture was stirred at 40 °C for 2h. The residue was filtered off, and the filtrate was extracted with EtOAc. The organic layer was dried and evaporated to get the crude product. The purification of the crude

product by silica gel column chromatography (*n*-hexane/EtOAc = 3:1) gave **18a** (342 mg, 82%) as a colorless oil.

^{1}H NMR (500 MHz, $CDCl_3$) δ 9.78 (t, J = 1.95 Hz, 1H), 6.77 - 6.84 (m, 1H), 6.69 - 6.76 (m, 2H), 3.88 (s, 3H), 3.90 (s, 3H), 2.51 - 2.60 (m, 2H), 2.44 (dt, J = 1.95, 7.33 Hz, 2H), 1.63 (td, J = 7.33, 19.06 Hz, 4H), 1.34 (br. s., 8H). ^{13}C NMR (126 MHz, $CDCl_3$) *δ* 202.8, 148.7, 147.0, 135.5, 120.1, 111.7, 111.2, 55.9, 55.8, 43.9, 35.5, 31.6, 29.3, 29.2, 29.1, 22.0. ESI MS(m/z): 300.81 $[M+Na]^+$.

Compound **18b**: colorless oil, 89% yield.

^{1}H NMR (500 MHz, $CDCl_3$) δ 9.74 - 9.80 (m, 1H), 6.80 (d, J = 7.82 Hz, 1H), 6.67 - 6.75 (m, 2H), 3.87 (s, 3H), 3.89 (s, 3H), 2.60 (t, J = 7.08 Hz, 2H), 2.42 - 2.50 (m, 2H), 1.62 - 1.75 (m, 4H). ^{13}C NMR (126 MHz, $CDCl_3$) *δ* 202.5, 148.8, 147.2, 134.6, 120.1, 111.7, 111.2, 55.9, 55.8, 43.7, 35.2, 31.0, 21.6. ESI MS(m/z): 244.72 $[M+Na]^+$.

*1-(2-(benzyloxy)-6-hydroxyphenyl)ethan-1-one **19***

To a stirred solution of 2,6 dihydroxyacetophenone (2.0 g, 13.1 mmol) in DMSO (40 mL) was added sodium hydride (529 mg, 13.1 mmol) portion wise at 0 °C. After 30 min stirring, benzyl bromide (1.6 mL, 13.1 mmol) was added dropwise. The reaction mixture was then brought to room temperature, and stirring was continued for 1 h. The reaction mixture was acidified by cold 1 M HCl and extracted with CH_2Cl_2. The residue was then purified by silica column chromatography (*n*-hexane/EtOAc = 5:1) to obtain compound **19** (2.58 g, 81%) as a yellow solid.

^{1}H NMR (500 MHz, $CDCl_3$) δ13.26 (s, 1H), 7.33 - 7.50 (m, 5H), 6.58 - 6.64 (m, 1H), 6.49 (d, J = 7.82 Hz, 1H), 5.16 (s, 2H), 2.64 (s, 3H). ^{13}C NMR (126 MHz, $CDCl_3$) *δ* 205.1, 164.7, 160.6, 136.1, 135.8, 128.8, 128.5, 127.9, 111.5, 111.0, 102.2, 71.1, 34.0. ESI MS(m/z): 265.09 $[M+Na]^+$.

*1-(2-(benzyloxy)-6-hydroxyphenyl)-11-(3,4-dimethoxyphenyl)-3-hydroxyundecan-1-one **20a***

A solution of **19** (1.1 g, 4.5 mmol) in dry THF was added dropwise to a solution of LDA (18 mL in 1 M THF solution, 18 mmol) over 10 min at -78 °C under nitrogen atmosphere and the mixture was stirred for 2 h to prepare the enolate. A solution of **18a** (1.25 g, 4.5 mmol) and HMPA (0.5 mL) in THF (10 mL) was added to the enolate

and the mixture was stirred for 1 h. The reaction mixture was brought to 0 °C slowly and quenched with 6 M HCl and ice. The mixture was extracted with $CHCl_3$, washed with brine and evaporated under reduced pressure. The crude products were purified by silica column chromatography (*n*-hexane/EtOAc = 5:1) gave compound **20a** (842 mg, 36%) as a light-yellow solid.

^{1}H NMR (500 MHz, $CDCl_3$) δ 13.07 (s, 1H), 7.36 - 7.47 (m, 5H), 6.79 - 6.83 (m, 1H), 6.71 - 6.77 (m, 2H), 6.63 (dd, J = 0.98, 8.31 Hz, 1H), 6.49 - 6.53 (m, 1H), 5.09 - 5.15 (m, 2H), 4.06 - 4.12 (m, 1H), 3.88 (s, 3H), 3.90 (s, 3H), 3.21 (dd, J = 2.20, 18.32 Hz, 1H), 3.03 (dd, J = 9.53, 18.32 Hz, 1H), 2.90 (d, J = 3.42 Hz, 1H), 2.53 - 2.61 (m, 2H), 1.58 - 1.66 (m, 2H), 1.15 - 1.39 (m, 12H). ^{13}CNMR (126 MHz, $CDCl_3$) *δ* 207.5, 164.9, 160.7, 148.7, 147.0, 136.4, 135.6, 135.4, 128.8, 128.7, 128.3, 120.1, 111.8, 111.4, 111.3, 111.2, 102.2, 71.4, 67.6, 55.9, 55.8, 52.1, 36.3, 35.6, 31.7, 29.6, 29.5, 29.3, 25.3. ESI MS(m/z): 543.07 $[M+Na]^+$.

Compound **20b**: light yellow solid, 54% yield.

^{1}H NMR (500 MHz, $CDCl_3$) δ13.06 (s, 1H), 7.35 - 7.49 (m, 5H), 6.76 - 6.85 (m, 1H), 6.67 - 6.76 (m, 2H), 6.62 (d, J = 8.31 Hz, 1H), 6.50 (d, J = 8.31 Hz, 1H), 5.04 - 5.17 (m, 2H), 4.04 - 4.14 (m, 1H), 3.85 - 3.92 (m, 6H), 3.20 (dd, J = 2.20, 18.32 Hz, 1H), 3.03 (dd, J = 9.53, 18.32 Hz, 1H), 2.86 - 2.95 (m, 1H), 2.47 - 2.56 (m, 2H), 1.47 - 1.59 (m, 2H), 1.21 - 1.43 (m, 4H). ^{13}CNMR (126 MHz, $CDCl_3$) *δ* 207.3, 164.9, 160.6, 148.8, 147.1, 136.5, 135.5, 135.4, 128.8, 128.7, 128.3, 120.1, 111.7, 111.4, 111.3, 111.2, 102.3, 71.4, 67.5, 55.9, 55.8, 52.1, 49.5, 36.1, 35.5, 31.7, 25.0. ESI MS(m/z): 486.92 $[M+Na]^+$.

(E)-1-(2-(benzyloxy)-6-hydroxyphenyl)-11-(3,4-dimethoxyphenyl)undec-2-en-1-one

21a

A catalytic amount of *p*-TsOH was added to a solution of **20a** (853 mg, 1.64 mmol) in toluene (20 mL). The mixture was heated at 80 °C for 2 h with occasional monitoring by TLC. After completion, the mixture was poured into cold water and extracted with ether. The organic layer was then washed with a saturated $NaHCO_3$ and concentrated to obtain a yellow crude. The crude product was purified by silica gel column chromatography (*n*-hexane/EtOAc = 4:1) gave compound **21a** (420 mg, 51%) as a yellow solid.

^{1}H NMR (500 MHz, $CDCl_3$) δ13.12 (s, 1H), 7.32 - 7.48 (m, 5H), 7.17 - 7.23 (m, 1H), 7.00 - 7.08 (m, 1H), 6.79 - 6.83 (m, 1H), 6.71 - 6.77 (m, 2H), 6.63 (dd, J = 0.98, 8.31 Hz, 1H), 6.50 (d, J = 8.31 Hz, 1H), 5.12 (s, 2H), 3.87 (s, 3H), 3.89 (s, 3H), 2.55 - 2.61 (m, 2H), 2.09 (d, J = 6.35 Hz, 2H), 1.62 (t, J = 7.33 Hz, 2H), 1.22 - 1.39 (m, 10H). ^{13}C NMR (126 MHz, $CDCl_3$) δ 195.0, 164.9, 160.1, 148.8, 147.9, 147.0, 135.9, 135.7, 135.6, 131.1, 128.6, 128.3, 127.9, 120.1, 111.8, 111.8, 111.2, 111.1, 102.6, 71.2, 55.9, 55.8, 35.6, 32.6, 31.7, 29.5, 29.4, 29.3, 29.3, 28.1. ESI MS(m/z): 525.13 $[M+Na]^+$.

Compound **21b**: yellow solid, 60% yield.

^{1}H NMR (500 MHz, $CDCl_3$) δ 13.06 (s, 1H), 7.33 - 7.49 (m, 5H), 7.17 (s, 1H), 6.95 - 7.08 (m, 1H), 6.80 (d, J = 8.31 Hz, 1H), 6.66 - 6.75 (m, 2H), 6.63 (d, J = 8.31 Hz, 1H), 6.49 (d, J = 8.31 Hz, 1H), 5.12 (s, 2H), 3.87 (s, 3H), 3.88 (s, 3H), 2.51 (t, J = 7.82 Hz, 2H), 2.12 (q, J = 7.17 Hz, 2H), 1.50 - 1.61 (m, 2H), 1.37 (quin, J = 7.45 Hz, 2H). ^{13}C NMR (126 MHz, $CDCl_3$) δ 195.0, 164.9, 160.1, 148.8, 147.5, 147.1, 135.9, 135.8, 135.0, 131.3, 128.6, 128.3, 127.8, 120.1, 111.7, 111.2, 111.1, 102.6, 71.1, 55.9, 55.8, 35.3, 32.5, 31.2, 27.6. ESI MS(m/z): 469.02 $[M+Na]^+$.

1-(2,6-dihydroxyphenyl)-11-(3,4-dimethoxyphenyl)undecan-1-one ***22a***

Compound **21a** (400 mg, 0.79 mmol) in acetone (20 mL) was hydrogenated over 5% Pd/C for 3 h under hydrogen gas. After completion, the catalyst and solvent were removed. The crude product was purified by silica gel column chromatography (*n*-hexane/EtOAc = 3:1) to obtain **22a** (235 mg, 71%) as a light yellow solid.

^{1}H NMR (500 MHz, $CDCl_3$) δ 9.97 (br. s., 1H), 7.21 (t, J = 8.06 Hz, 1H), 6.79 - 6.84 (m, 1H), 6.71 - 6.76 (m, 2H), 6.40 (d, J = 8.31 Hz, 2H), 3.86 (s, 3H), 3.88 (s, 3H), 3.15 (t, J = 7.57 Hz, 2H), 2.53 - 2.59 (m, 2H), 1.67 - 1.76 (m, 2H), 1.56 - 1.64 (m, 2H), 1.24 - 1.41 (m, 12H). ^{13}C NMR (126 MHz, $CDCl_3$) δ 208.2, 161.3, 148.6, 146.8, 135.8, 135.7, 120.3, 111.9, 111.3, 110.1, 108.3, 55.9, 55.8, 44.8, 35.6, 31.7, 29.5, 29.5, 29.5, 29.5, 29.4, 29.2, 24.5. ESI MS(m/z): 437.02 $[M+Na]^+$.

Compound **22b**: yellow solid, 88% yield.

^{1}H NMR (500 MHz, $CDCl_3$) δ 9.34 (br. s., 1H), 7.23 (t, J = 8.31 Hz, 1H), 6.77 - 6.84 (m, 1H), 6.70 - 6.76 (m, 2H), 6.39 (d, J = 7.82 Hz, 2H), 3.87 (s, 3H), 3.89 (s, 3H), 3.12 (t, J = 7.33 Hz, 2H), 2.57 (t, J = 7.82 Hz, 2H), 1.68 - 1.78 (m, 2H), 1.63 (quin, J = 7.45 Hz, 2H), 1.36 - 1.46 (m, 4H). ^{13}C NMR (126 MHz, $CDCl_3$) δ 208.1, 161.4, 148.6,

146.9, 135.8, 135.7, 120.3, 111.9, 111.3, 110.1, 108.3, 55.9, 55.8, 44.7, 35.5, 31.5, 29.2, 29.1, 24.4. ESI MS(m/z): 380.93 $[M+Na]^+$.

*1-(2,6-dihydroxyphenyl)-11-(3,4-dihydroxyphenyl)undecan-1-one **11***

Boron tribromide (340 mL, 3.57 mmol) was added to a stirred solution of **22a** (298 mg, 0.72 mmol) in CH_2Cl_2 (10 mL) at 0 °C, and the mixture was allowed to warm to room temperature and then stirred for 30 min. After completion of the reaction, the mixture was poured into ice water and extracted with EtOAc. The organic layer was then washed with a saturated $NaHCO_3$ and concentrated to obtain a yellow crude. The products were purified by silica gel column chromatography (*n*-hexane/EtOAc = 4:1) giving **11** (125 mg, 45%) as a light-yellow solid.

^1H NMR (500 MHz, CD_3OD) δ 7.17 (t, J = 8.06 Hz, 1H), 6.66 (d, J = 7.82 Hz, 1H), 6.61 (d, J = 1.95 Hz, 1H), 6.47 (dd, J = 1.95, 7.82 Hz, 1H), 6.34 (d, J = 8.31 Hz, 2H), 3.02 - 3.16 (m, 2H), 2.38 - 2.46 (m, 2H), 1.66 (t, J = 7.08 Hz, 2H), 1.53 (t, J = 7.08 Hz, 2H), 1.30 - 1.39 (m, 4H), 1.28 (br. s., 8H). ^{13}C NMR (125 MHz, CD_3OD) δ 208.3, 162.0, 144.5, 142.6, 135.4, 134.4, 119.3, 115.1, 114.8, 110.0, 107.0, 44.4, 34.9, 31.5, 29.4, 29.3, 29.3, 29.2, 29.0, 24.4. ESI MS(m/z): 409.06 $[M+Na]^+$.

Compound **12**: light yellow solid, 56% yield.

^1H NMR (500 MHz, CD_3OD) δ 7.13 - 7.21 (m, 1H), 6.66 (d, J = 7.82 Hz, 1H), 6.62 (d, J = 1.95 Hz, 1H), 6.48 (dd, J = 1.95, 7.82 Hz, 1H), 6.34 (d, J = 8.31 Hz, 2H), 3.09 (t, J = 7.57 Hz, 2H), 2.43 (t, J = 7.57 Hz, 2H), 1.65 (t, J = 7.33 Hz, 2H), 1.48 - 1.59 (m, 2H), 1.26 - 1.42 (m, 4H). ^{13}C NMR (125 MHz, CD_3OD) δ 208.3, 162.0, 144.5, 142.6, 135.5, 134.4, 119.3, 115.1, 114.8, 110.0, 107.0, 44.4, 34.8, 31.4, 29.0, 28.8, 24.3. ESI MS(m/z): 353.21 $[M+Na]^+$

Compounds

Malabaricone C and its derivatives were prepared using the described method. Molnupravir was purchased from Angene Chemical, and remdesivir was purchased from MedChemExpress. All compounds were diluted in dimethyl sulfoxide (DMSO) for *in vitro* experiments.

Generation of TMPRSS2- and ACE2- expressing cells

Vero E6 cells stably expressing human TMPRSS2 (VeroE6/TMPRSS2) and HEK293TA cells stably expressing human ACE2 were described previously (Sasaki et al. PLoS Pathogens 2021) (Uemura et al. Scientific Reports 2021). MA104T cells stably expressing human TMPRSS2 were established from an African green monkey kidney-derived cell line MA104 (RCB0994, RIKEN BRC, Japan) by lentiviral vector transduction with CSII-CMV-TMPRSS2-IRES2-Bsd. For the preparation of the lentiviral particles, the aforementioned lentiviral vector plasmid and Lentiviral High Titer Packaging Mix (Takara Bio, Shiga, Japan) were transfected into Lenti-X 293T cells with TransIt-293 transfection reagent (Mirus Bio, Madison, WI).

Generation of HEK293TA-G and HEK293TA-M cells

The AcGFP1 and mCherry coding sequences were subcloned to pLVSIN-CMV Pur and pLVSIN-CMV Neo (Takara Bio). The resultant plasmids were used for the lentiviral vector preparation as described above.

Virus

SARS-CoV-2 strain WK-521 (Ancestral, Pango Lineage: A, GISAID: EPI_ISL_408667), QK002 (Alpha, Pango Lineage: B.1.1.7, GISAID: EPI_ISL_768526), TY7-501 (Gamma, Pango Lineage: P.1, GISAID: EPI_ISL_833366), TY11-927 (Delta, Pango Lineage: B.1.617.2, GISAID: EPI_ISL_2158617), were provided by the National Institute of Infectious Diseases, Tokyo, Japan. The virus stock was propagated in Vero E6/TMPRSS2 cells and titrated by inoculating Vero E6/TMPRSS2 cells in a 96-well plate with five-fold serial dilutions of the virus, and CPE was scored to calculate the $TCID_{50}$/ml.

Persistent SARS-CoV-2 infection in cells

MA104T cells were infected with SARS-CoV-2 (WK-521) and cultured with an exchanging medium on a regular basis. After apparent CPE (cytopathic effect), the survived cells were maintained with a regular medium exchange for about four weeks. The MA104T cells persistently infected with SARS-CoV-2 were able to proliferate and continuously released infectious SARS-CoV-2.

SARS-CoV-2 Entry Inhibition MTT Assay

The MTT (3-(4,5-di-methylthiazol-2-yl)-2,5-diphenyltetrazolium bromide, yellow tetrazol)(5 mg/mL; Nacalai tesque) assay was performed to evaluate cell viability following viral infection. VeroE6/TMPRSS2 or HEK293TA cells ($2.0 – 2.5 \times 10^4$ cells/mL) were plated on 96-well microplates in MEM containing 2% FBS and the test compounds. Either WT or variants of SARS-CoV-2 (50 μL/well) were added to the plates and then the cells were cultured for 2 – 3 days. Subsequently, MTT test solution was added to each well and then the cells were incubated for 4 – 6 hours. After removing the solution and adding cytolysis solution to each well, the plate was incubated at room temperature for overnight. Absorbance at a wavelength of 570 nm and reference wavelength of 630 nm was measured using Multiskan microplate reader, (Thermo Fisher Scientific), and then the 50% effective concentration (EC_{50}) was calculated. Cell toxicity was assessed under the same method of viral inhibitory assay, and the 50% cytotoxicity concentration (CC_{50}) was calculated.

SARS-CoV-2 Fusion Inhibition Assay

SARS-CoV-2 persistently infected cells were seeded at 100 μL ($1x10^4$ cells)/well into a 96-well plate containing the inhibitors, then reacted at room temperature for 1 hour. Subsequently, HEK293TA-G cells at 50 μL ($5x10^4$ cells)/well and HEK293TA-M cells at 50 μL ($5x10^4$ cells) /well were added to each well, mixed with a plate mixer, and then cultured in a CO_2 incubator for 24 hours. By cell fusion of SARS-CoV-2 persistently infected cells, HEK293TA-G cells (green fluorescence), and HEK293TA-M cells (red fluorescence), hypertrophy cells were formed and emit yellow fluorescence. The cell fusion inhibitory effect was evaluated using the number and the total area of cells emitting yellow fluorescence as indexes. The measurement of fluorescent cells was carried out using an all-in-one fluorescence microscope BZ-X800 (manufactured by KEYENCE).

^{1}H NMR of **Malabaricone C**

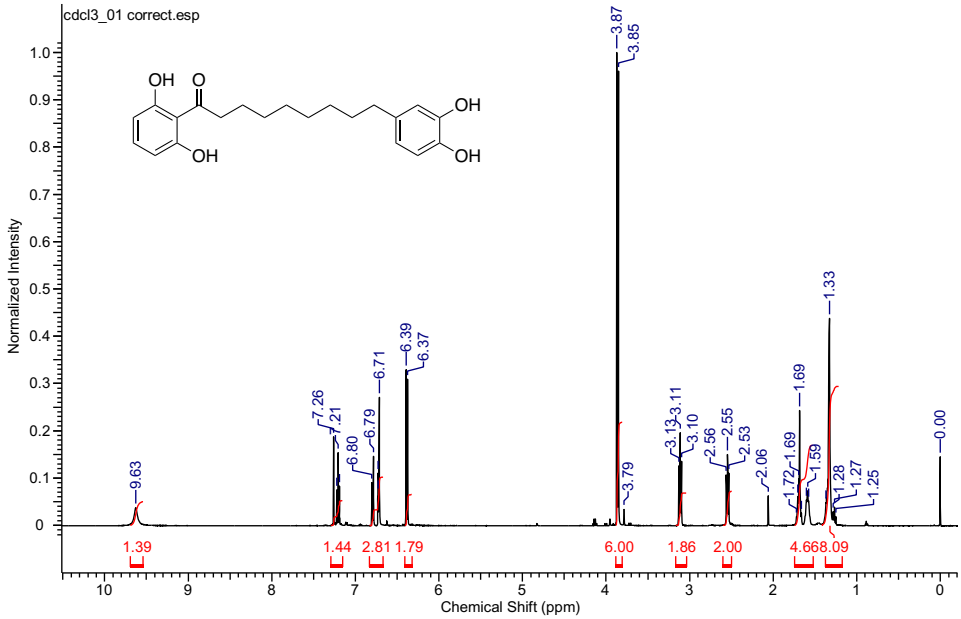

^{1}H and ^{13}C NMR of **2**

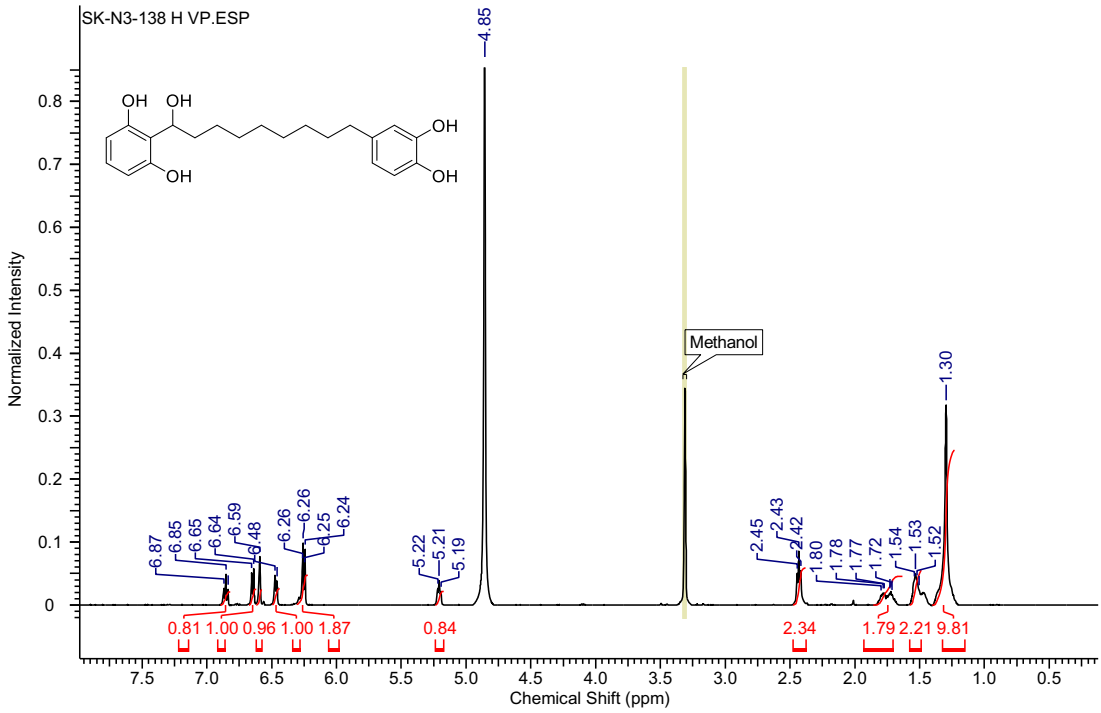

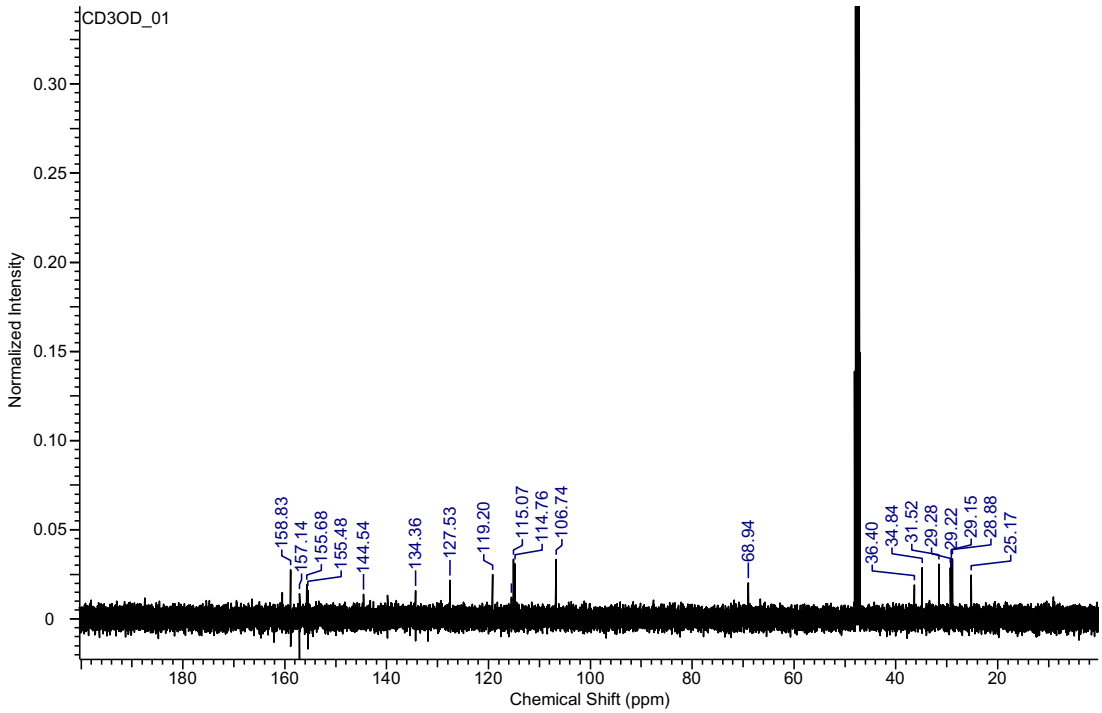

^{1}H and ^{13}C NMR of **3**

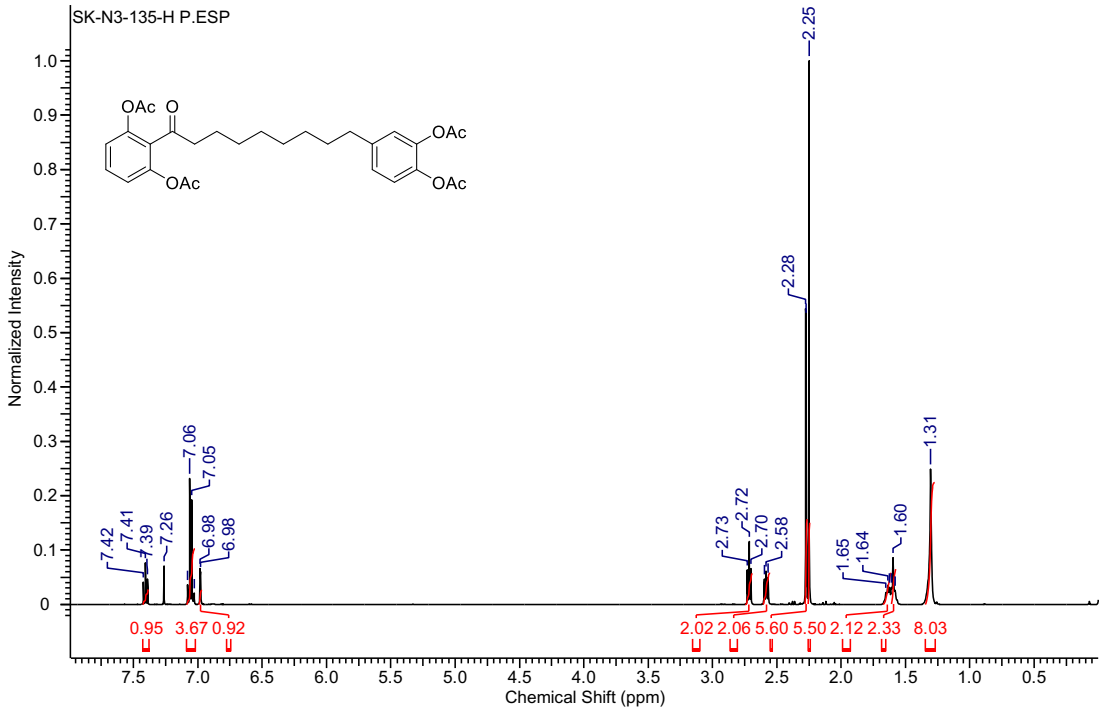

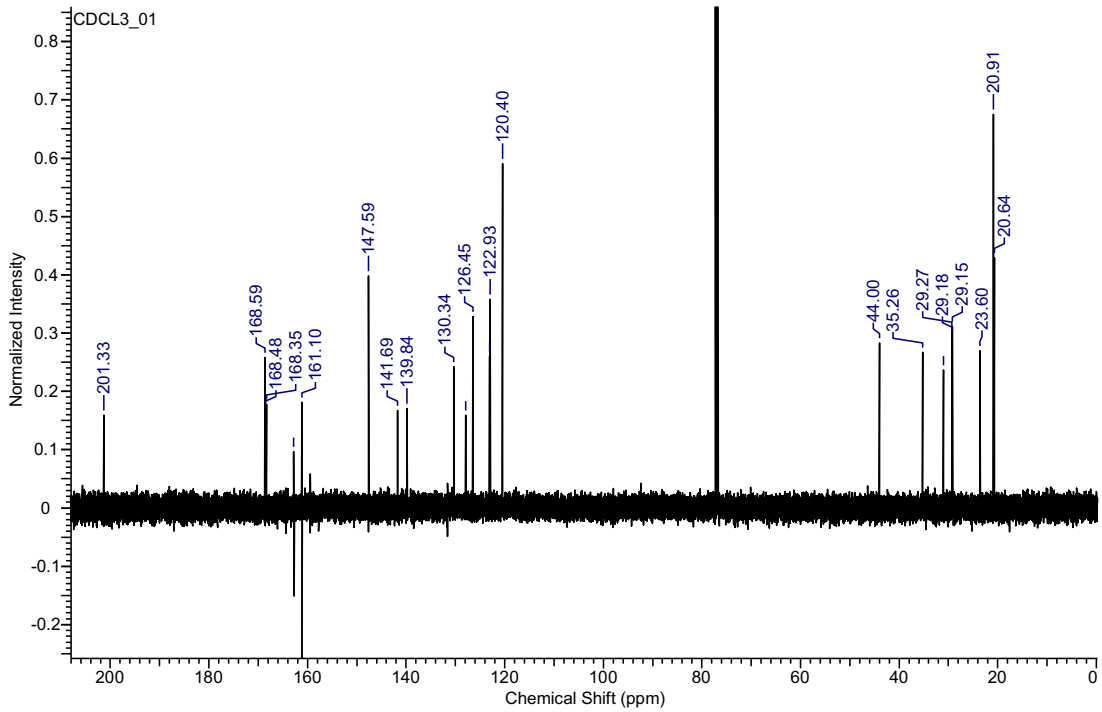

^{1}H and ^{13}C NMR of **4**

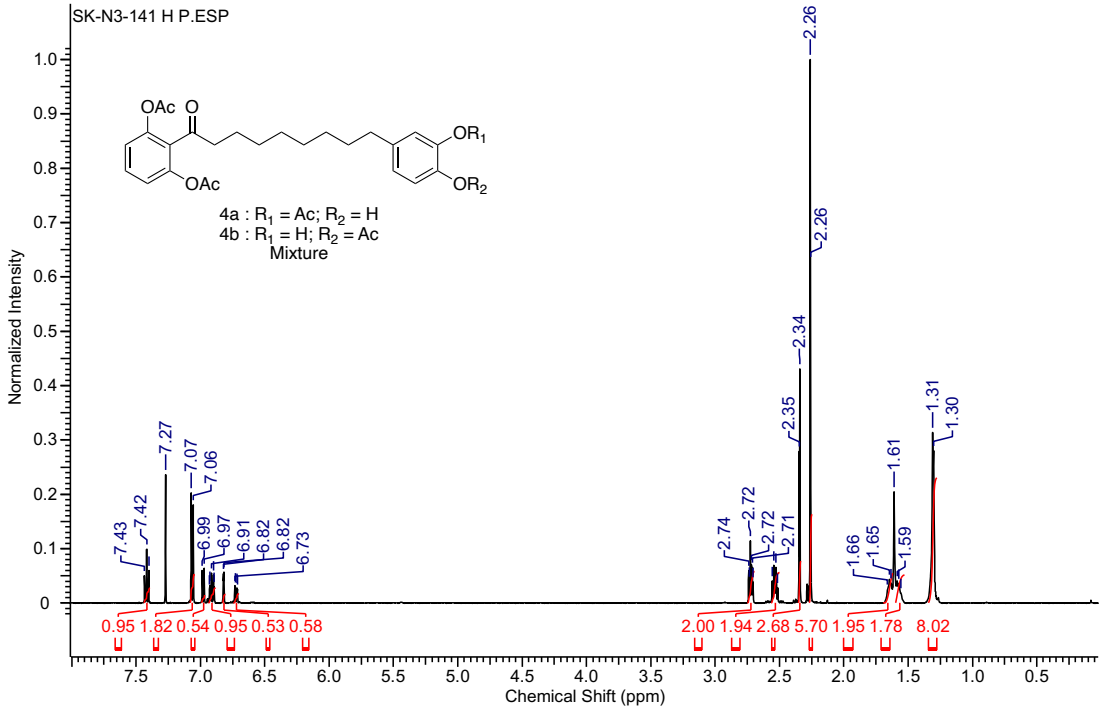

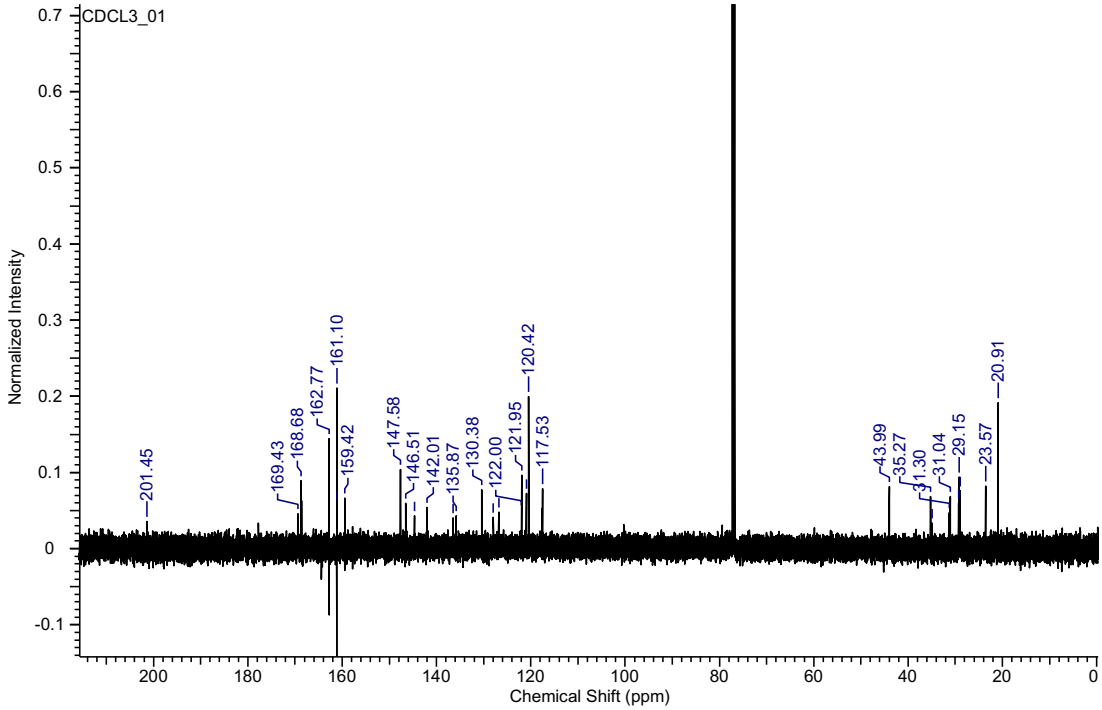

^{1}H and ^{13}C NMR of **5**

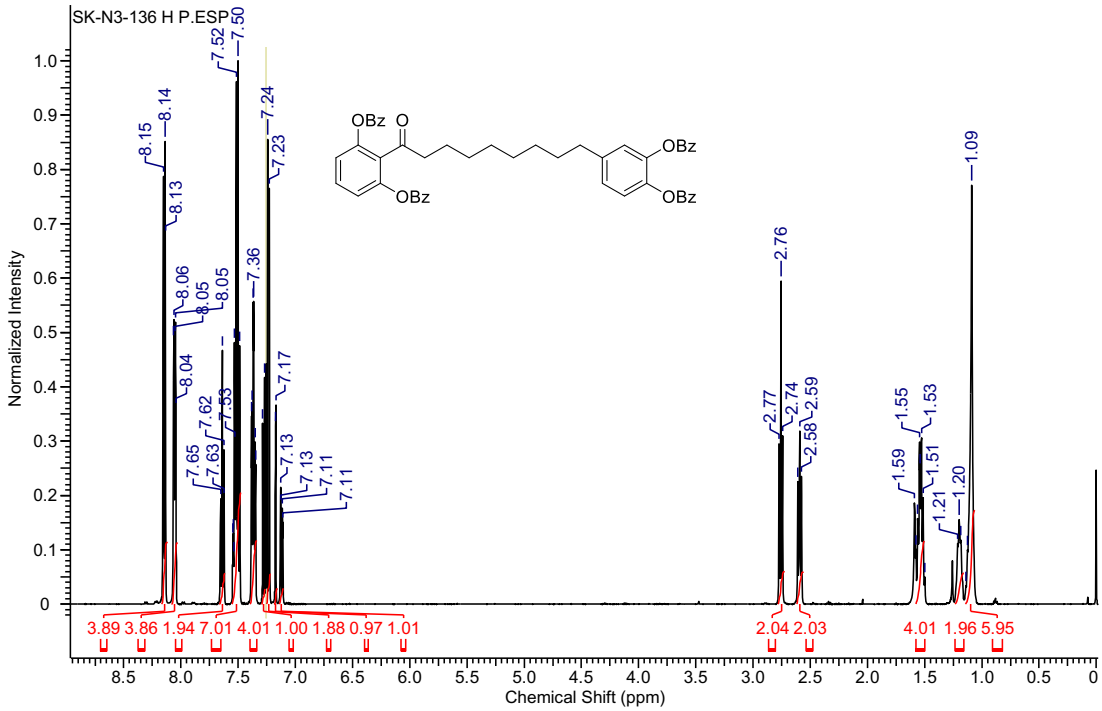

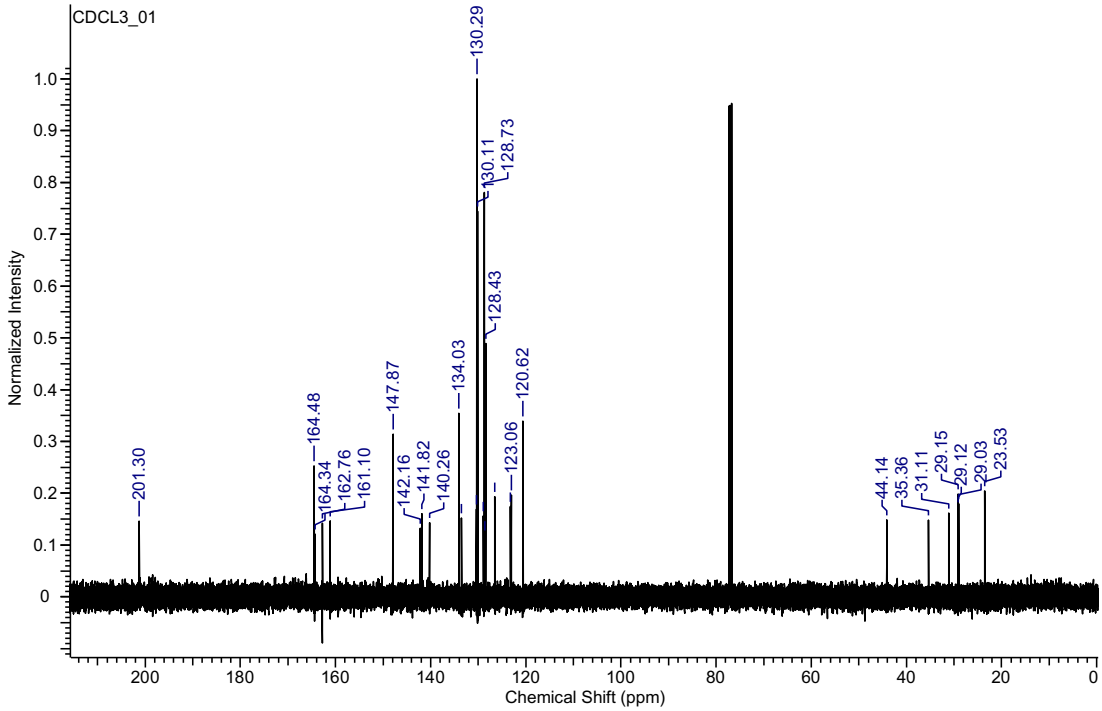

^{1}H and ^{13}C NMR of **6**

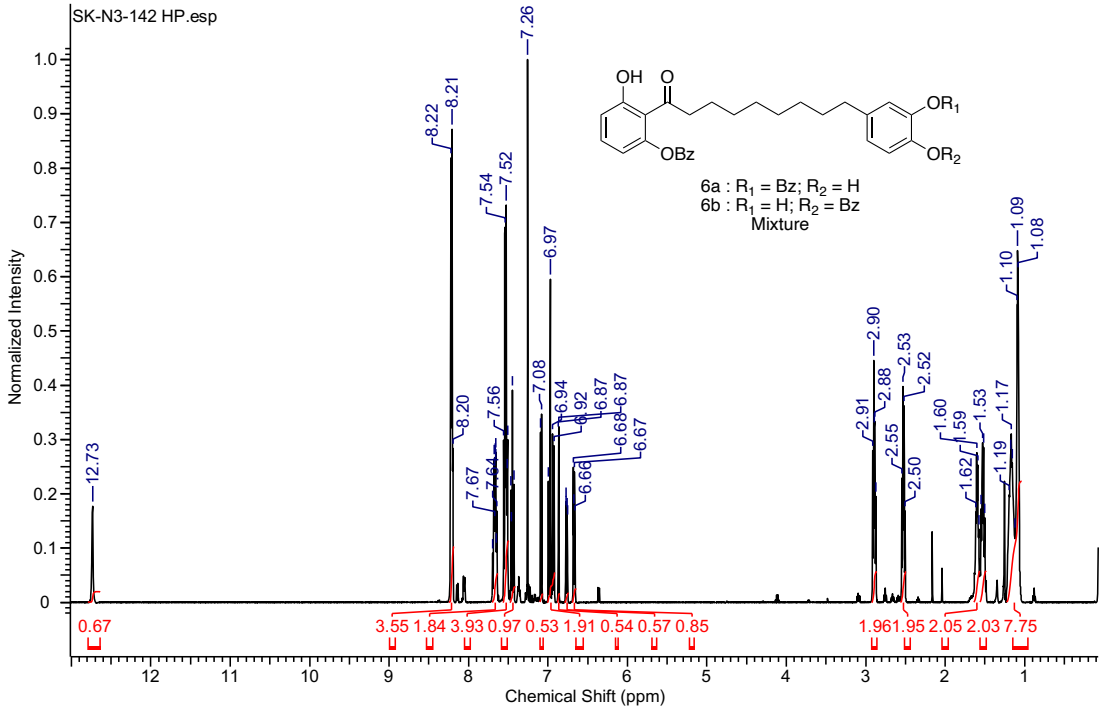

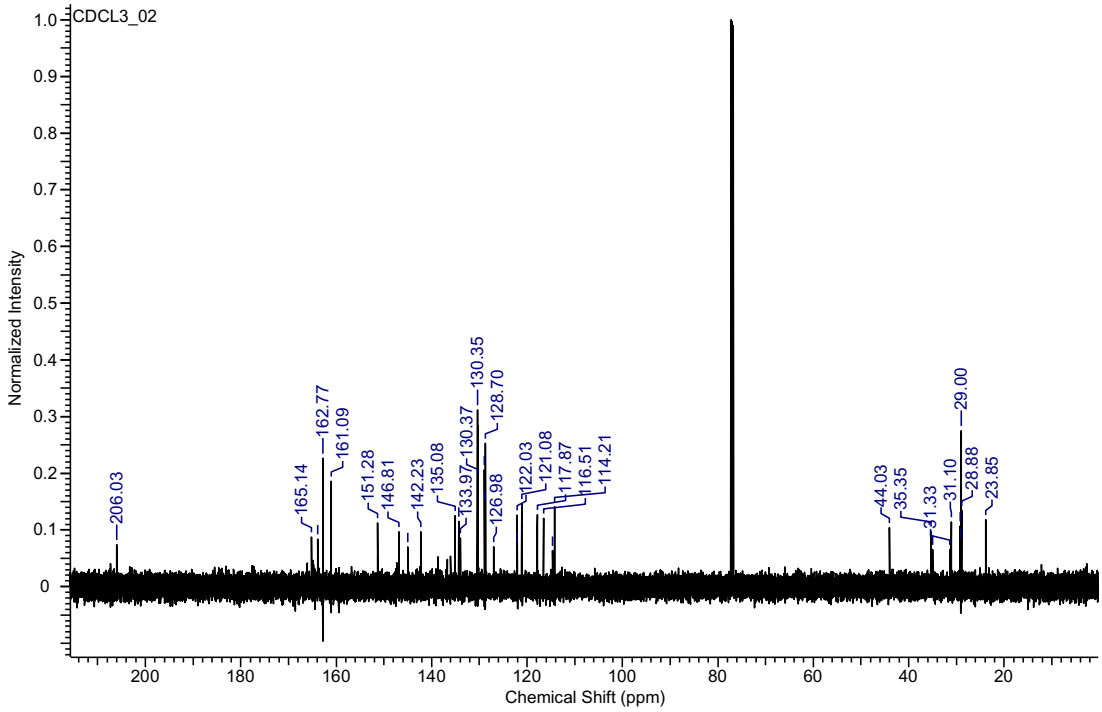

^{1}H and ^{13}C NMR of **7**

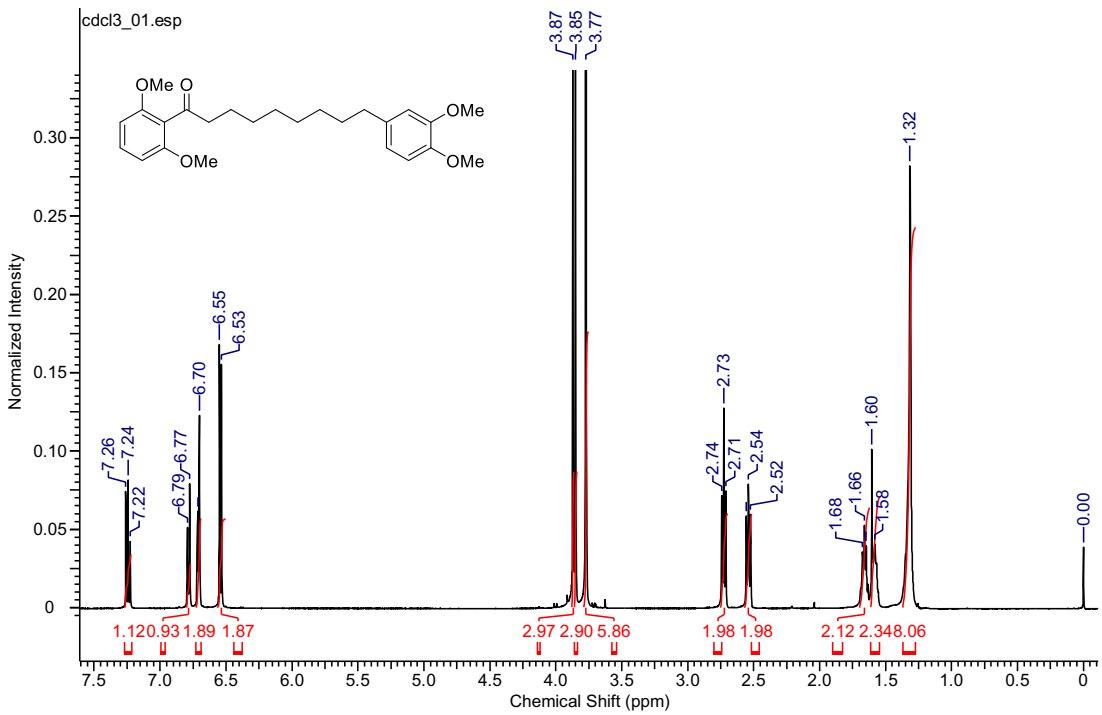

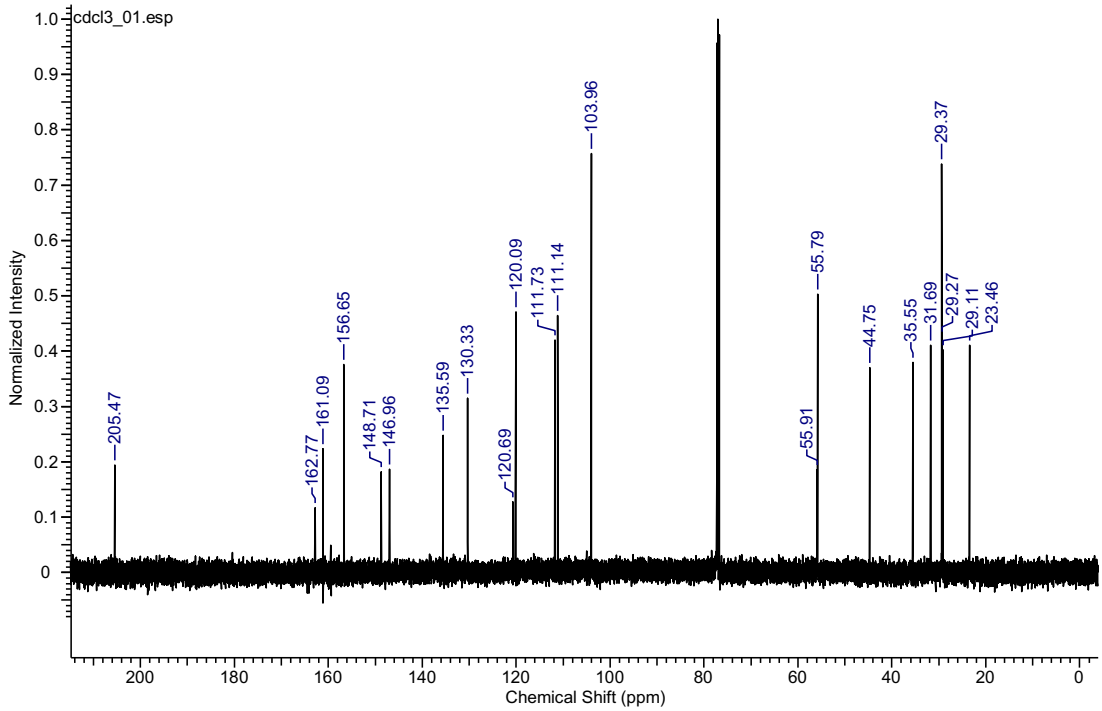

^{1}H and ^{13}C NMR of **8**

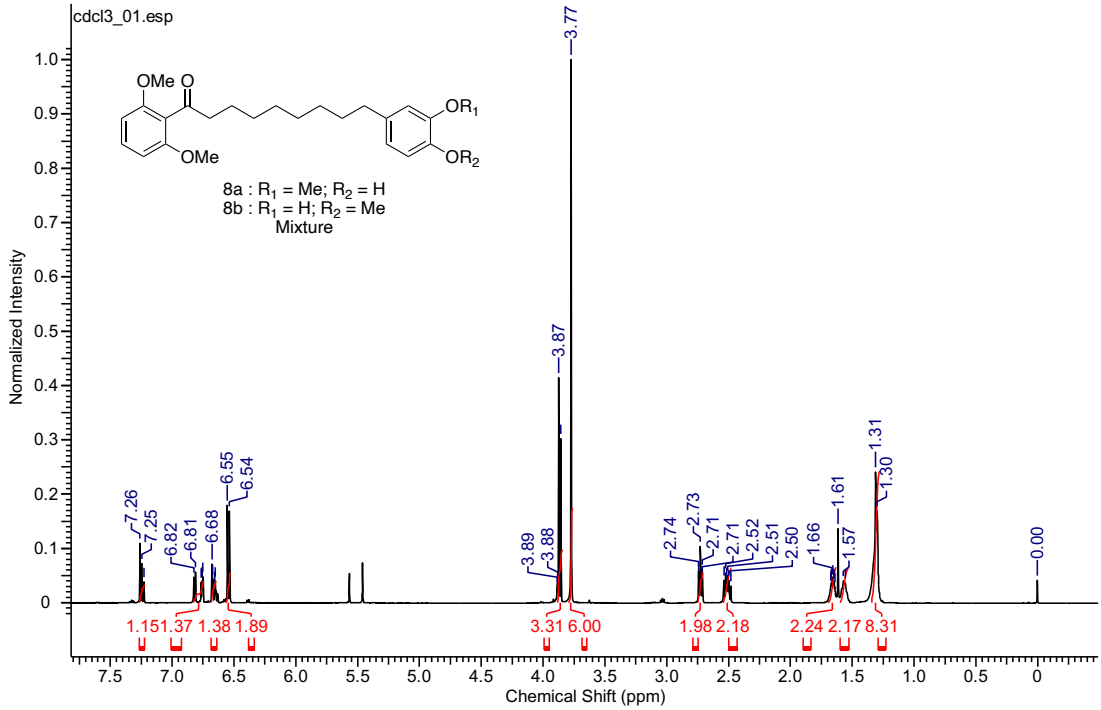

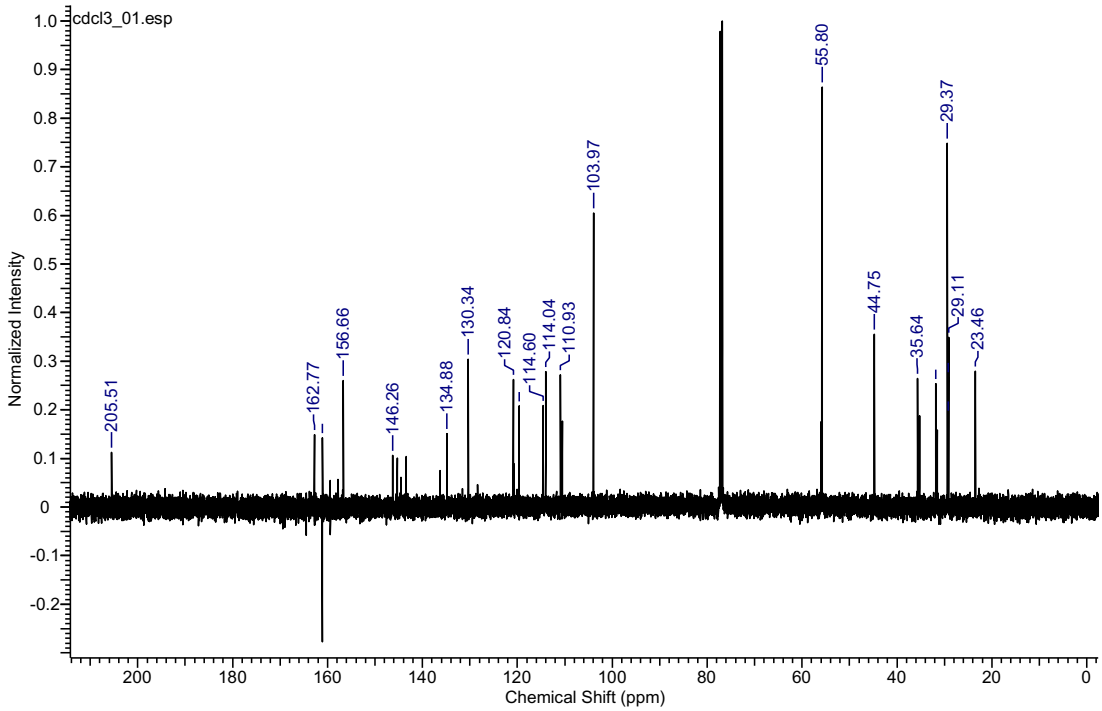

^{1}H and ^{13}C NMR of **9**

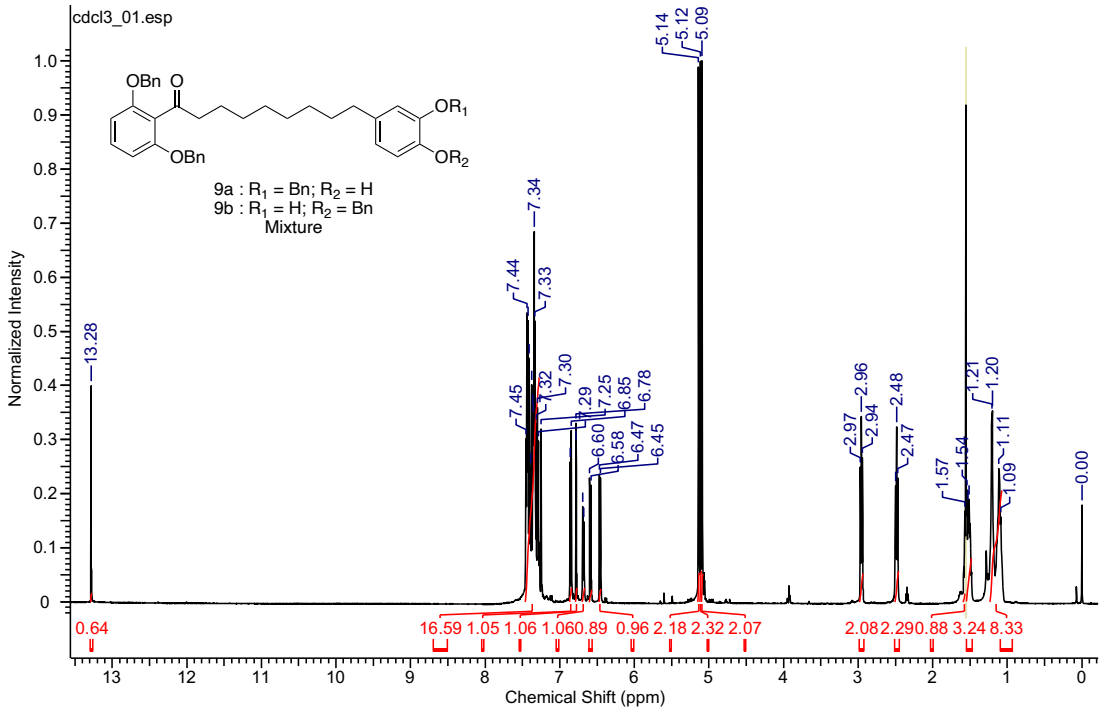

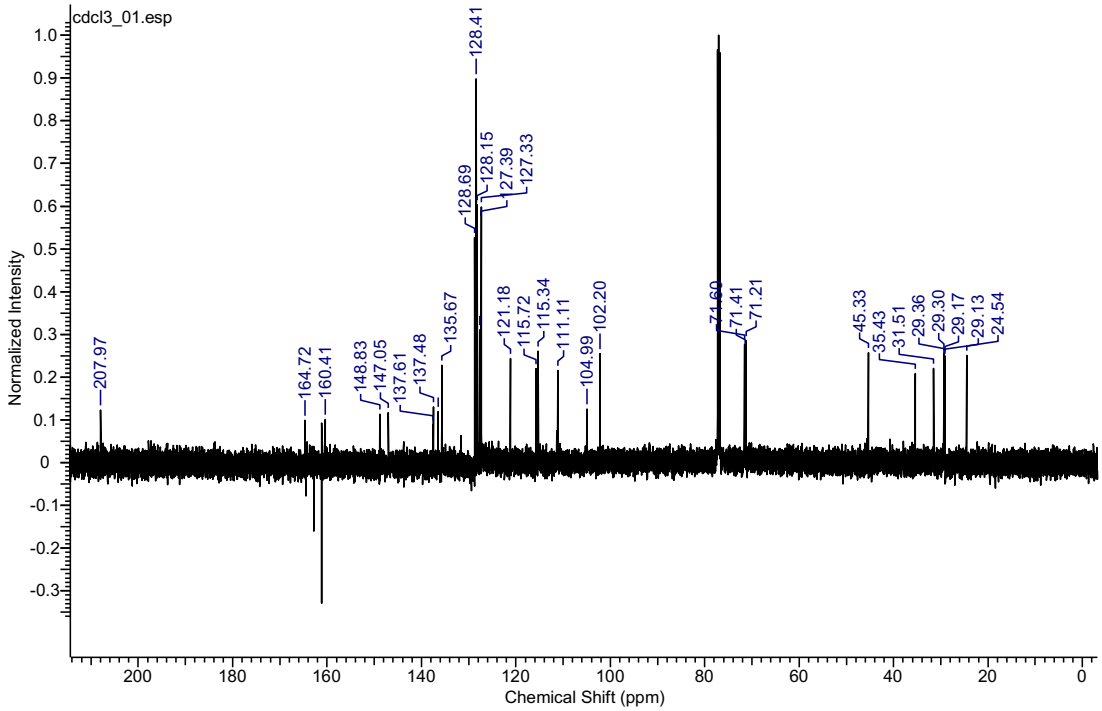

^{1}H and ^{13}C NMR of **10**

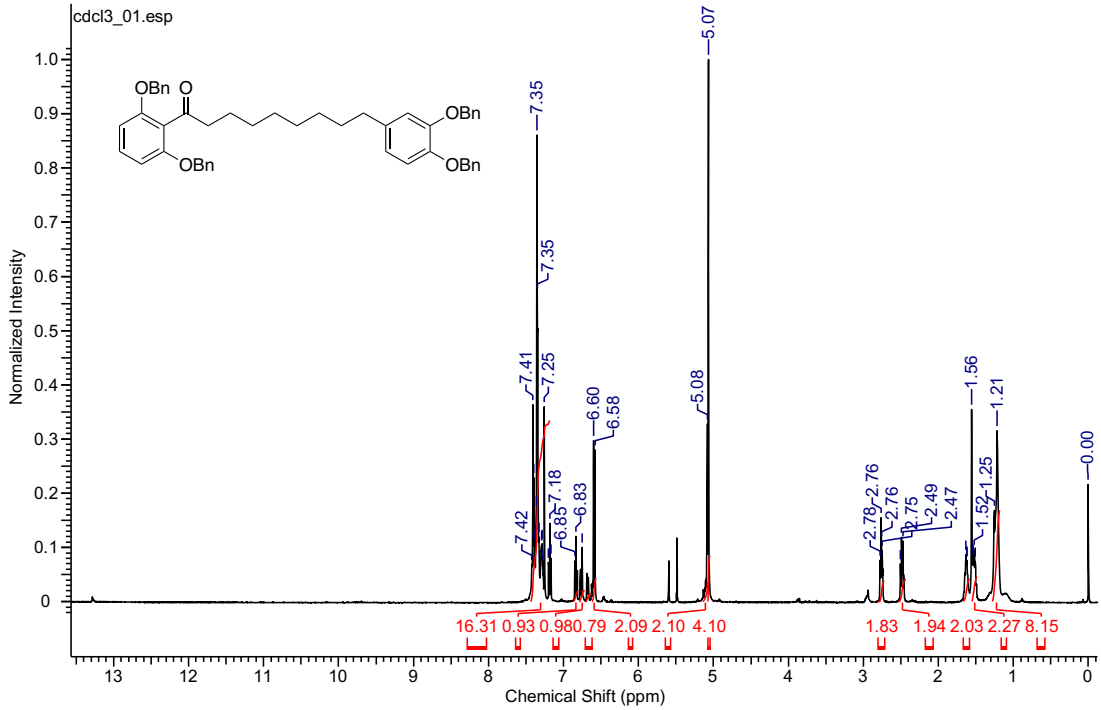

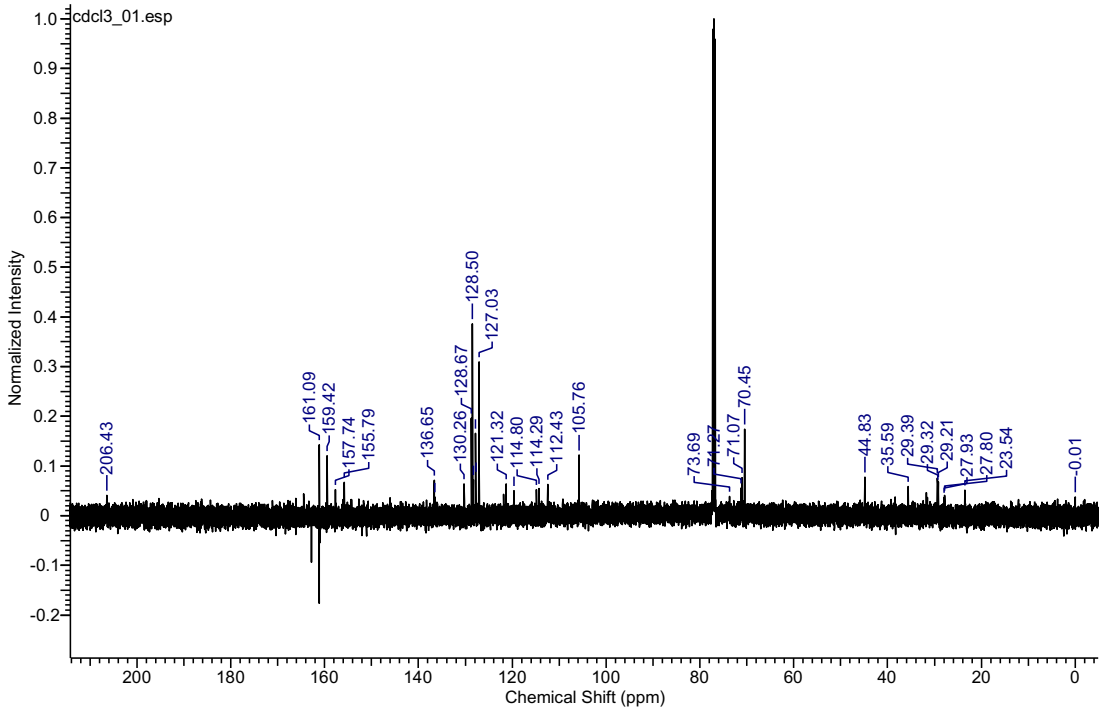

^{1}H and ^{13}C NMR of **11**

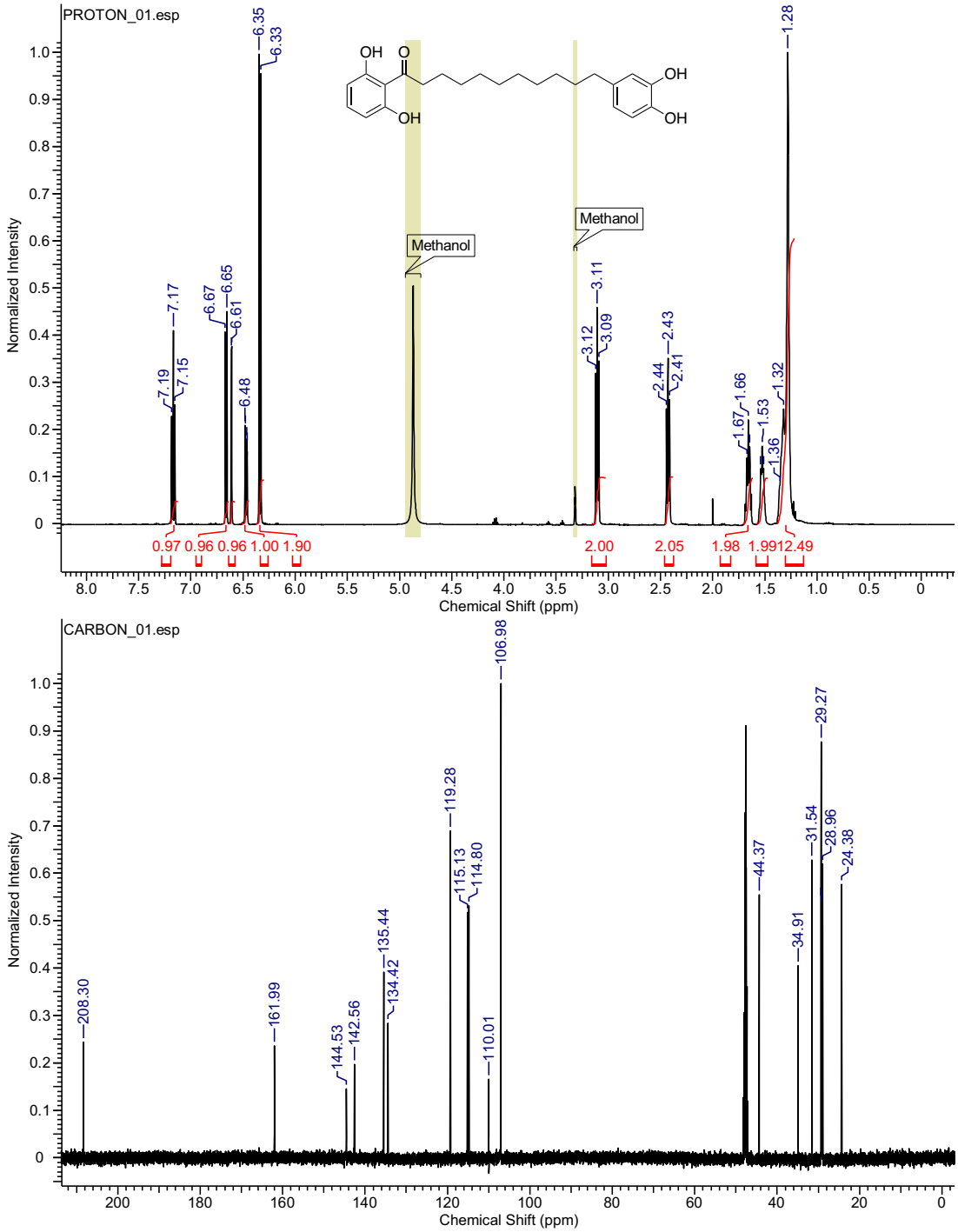

^{1}H and ^{13}C NMR of **12**

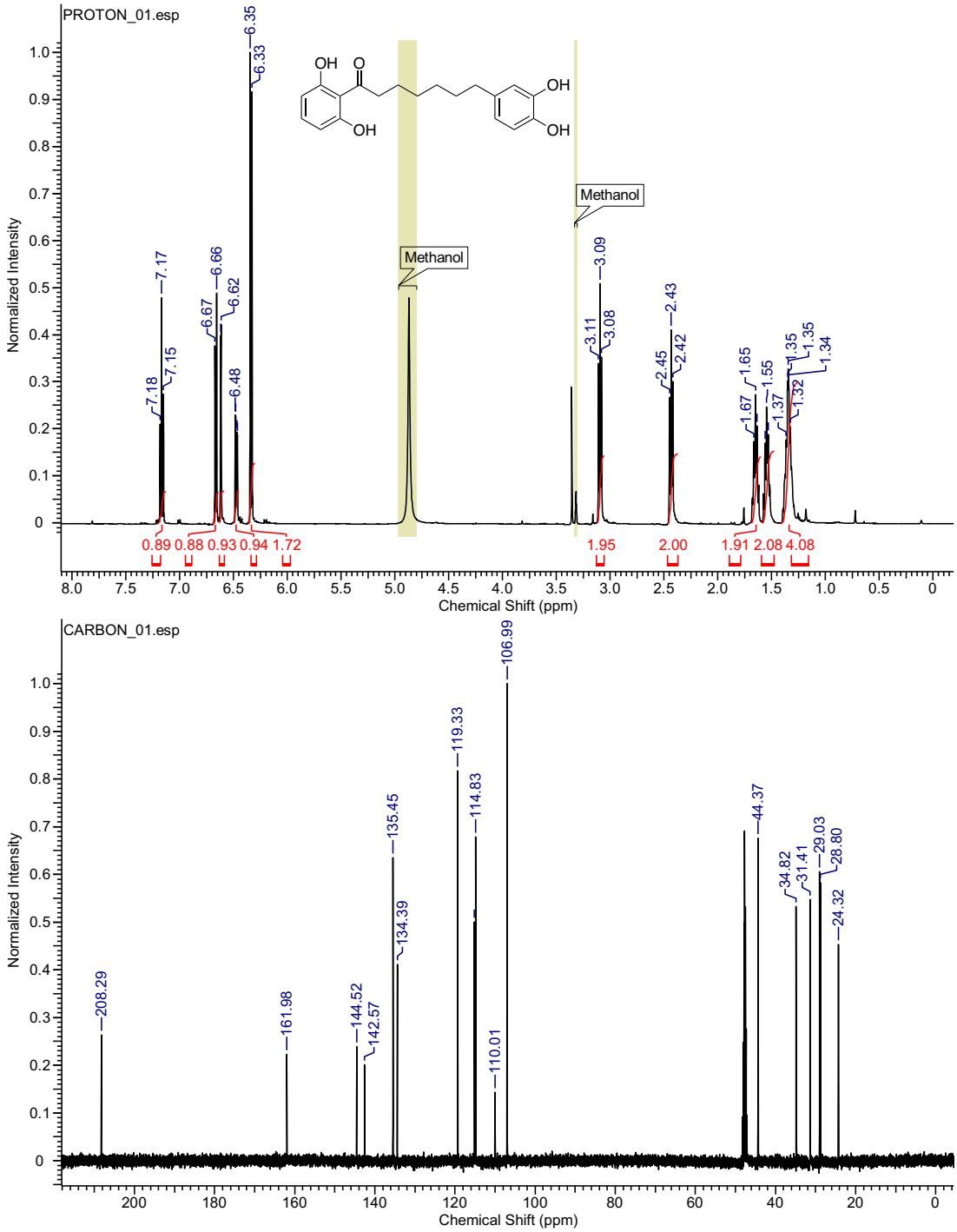

^{1}H and ^{13}C NMR of **13a**

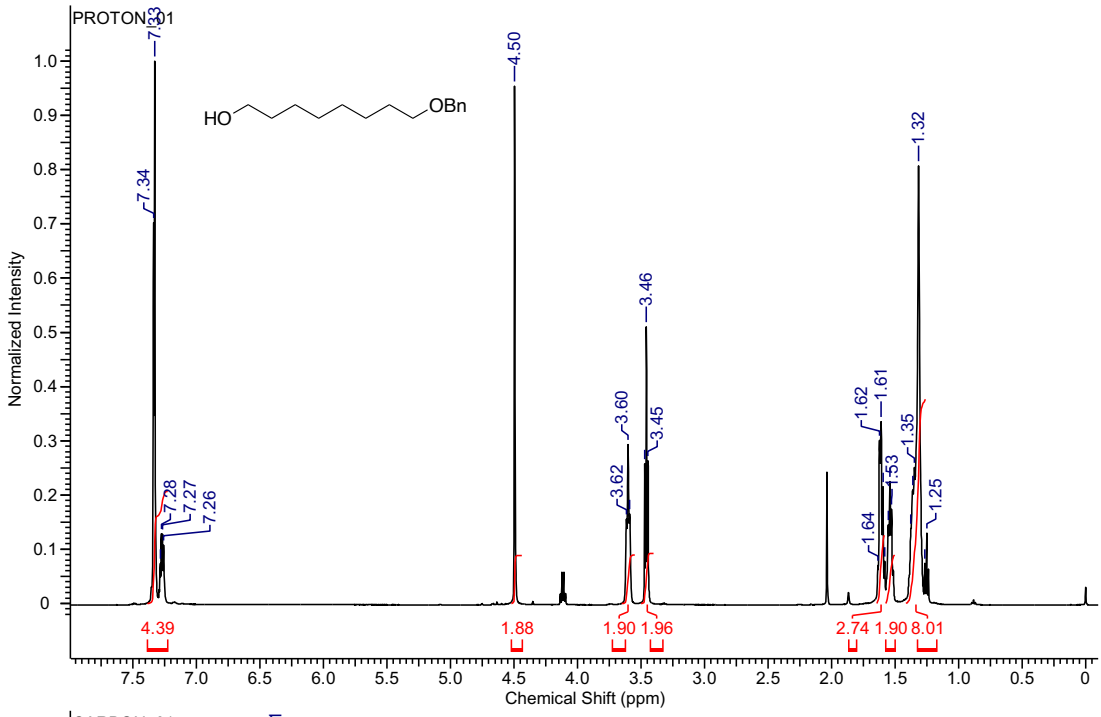

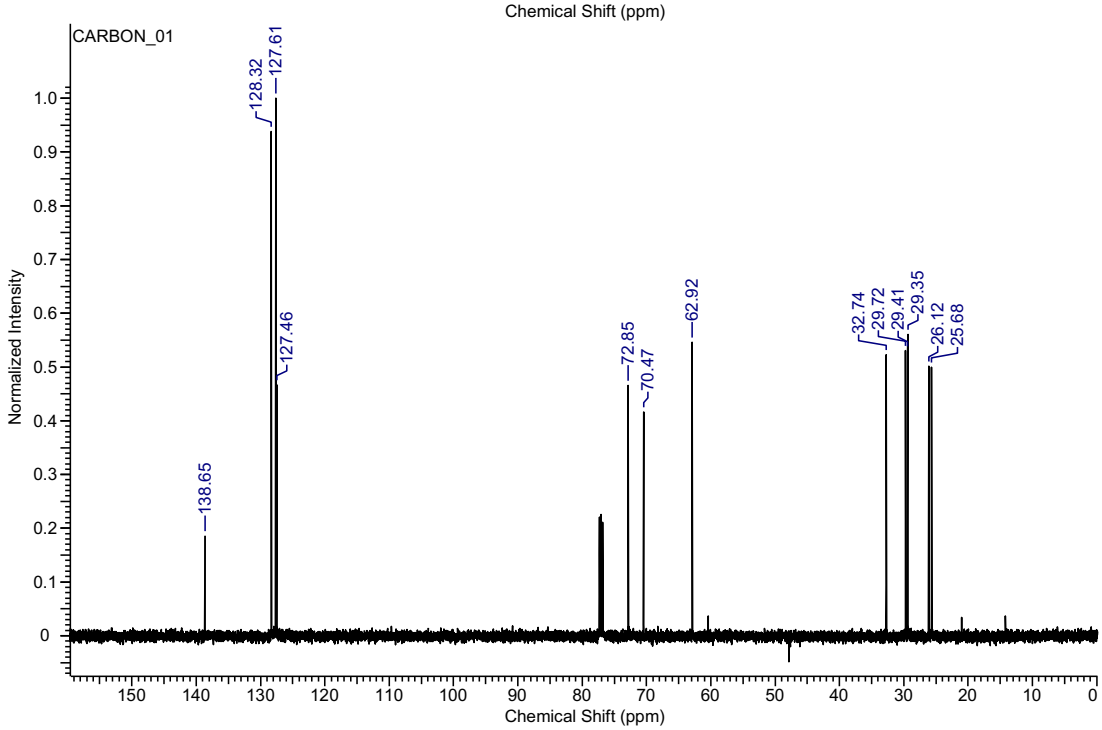

^{1}H and ^{13}C NMR of **13b**

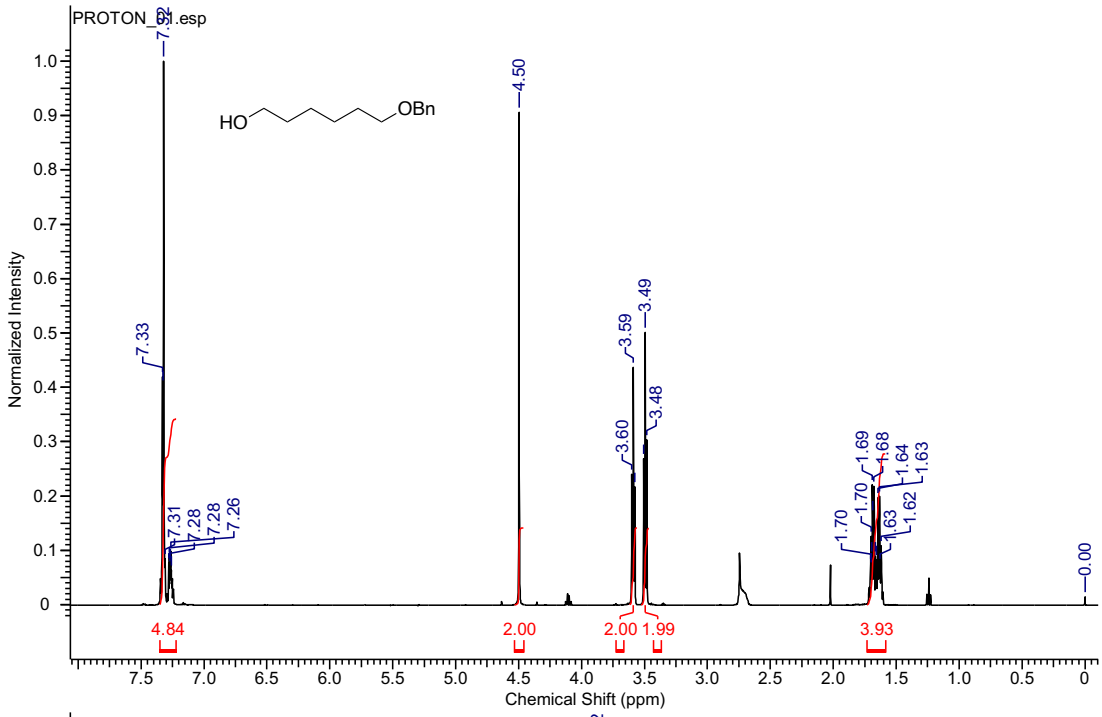

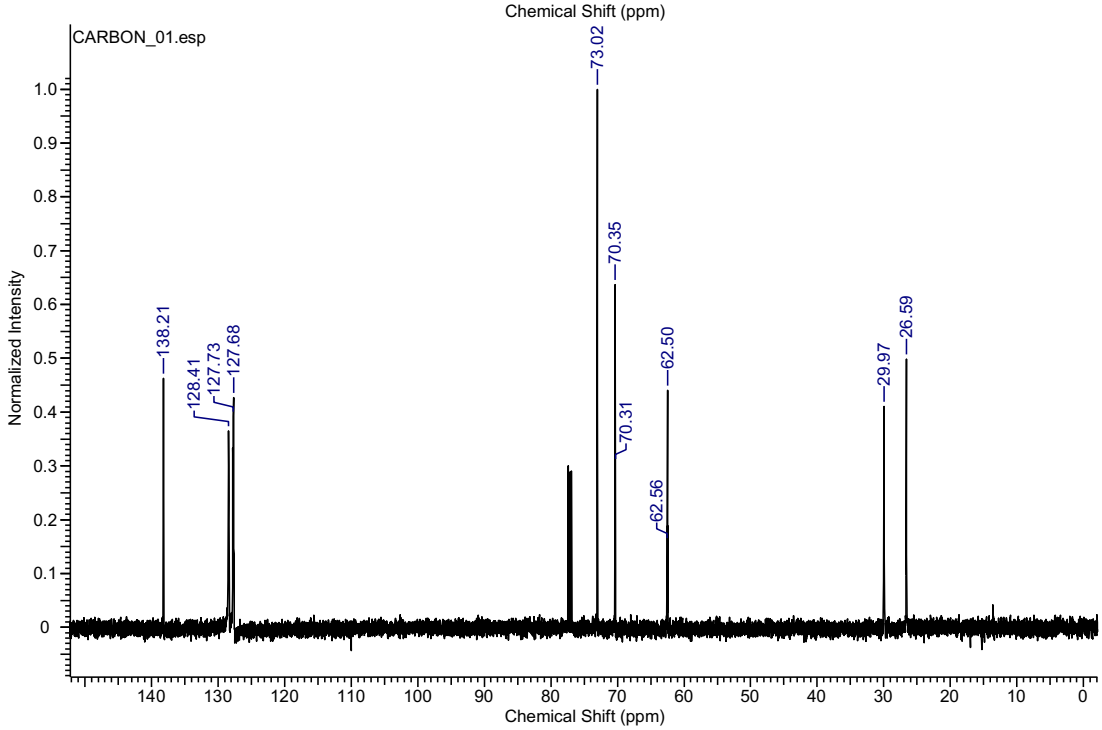

^{1}H and ^{13}C NMR of **14a**

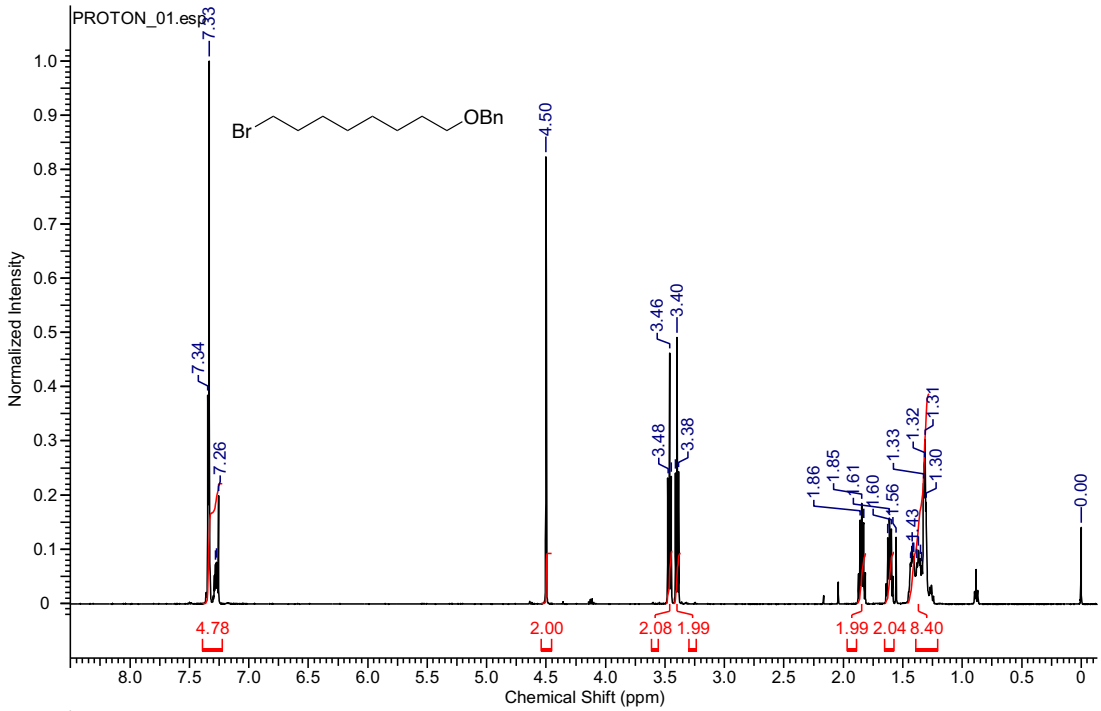

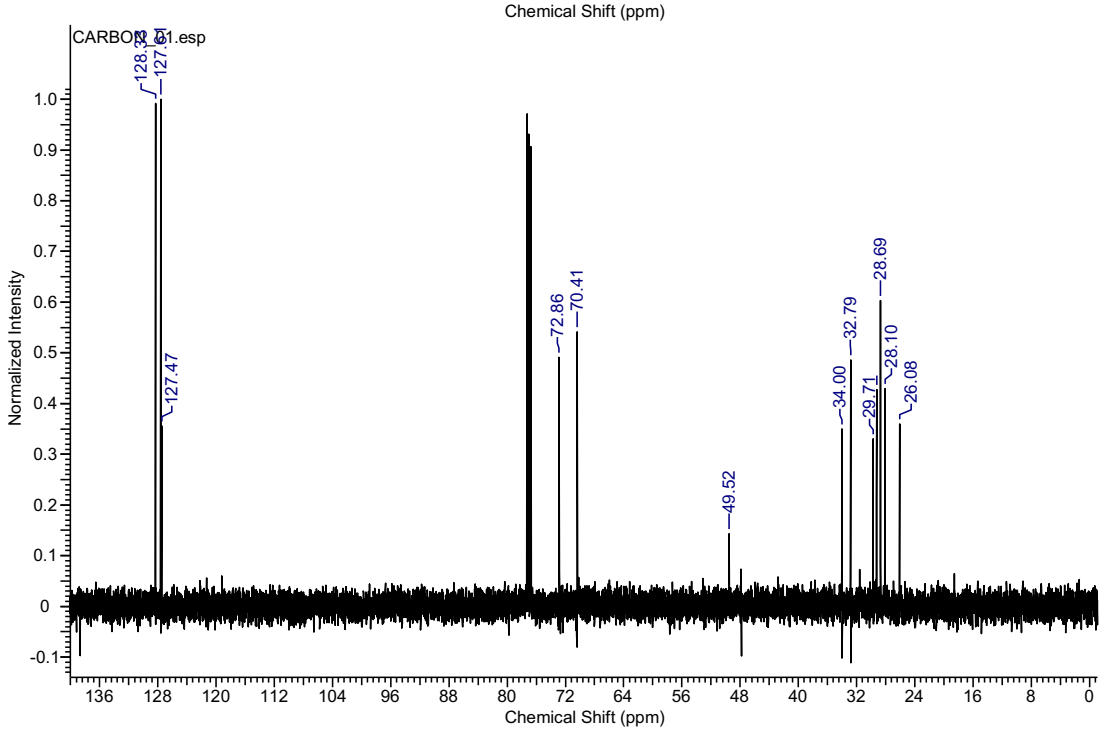

^{1}H and ^{13}C NMR of **14b**

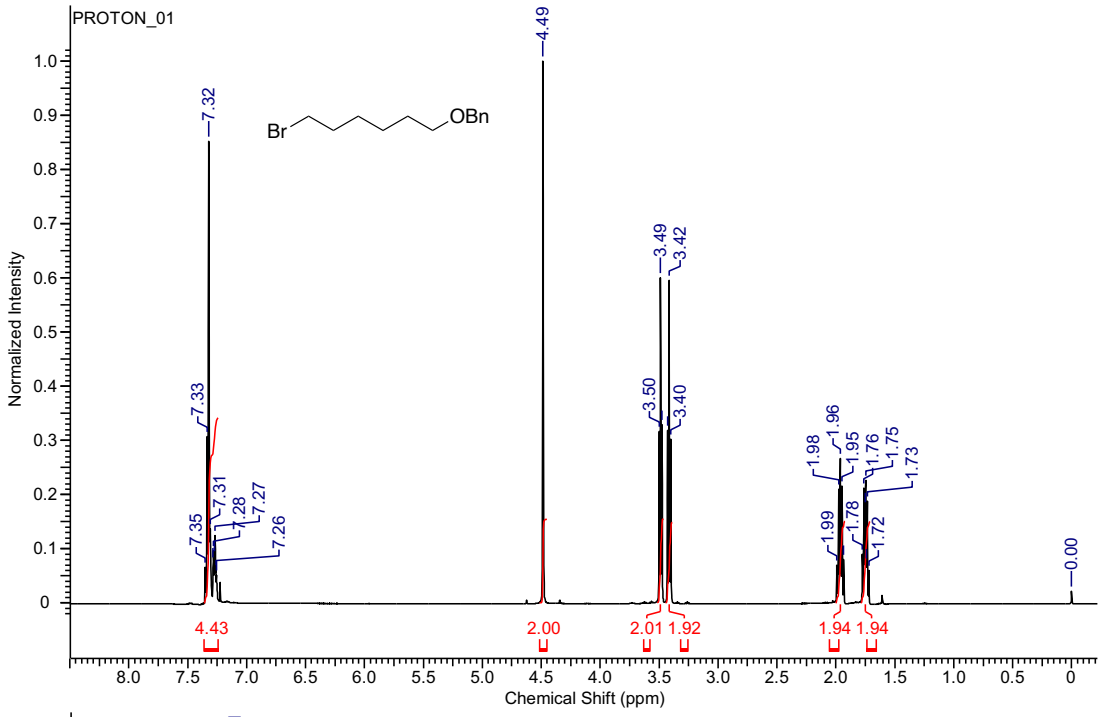

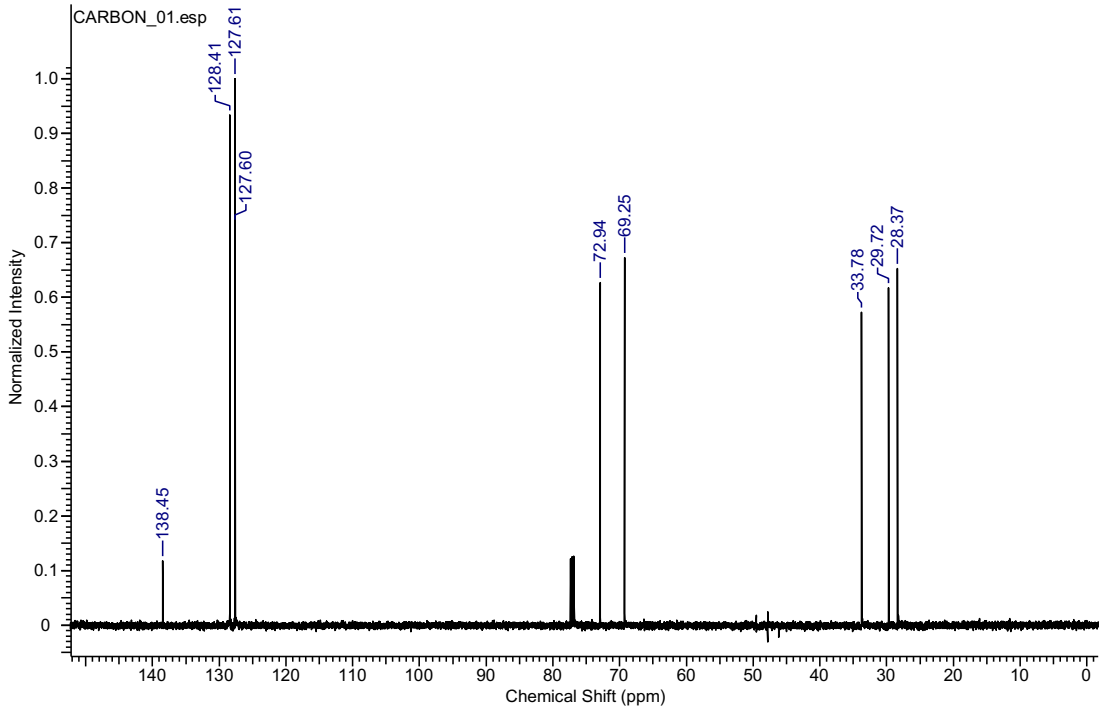

^{1}H and ^{13}C NMR of **15a**

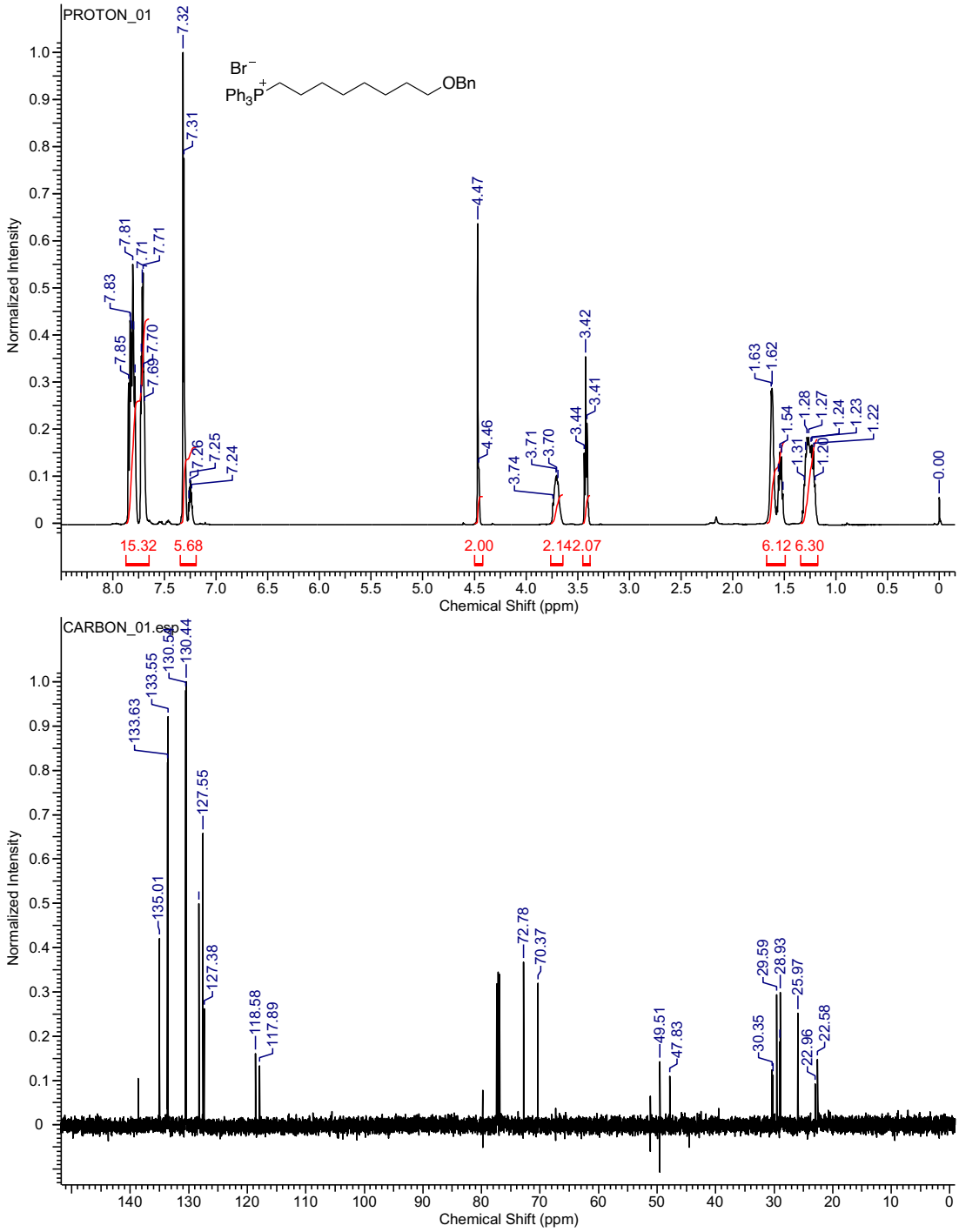

^{1}H and ^{13}C NMR of **15b**

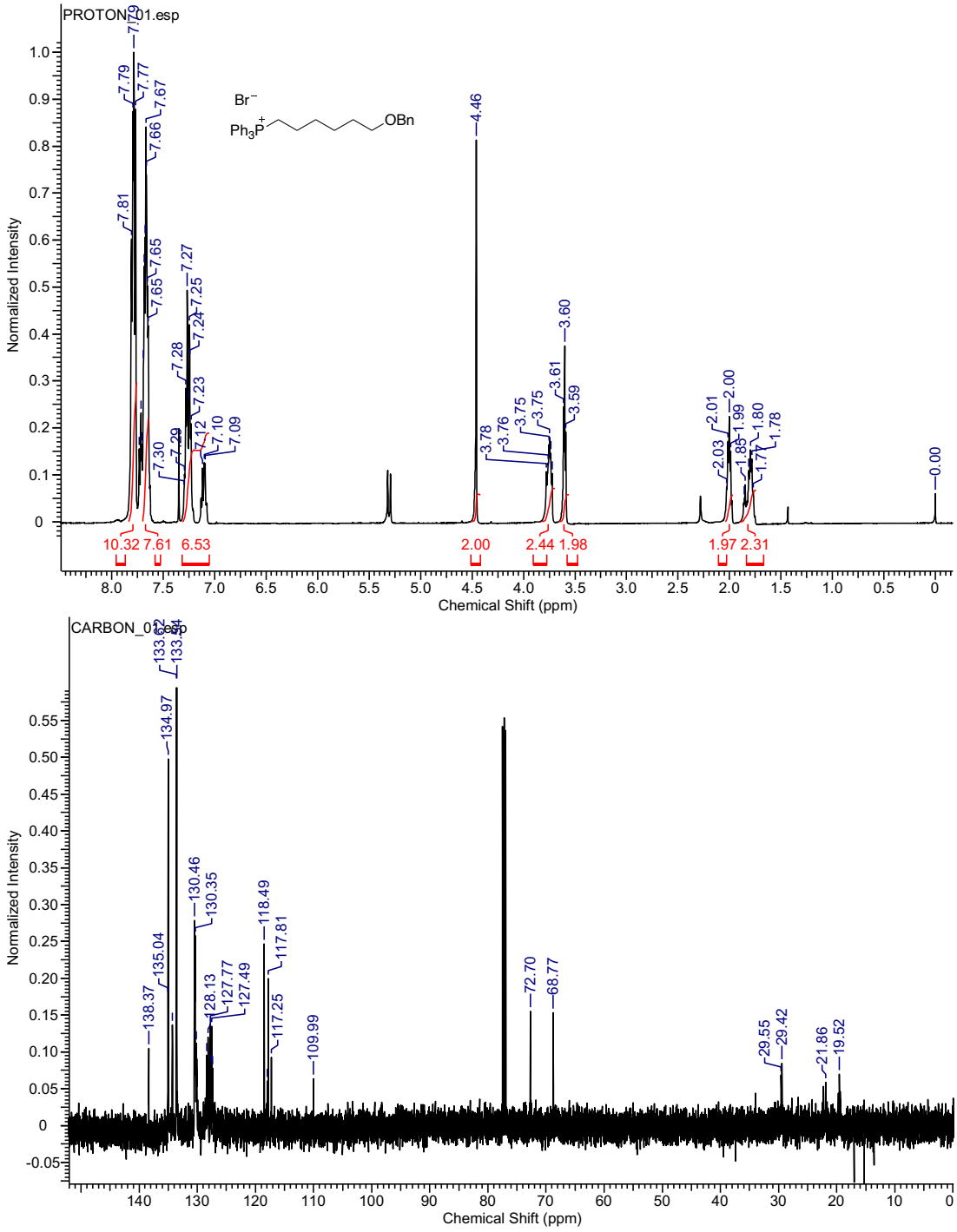

^{1}H and ^{13}C NMR of **16a**

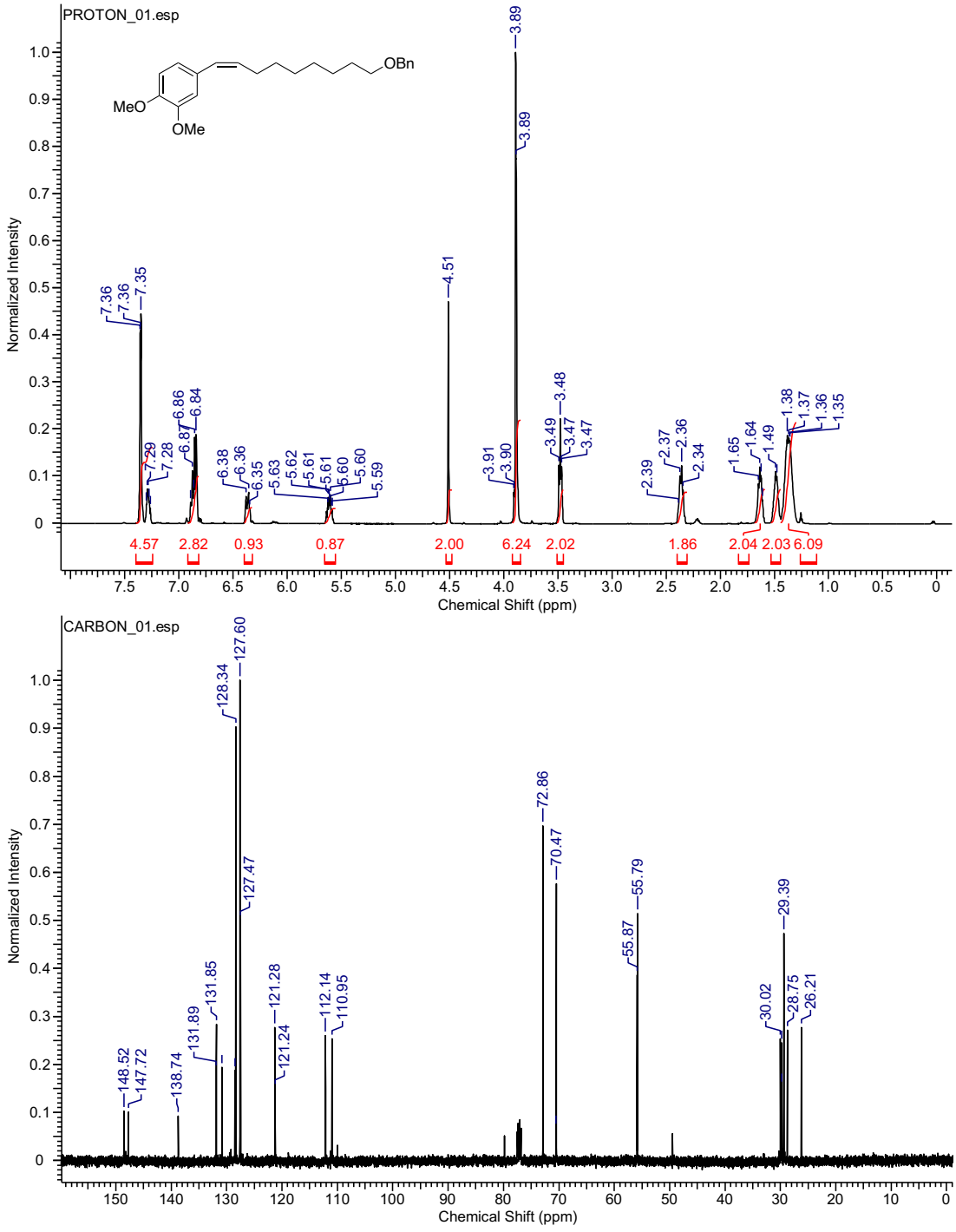

^{1}H and ^{13}C NMR of **16b**

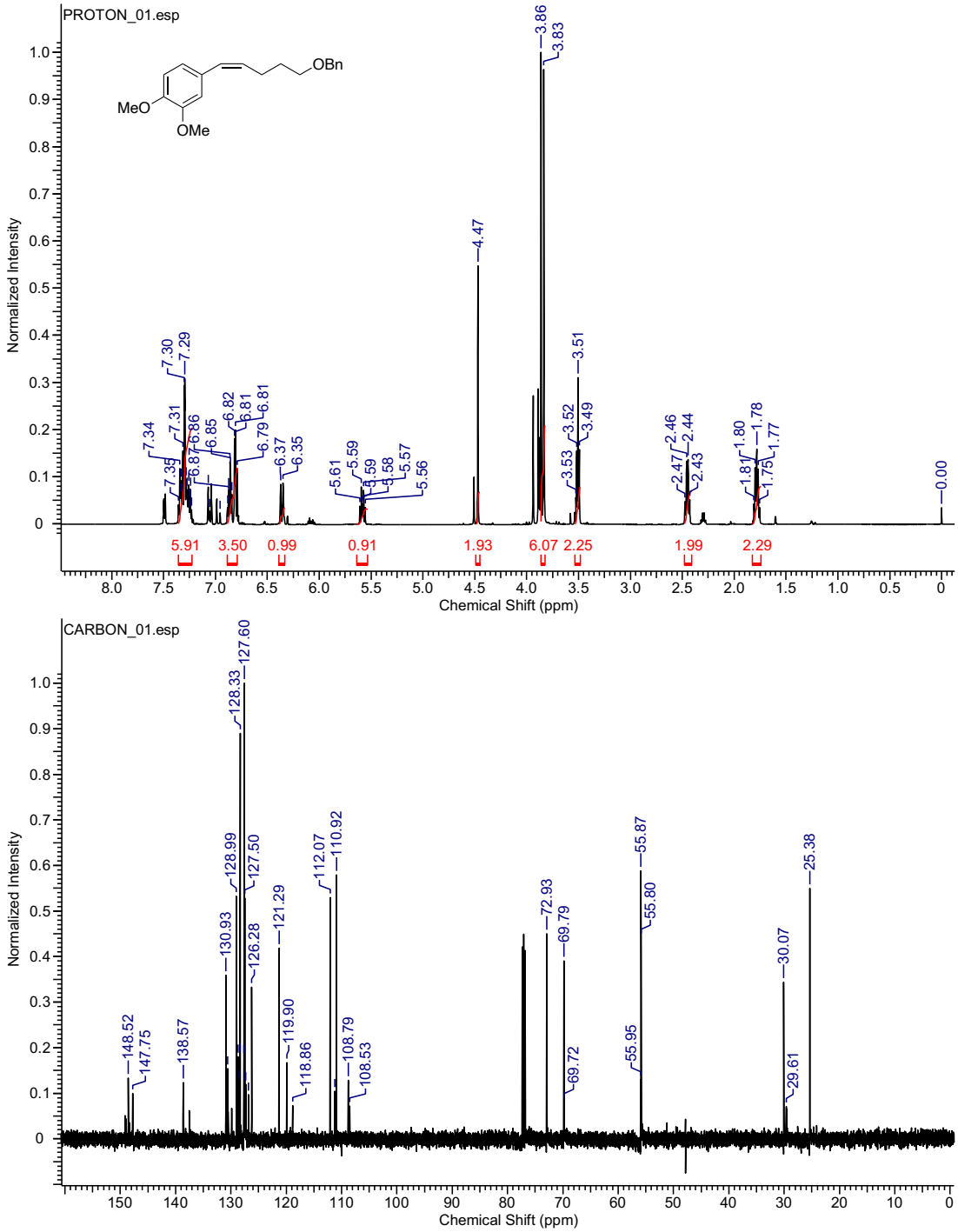

^{1}H and ^{13}C NMR of **17a**

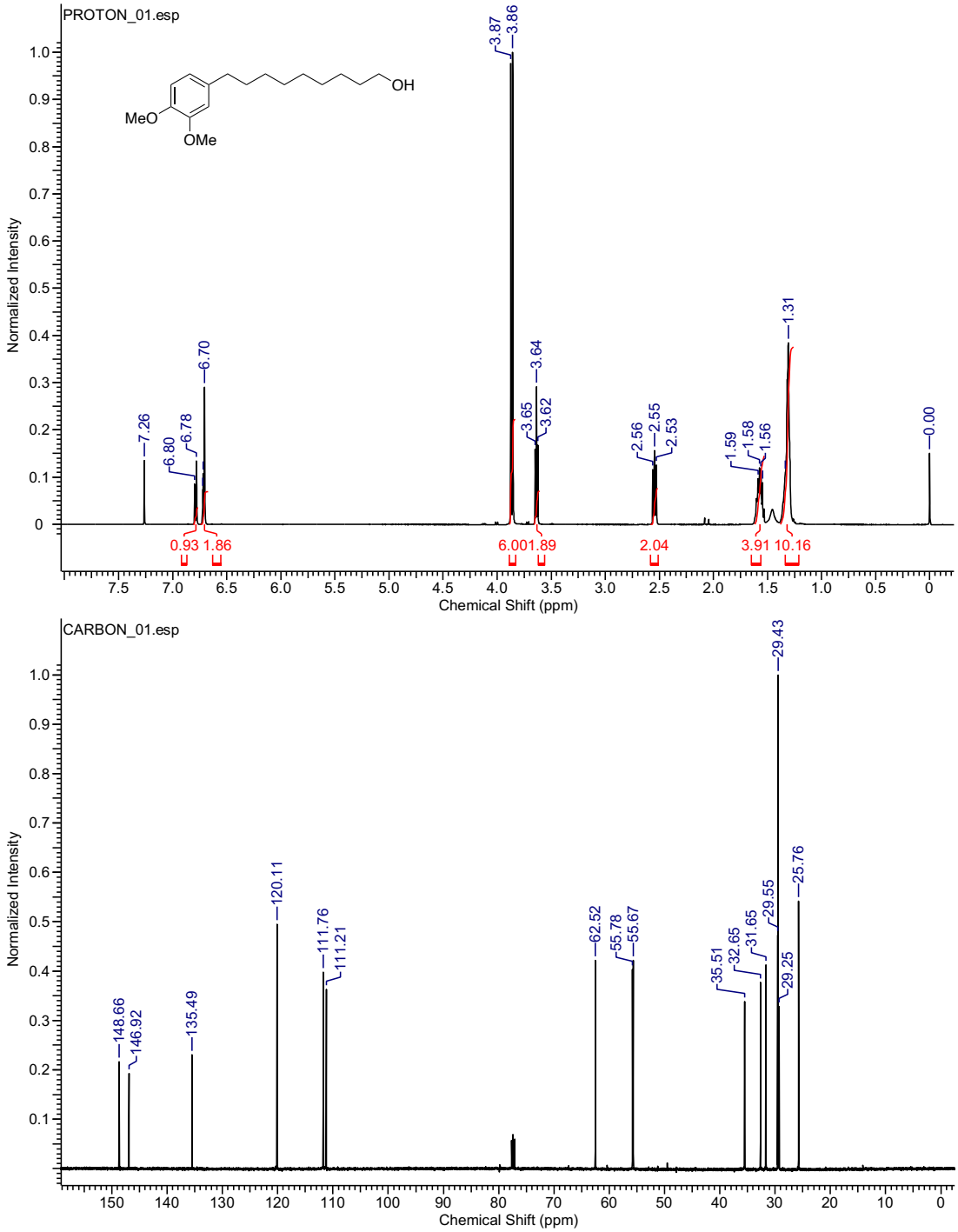

^{1}H and ^{13}C NMR of **17b**

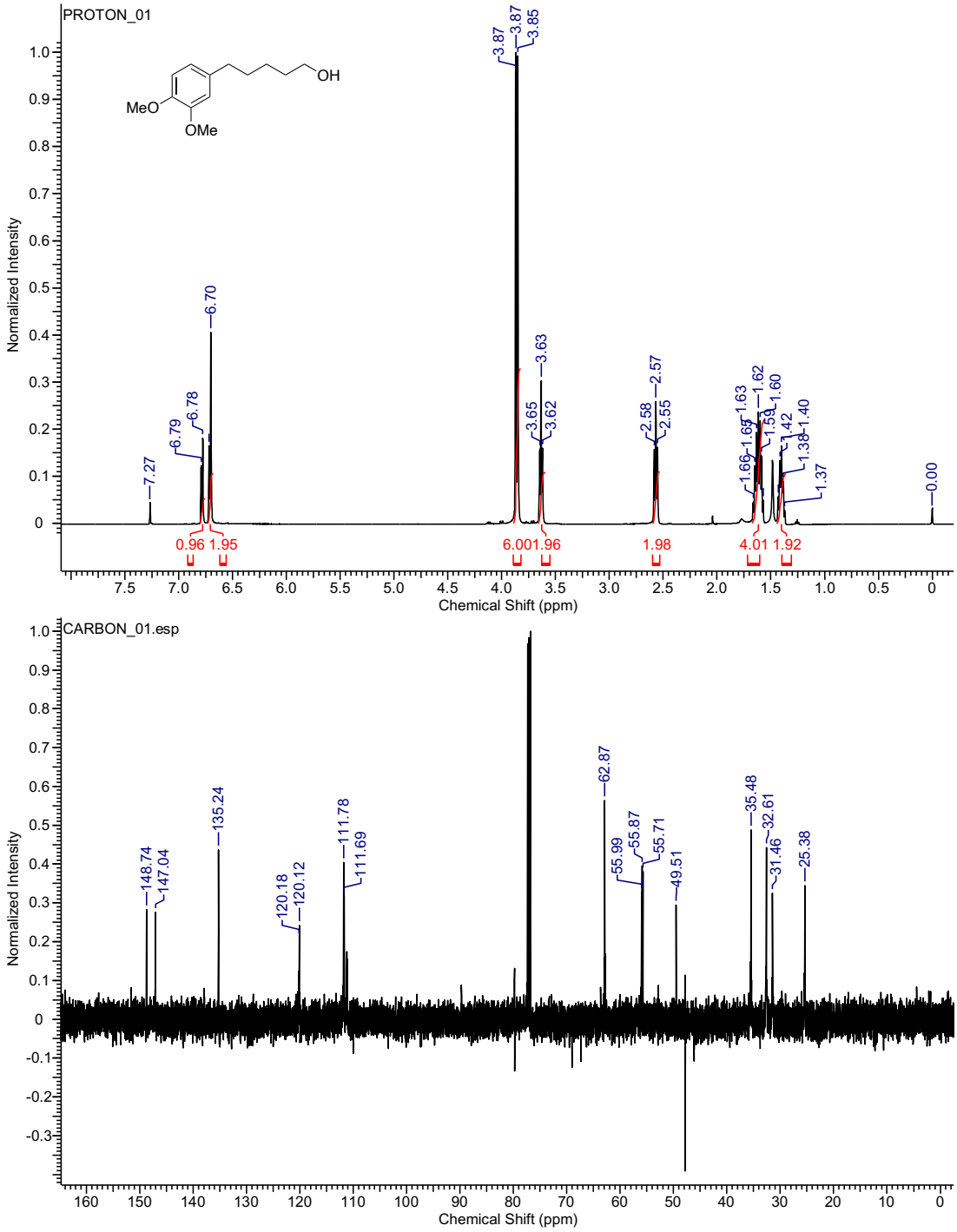

^{1}H and ^{13}C NMR of **18a**

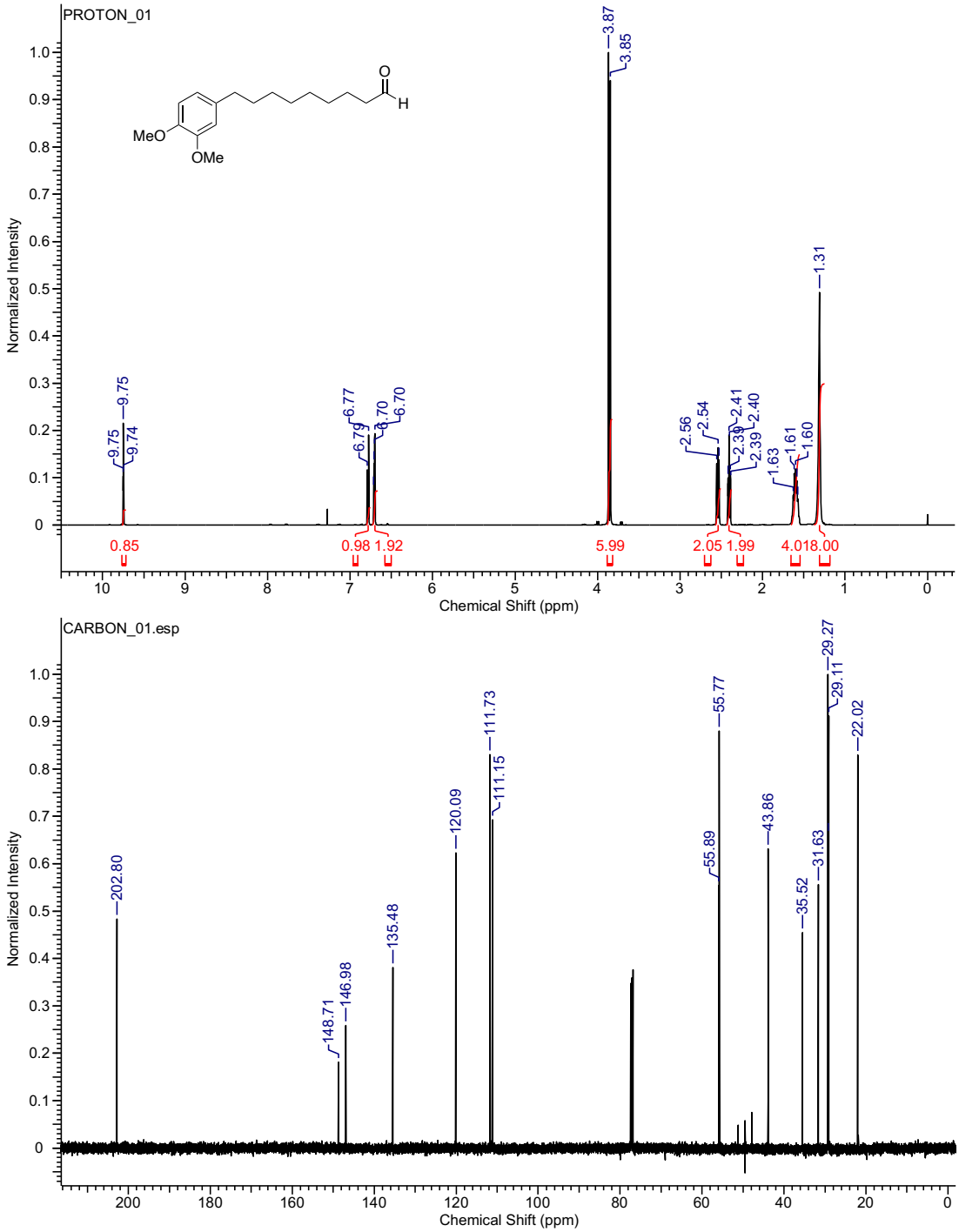

^{1}H and ^{13}C NMR of **18b**

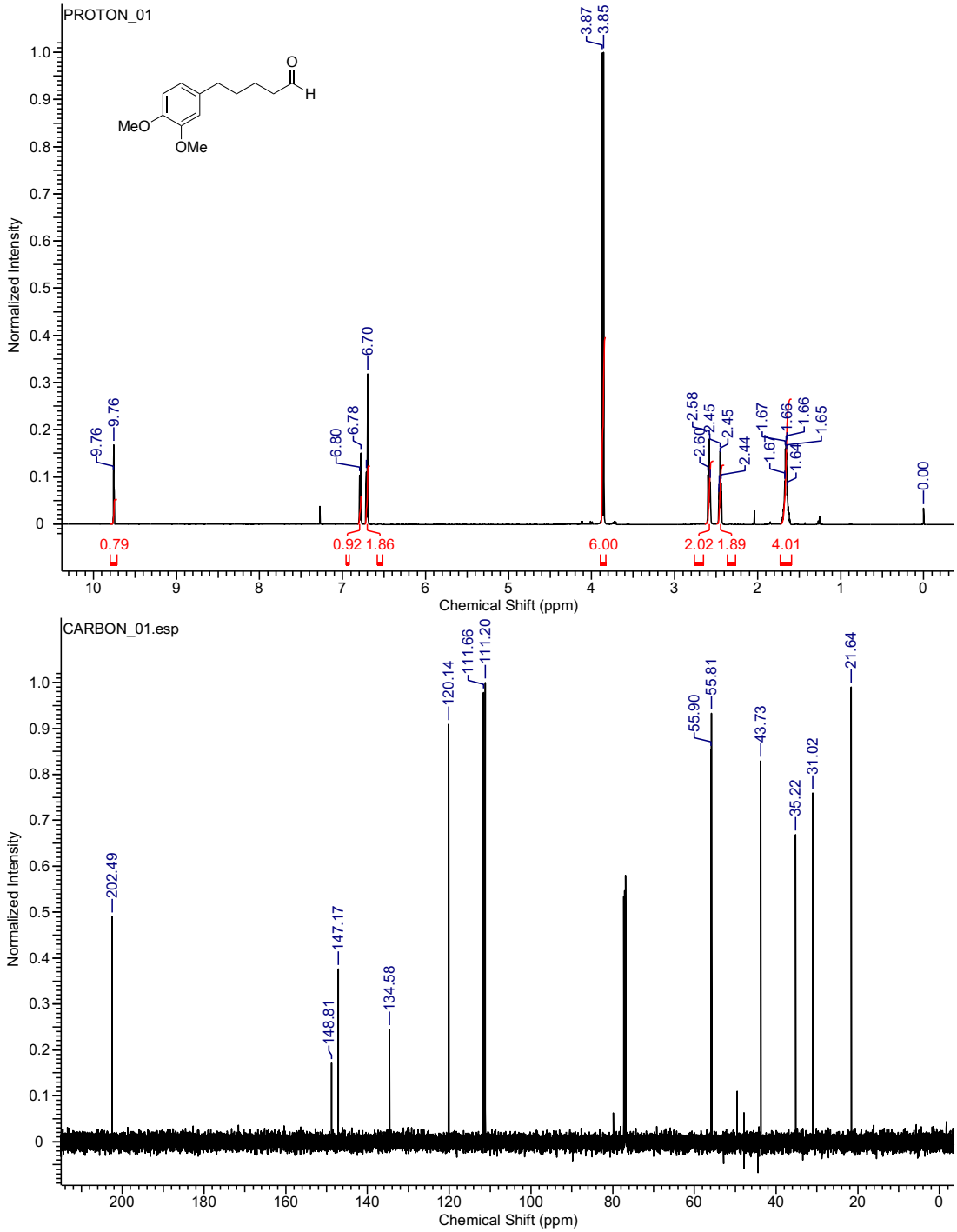

^{1}H and ^{13}C NMR of **19**

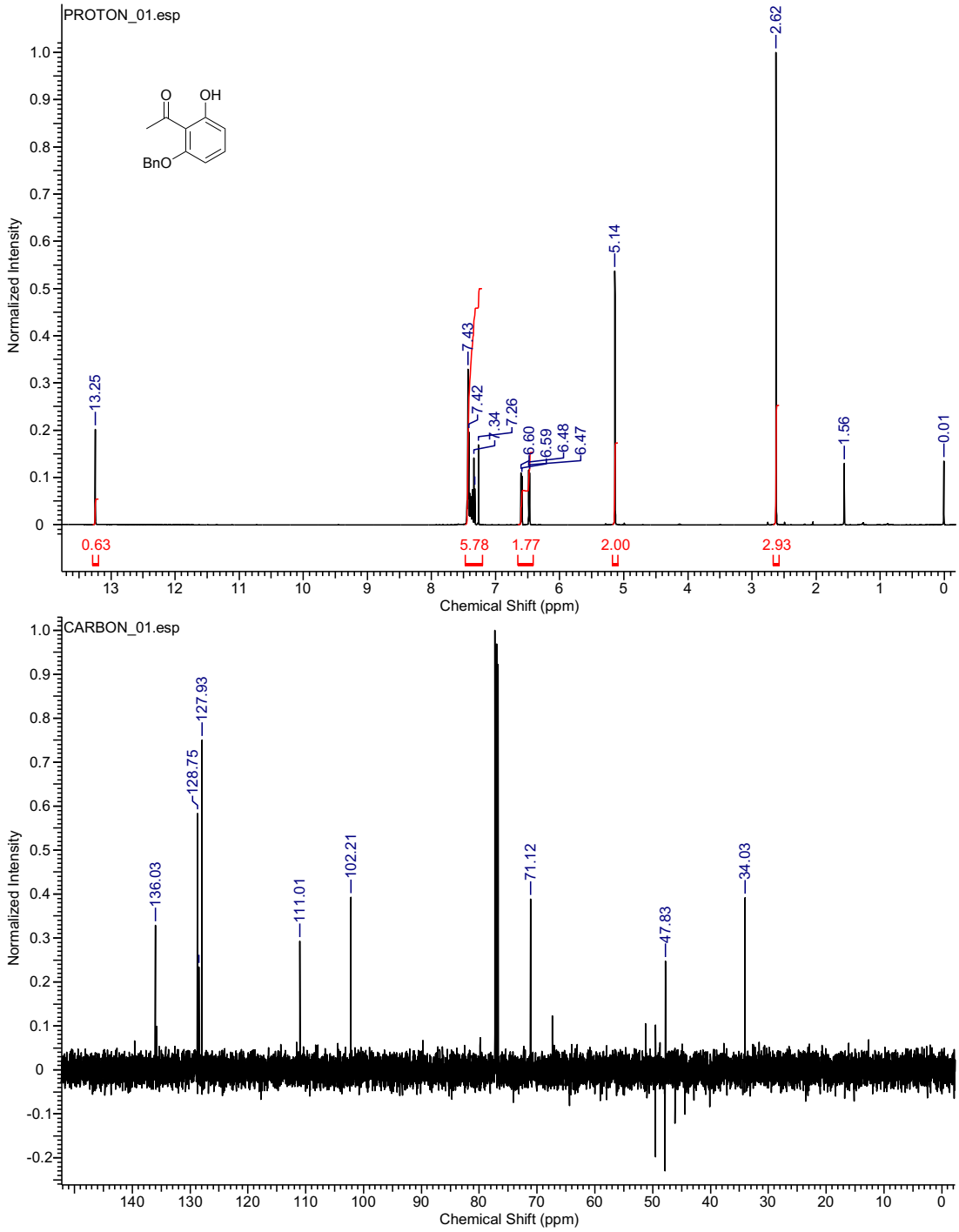

^{1}H and ^{13}C NMR of **20a**

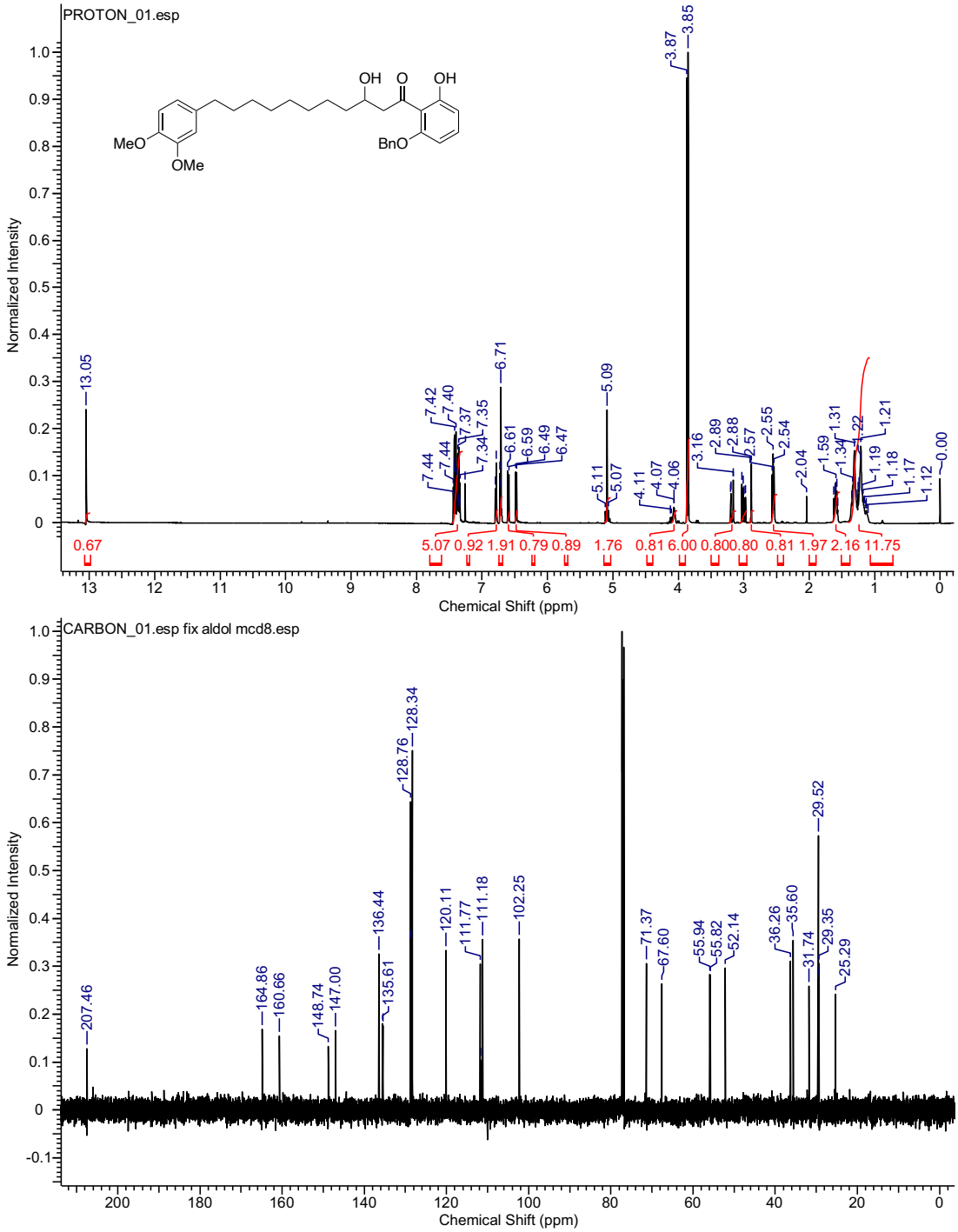

^{1}H and ^{13}C NMR of **20b**

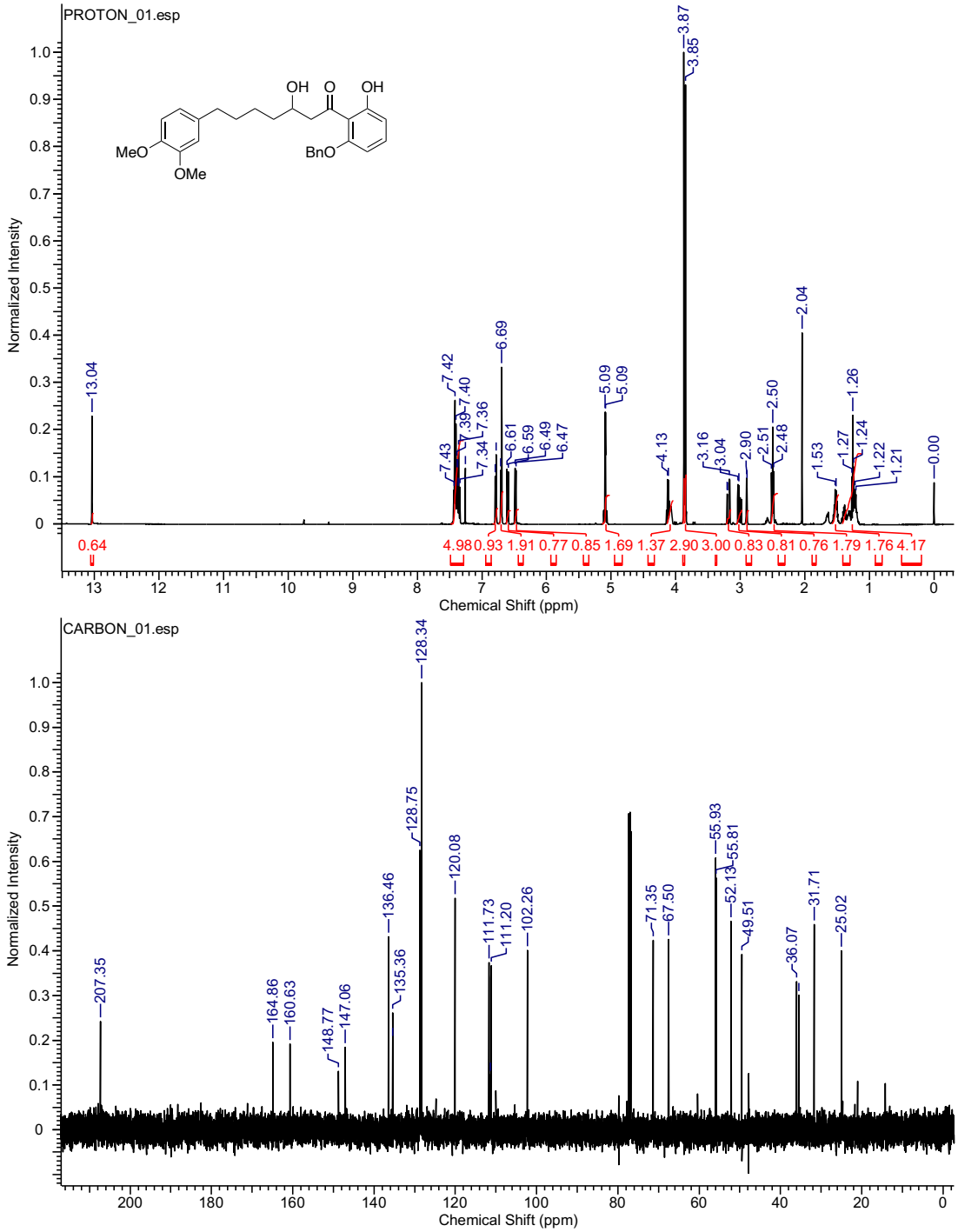

^{1}H and ^{13}C NMR of **21a**

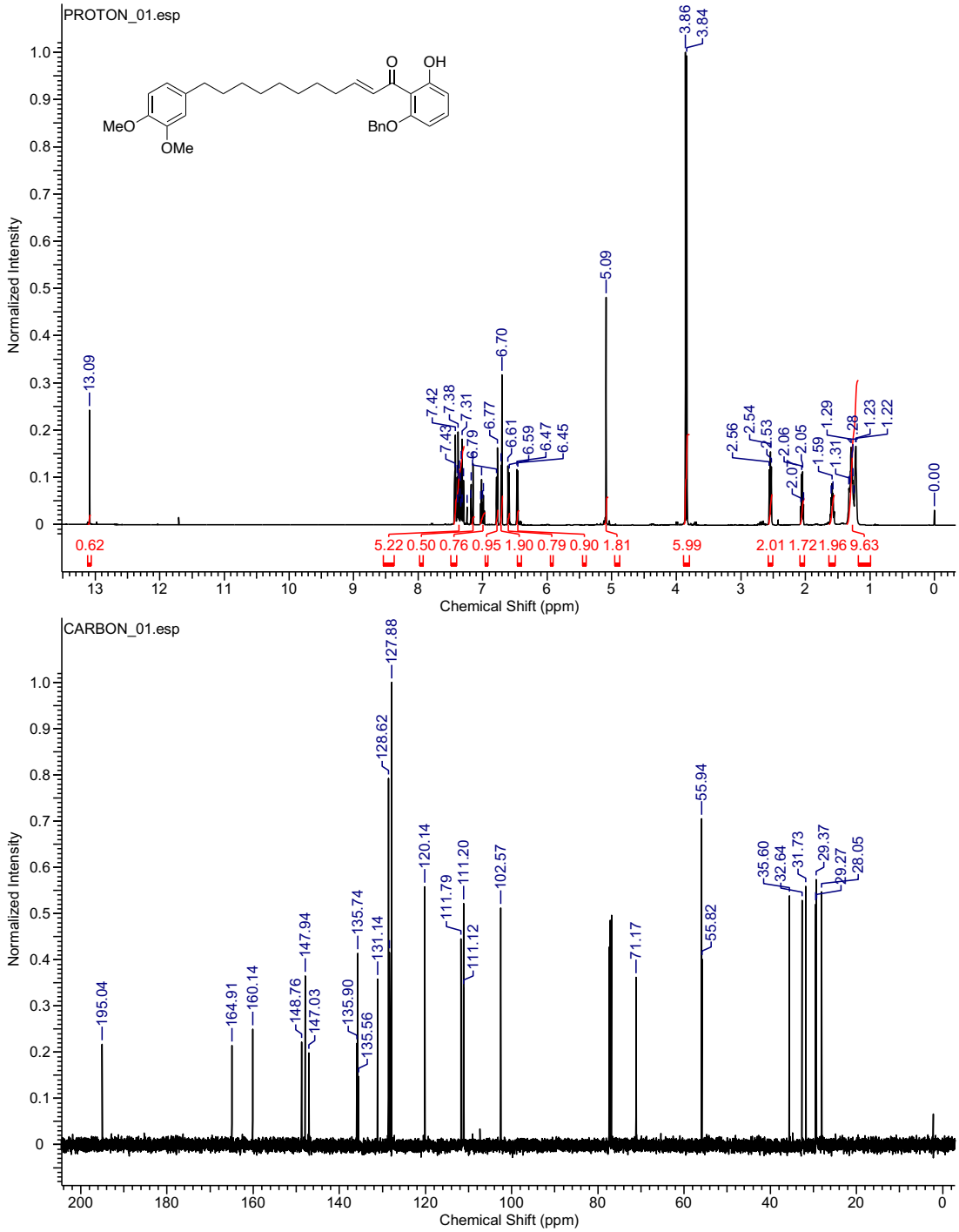

^{1}H and ^{13}C NMR of **21b**

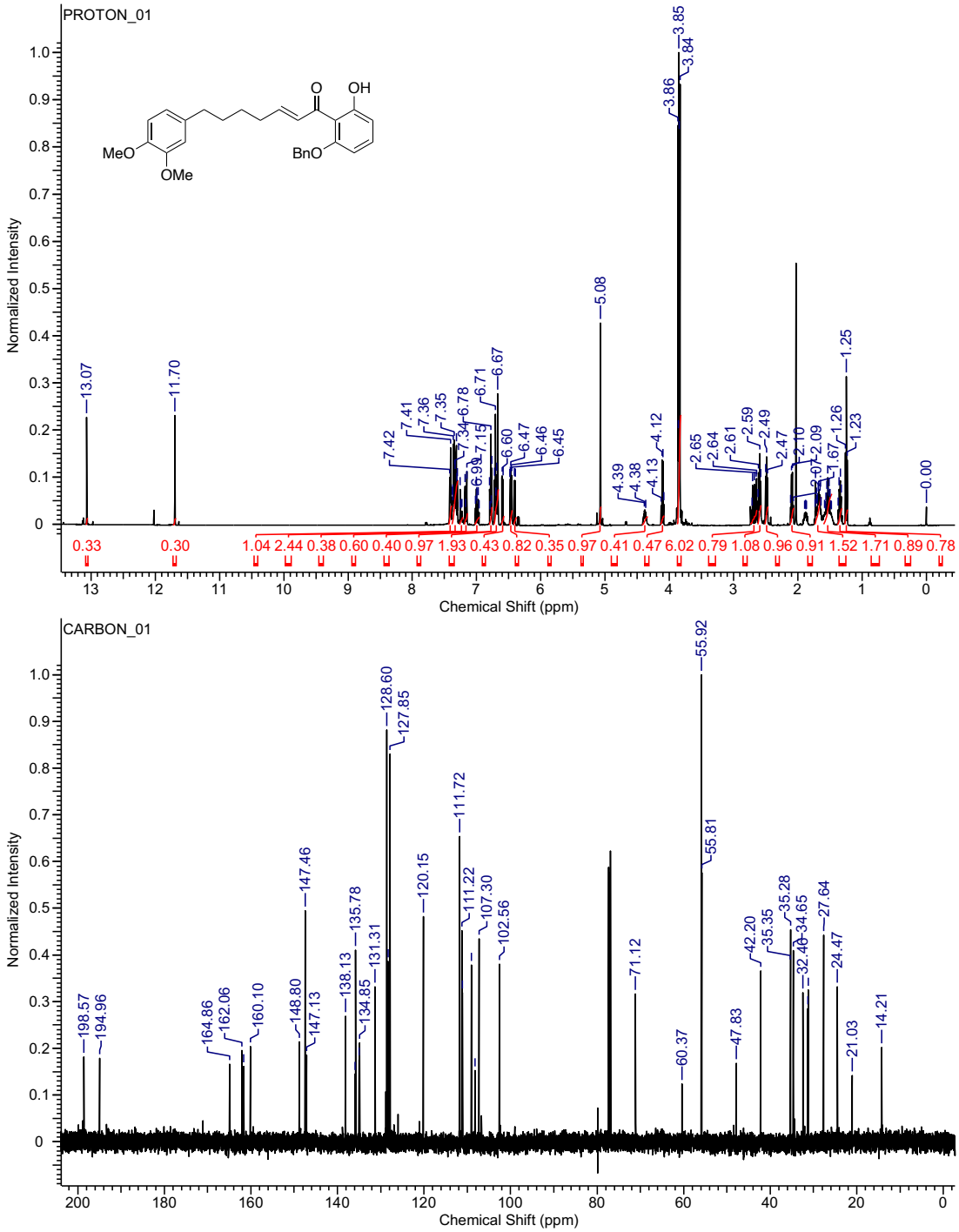

^{1}H and ^{13}C NMR of **22a**

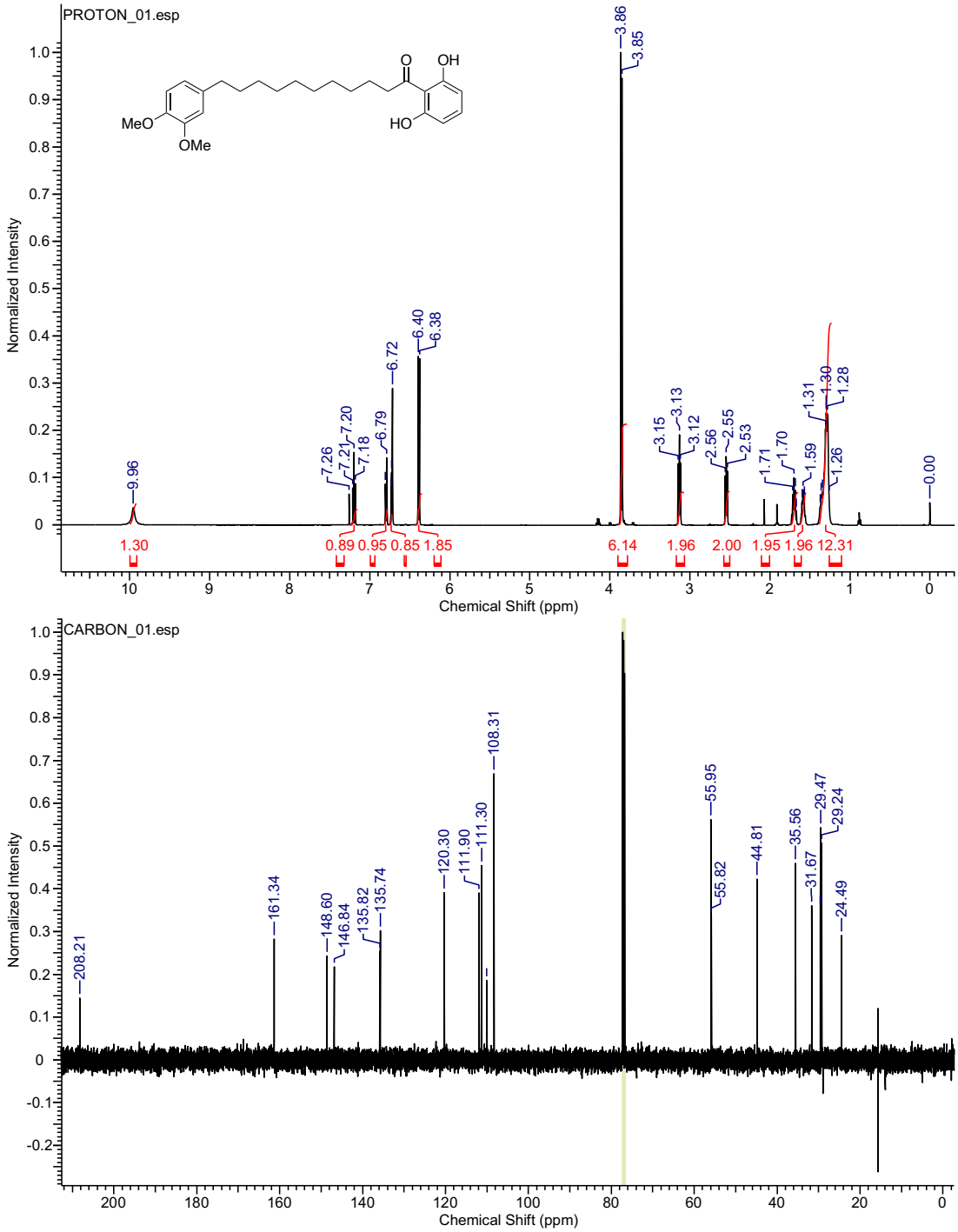

^{1}H and ^{13}C NMR of **22b**

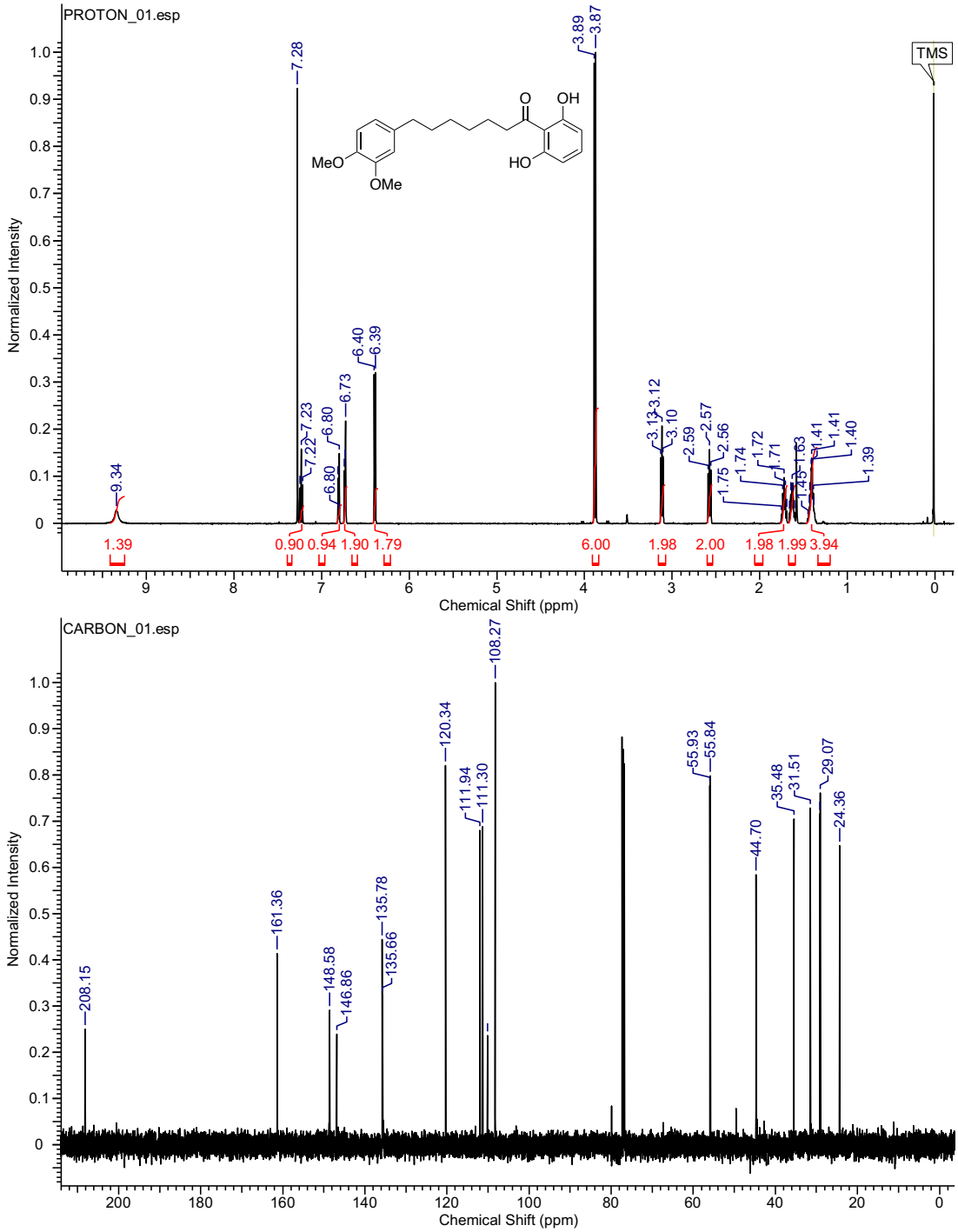

2.6 References

1. Zhu, N.; Zhang, D.; Wang, W.; Li, X.; Yang, B.; Song, J.; Zhao, X.; Huang, B.; Shi, W; Lu, R.; et al. A Novel Coronavirus from Patients with Pneumonia in China, 2019. *N. Engl. J. Med.* **2020**, *382*, 727−733.
2. a) Li, Q.; Guan, X.; Wu, P.; Wang, X.; Zhou, L.; Tong, Y.; Ren, R.; Leung, K. S. M.; Lau, E. H. Y.; Wong, J. Y. et al., Early Transmission Dynamics in Wuhan, China, of Novel Coronavirus-Infected Pneumonia. *N. Engl. J. Med.* **2020**, *382*, 1199−1207.
3. Sohrabi, C.; Iosifidis, C.; Alsafi, Z.; Khan, M.; O'Neill, N.; Kerwan, A.; Al-Jabir, A.; Agha, R. *Int. J. Surg.* **2020**, *76*, 71−76.
4. Shang, J.; Wan, Y.; Luo, C.; Ye, G.; Geng, Q.; Auerbach, A.; Li, F. Cell entry mechanisms of SARS-CoV-2. *Proc. Natl. Acad. Sci. USA.* **2020**, *117*, 11727−11734.
5. Cantuti-Castelvetri, L.; Ojha, R.; Pedro, L.D.; Djannatian, M.; Franz, J.; Kuivanen, S.; van der Meer, F.; Kallio, K.; Kaya, T.; Anastasina, M.; Smura, T.; Levanov, L.; Szirovicza, L.; Tobi, A.; Kallio-Kokko, H.; Österlund, P.; Joensuu, M.; Meunier, F.A.; Butcher, S.J.; Winkler, M.S.; Mollenhauer, B.; Helenius, A.; Gokce, O.; Teesalu, T.; Hepojoki, J.; Vapalahti, O.; Stadelmann, C.; Balistreri, G.; Simons, M. Neuropilin-1 facilitates SARS-CoV-2 cell entry and infectivity. *Science*. **2020**, *370*, 856-860.
6. Daly, J.L.; Simonetti, B.; Klein, K.; Chen, K.E.; Williamson, M.K.; Antón-Plágaro, C.; Shoemark, D.K.; Simón-Gracia, L.; Bauer, M.; Hollandi, R.; Greber, U.F.; Horvath, P.; Sessions, R.B.; Helenius, A.; Hiscox, J.A.; Teesalu, T.; Matthews, D.A.; Davidson, A.D.; Collins, B.M.; Cullen, P.J.; Yamauchi. Y. *Science.* **2020**, *370*, 861-865.
7. Hoffmann, M.; Hofmann-Winkler, H.; Smith, J.C.; Krüger, N.; Arora, P.; Sørensen, L.K.; Søgaard, O.S.; Hasselstrøm, J.B.; Winkler, M.; Hempel, T.; Raich, L.; Olsson, S.; Danov, O.; Jonigk, D.; Yamazoe, T.; Yamatsuta, K.; Mizuno, H.; Ludwig, S.; Noé, F.; Kjolby, M.; Braun, A.; Sheltzer, J.M.; Pöhlmann, S. Camostat mesylate inhibits SARS-CoV-2 activation by TMPRSS2-related proteases and its metabolite GBPA exerts antiviral activity. *EBioMedicine*. **2021**, *65*:103255.

8. Wei, J.; Alfajaro, M.M.; DeWeirdt, P.C.; Hanna, R.E.; Lu-Culligan, W.J.; Cai, W.L.; Strine, M.S.; Zhang, S.M.; Graziano, V.R.; Schmitz, C.O.; Chen, J.S.; Mankowski, M.C.; Filler, R.B.; Ravindra, N.G.; Gasque, V.; de Miguel, F.J.; Patil, A.; Chen, H.; Oguntuyo, K.Y.; Abriola, L.; Surovtseva, Y.V.; Orchard, R.C.; Lee, B.; Lindenbach, B.D.; Politi, K.; van Dijk, D.; Kadoch, C.; Simon, M.D.; Yan, Q.; Doench, J.G.; Wilen, C.B. *Cell*. **2021**, *184*, 76-91.e13.
9. Kadali, R.A.K.; Janagama, R.; Yedlapati, S.H.; Kanike, N.; Gajula, V.; Madathala, R.R.; Poddar, S.; Sukka, N.; Jogu, H.R.; Racherla, S.; Shah, I. Side effects of messenger RNA vaccines and prior history of COVID-19, a cross-sectional study. *Am J Infect Control.* **2022**, *50*, 8-14.
10. Mulangu, S.; Dodd, L. E.; Davey, R. T. Jr.; Tshiani, M. O.; Proschan, M.; Mukadi, D.; Lusakibanza, M. M.; Nzolo, D.; Tshomba, O. A.; Ibanda, A. et al. A Randomized, Controlled Trial of Ebola Virus Disease Therapeutics. *Engl. J. Med.* **2019**, *381*, 2293−2303.
11. Sheahan, T. P.; Sims, A. C.; Graham, R. L.; Menachery, V. D.; Gralinski, L. E.; Leist, S. R.; Baric, R. S.; Case, J. B.; Pyrc, K.; Feng, J. Y. et al. Broad-spectrum antiviral GS-5734 inhibits both epidemic and zoonotic coronaviruses. *Sci. Transl. Med.* **2017**, *9*, eaal3653.
12. Wang, M.; Zhang, L.; Yang, X.; Liu, J.; Xu, M.; Shi, Z.; Hu, Z.; Xiao, G.; Cao, R.; Zhong, Wu. Remdesivir and chloroquine effectively inhibit the recently emerged novel coronavirus (2019-nCoV) in vitro. **2020**, *30*, 269−271.
13. Jin, Z., Du, X., Xu, Y., Deng, Y., Liu, M. *et al.* Structure of M^{pro} from SARS-CoV-2 and discovery of its inhibitors. Nature **2020**, *582*, 289–293.
14. Ul Qamar, M. T., Alqahtani, S. M., Alamri, M. A. & Chen, L. L. Structural basis of SARS-CoV-2 3CLproand anti-COVID-19 drug discovery from medicinal plants. *J. Pharm. Anal.* **2020**, *10*, 313–319.
15. Kanjanasirirat, P., Suksatu, A., Manopwisedjaroen, S., Munyoo, B., Tuchinda, P. *et al.* High-content screening of Thai medicinal plants reveals Boesenbergia rotunda extract and its component Panduratin A as anti-SARS-CoV-2 agents. *Sci. rep.* **2020**, 10:19963.
16. Rubio-Martínez, J.; Jiménez-Alesanco, A.; Ceballos-Laita, L.; Ortega-Alarcón, D.; Vega, S.; Calvo, C.; Benítez, C.; Abian, O.; Velázquez-Campoy, A.;

Thomson, TM.; Granadino-Roldán, JM.; Gómez-Gutiérrez, P.; Pérez, JJ. Discovery of diverse natural products as inhibitors of SARS-CoV-2 Mpro protease through virtual screening. *J. Chem. Inf. Model.* **2021**, *61*, 6094–6106.

17. Borenstein, R., Hanson, A. B., Markosyan, M. R., Gallo, S. E., Narasipura, D. S. *et al.* Ginkgolic acid inhibits fusion of enveloped viruses. *Sci. Rep.* **2020**, 10:4746.
18. Krüger, N.; Kronenberger, T.; Xie, H.; Rocha, C.; Pöhlmann, S.; Su, H.; Xu, Y.; Laufer, SA.; Pillaiyar T. Discovery of polyphenolic natural products as SARS-CoV-2 Mpro inhibitors for COVID-19. *Pharmaceuticals*. **2023**, *16*, 190.
19. Risener, CJ.; Woo, S.; Samarakoon, T.; Caputo, M.; Edwards, E.; Klepzig, K.; Applequist, W.; Zandi, K.; Goh, SL.; Downs-Bowen, JA.; Schinazi, RF.; Quave, CL. Botanical inhibitors of SARS-CoV-2 viral entry: a phylogenetic perspective. *Sci Rep.* **2023**, *13*, 1244.
20. Swamy, M. M. M., Murai, Y., Ohno, Y., Jojima, K., Kihara, A. *et al.* Structure-inspired design of a sphingolipid mimic sphingosine-1-phosphate receptor agonist from a naturally occurring sphingomyelin synthase inhibitor. *Chem. Commun.* **2018**, *54*, 12758–12761
21. Tafesse, G. F.; Sanyal, S.; Ashour, J.; Guimaraes, P. C.; Hermansson, M. *et al.* Intact sphingomyelin biosynthetic pathway is essential for intracellular transport of influenza virus glycoproteins. *Proc. Natl. Acad. Sci. USA.* **2013**, *110*, 6406–6411.
22. Hayashi, Y., Sasaki, YN., Tanikawa, T., Oka, S., Tsuchiya, K., et al. Sphingomyelin Synthase 2, but Not Sphingomyelin Synthase 1, is Involved in HIV-1 Envelope-mediated Membrane Fusion, *J Biol Chem*, **2014**, 289, 30842-30856.
23. Deepak, V. H.; Swamy, M. M.M.; Murai, Y.; Suga, Y.; Anetai, M. *et al.* Daurichromenic acid from the Chinese traditional medicinal plant Rhododendron dauricum inhibits sphingomyelin synthase and Aβ aggregation. *Molecules* **2020**, *25*, 4077.
24. Othman, M. A.; Yuyama, K.; Murai, Y.; Igarashi, Y.; Mikami, D. *et al.* Malabaricone C as natural sphingomyelin synthase inhibitor against diet-induced obesity and its lipid metabolism in mice. *ACS Med. Chem. Lett.* **2019**, *10*, 1154–1158.

25. Sasaki, M.; Uemura, K.; Sato, A.; Toba, S.; Sanaki, T. et al. SARS-CoV-2 variants with mutations at the S1/S2 cleavage site are generated in vitro during propagation in TMPRSS2-deficient cells. *PLoS Pathog.* **2021**, e1009233.
26. Hosoi, S.; Kiuchi, F.; Nakamura, N.; Imasho, M.; Ali, A. M. *et al.* Synthesis and nematocidal activity of diarylnonanoids related to malabaricones. *Chem. Pharm. Bull.* **1999**, *47*, 37–43.
27. Gao, J.; Tian, Z. & Yang, X. Breakthrough: chloroquine phosphate has shown apparent efficacy in treatment of COVID-19 associated pneumonia in clinical studies. *Biosci. Trends.* **2020**, *14*, 72–73.
28. Yao, X.; Ye, F.; Zhang, M.; Cui, C.; Huang, B. *et al.* In vitro antiviral activity and projection of optimized dosing design of hydroxychloroquine for the treatment of severe acute respiratory syndrome coronavirus 2 (SARS-CoV-2). *Clin. Infect. Dis.* **2020**, *71*, 732–739.
29. Colson, P.; Rolain, J. M.; Lagier, J. C.; Brouqui, P.; Raoult, D. Chloroquine and hydroxychloroquine as available weapons to fight COVID-19. *Int. J. Antimicrob. Agents.* **2020**, *55*, 105932.

Chapter 3

The Discovery of the Mechanism of Malabaricone C as an Antiviral for SARS-CoV-2

3.1. Abstract

The life cycle of SARS-CoV-2 can be generally divided into five stages: cell entry, viral genome translation, subgenomic transcription, genome replication, and the formation of progeny virions. Cell entry is a critical initial step in the viral life cycle and represents an ideal target for antiviral interventions. Understanding how a small molecule inhibits SARS-CoV-2 infection will facilitate the development of effective inhibitors for the virus in the future. This study aims to explore the potential mechanisms by which malabaricone C acts against SARS-CoV-2. Although the specific molecular and cellular mechanisms underlying the antiviral activity of malabaricone C have not yet been fully elucidated, we present evidence for a partial mechanism of its anti-SARS-CoV-2 activity, which involves interference with lipid raft formation on the plasma membrane of Vero E6 cells.

3.2. Introduction

SARS-CoV-2 is a single-stranded, positive-sense RNA virus that belongs to lineage B of the genus *Beta-coronavirus* in the *Coronaviridae* family[1]. The recently sequenced genome of SARS-CoV-2 is approximately 29.9 kb in size, sharing about 78% sequence homology with SARS-CoV[1,2]. The virus enters host cells by directly fusing its viral envelope with the host cell membrane or through membrane fusion within an endosome after endocytosis. Viral entry begins when the receptor-binding domain (RBD) of the spike (S) protein attaches to the human host cell receptors on the cell surface[3,4,5]. One primary receptor for SARS-CoV-2 is angiotensin-converting enzyme 2 (ACE2), which is widely expressed in the lungs, intestine, liver, heart, vascular endothelium, testis, and kidney cells[6].

Recently, additional host receptors and co-receptors that facilitate the entry of SARS-CoV-2 into respiratory system cells have been identified. Following the RBD-receptor interaction, the S protein undergoes proteolytic cleavage, catalyzed by various host proteases such as furin, TMPRSS2, and cathepsin B. This proteolytic processing activates the S protein, allowing for viral-host membrane fusion and the subsequent release of viral RNA into the host cytoplasm. Once in the cytoplasm, the viral RNA employs the host's machinery to replicate its genetic material and assemble new viral particles[7,8].

The entry of pathogenic viruses into susceptible cells is a critical first step in the infection process, making it an important target for intervention. Like other well-known viruses, such as HIV-1 and Ebola, the viral entry of coronaviruses involves a complex multi-step process with numerous interactions and points of vulnerability that could be targeted for therapeutic purposes[9].

In the case of SARS-CoV-2, the binding of the S protein to the cellular ACE2 receptor marks the initial encounter in both the endosomal and non-endosomal pathways during the viral replication cycle. This interaction presents opportunities for preventive interventions[10]. The RBD of the SARS-CoV-2 spike protein binds to the ACE2 receptor with high affinity (Kd = 14.7 nM)[11], as determined by surface plasmon resonance (SPR) interaction analysis. Targeting the RBD-ACE2 interface could disrupt the efficiency of viral infection[9].

Endosomal cysteine proteases, such as cathepsin L, or cell membrane-associated serine proteases, such as TMPRSS2, facilitate the entry of the SARS-CoV virus into host cells. This protease cleaves the viral S protein[7], exposing fusion-competent motifs known as fusion peptides. Importantly, for SARS-CoV, effective inhibition of virus replication requires interference with both proteases[7]. Matsuyama et al. identified Camostat, a commercially available serine protease inhibitor, which can efficiently prevent SARS-CoV infections at a concentration of 10 μM by inhibiting TMPRSS2 activity[12].

Blocking the priming or proteolytic cleavage of the viral S protein is also a viable target for early drug interventions[7]. Recent studies focusing on the interactions between the host cell membrane and the virus have provided new insights into the role of cellular lipids in viral entry[13,14]. Cholesterol-binding agents, such as statins and methyl-β-cyclodextrin (MβCD), can impact cholesterol levels and disrupt lipid rafts. This disruption impairs the adhesion and binding of coronaviruses. Additionally, these compounds may block crucial downstream molecules involved in viral infectivity, reducing pro-inflammatory markers like tumor necrosis factor-alpha (TNF-α) and interleukin-6 (IL-6). They may also influence the autophagic process essential for both viral replication and clearance[15].

The main aim of this study is to explore the mechanism of action of malabaricone C inhibiting SARS-CoV-2 infection. The mechanisms studied in this research include

targeting the binding of the viral spike RBD to ACE2, inhibiting TMPRSS2, and interfering with lipid raft formation in the cellular membrane. These pathways are critical points in the viral life cycle, and modifying them could provide valuable insights into innovative therapeutic strategies against SARS-CoV-2. By exploring how malabaricone C interacts at the molecular level, this study seeks to fill significant gaps in our knowledge of natural compounds as SARS-CoV-2 inhibitors and contribute to the development of novel antiviral treatments.

3.3. Results and Discussion

ACE2-Spike RBD Interaction Inhibition Activity

SARS-CoV-2 uses the spike protein, a trimeric glycoprotein located on its surface, to enter host cells. The viral infection begins when the RBD of the S1 subunit of the spike protein interacts with the host receptor ACE2, followed by the cleavage of the spike protein at the S2′ site by host proteases, such as TMPRSS2[7]. This cleavage step primes the fusion between the virus and the host cell membrane via the S2 subunit of the spike protein. Consequently, therapeutics aimed at disrupting interactions or functions of proteins, such as the spike and ACE2, could be promising for treating COVID-19. A strategy that targets the ACE2 receptor, instead of the RBD, to inhibit their interaction would help bypass issues related to spike protein mutations[16].

Several small molecules have been reported to inhibit the SARS-CoV-2 Spike–ACE2 protein-protein interaction, including methylene blue[17], 9-methoxycanthin-6-one[18], and Kobophenol A, which is isolated from Caragana chamlagu[19]. Additionally, active components from traditional Chinese medicine, such as Oleanolic acid, Tryptanthrin, Chrysophanol, and Rhein, have been identified through molecular docking as having inhibitory activity against the spike protein and ACE2 interaction[20]. Malabaricone C is another small molecule suspected of functioning similarly by inhibiting the interaction between ACE2 and Spike RBD.

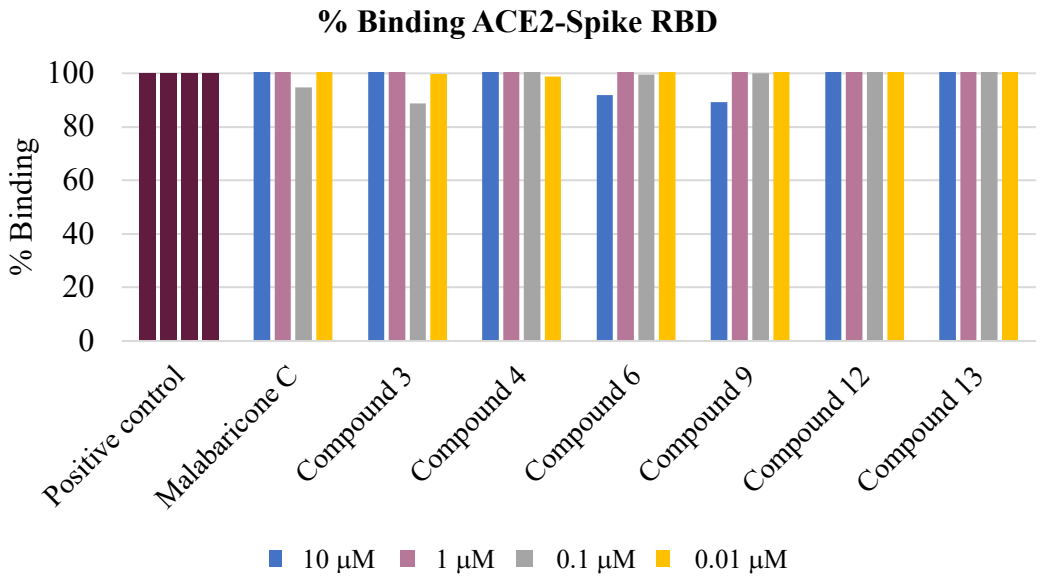

Figure 1. Binding assay result to evaluate ACE2-Spike RBD interaction in the presence of malabaricone C derivatives

To determine whether malabaricone C can inhibit the Spike RBD–ACE2 interaction, we conducted a Spike RBD–ACE2 binding assay using a commercially available kit. In this assay, we measured the total amount of human ACE2-bound RBD protein in the presence of different derivatives of malabaricone C. The results, shown in Figure 1, indicate that the percentage binding between ACE2 and Spike RBD is 100% across almost all compounds tested at various concentrations. This suggests that even in the presence of malabaricone C, the binding between ACE2 and Spike RBD remains unaffected. Therefore, our findings imply that the mechanism of action for malabaricone C in preventing SARS-CoV-2 infection does not involve the inhibition of Spike RBD–ACE2 interactions.

TMPRSS2 Inhibition Activity

TMPRSS2 is recognized as a crucial factor for viral entry and the pathogenesis of SARS-CoV-2[21]. The Spike protein of the virus requires proteolytic processing, or priming, by TMPRSS2 to facilitate entry into lung cells. Therefore, small-molecule inhibitors targeting TMPRSS2 hold significant promise as new therapeutics for COVID-19 and other coronavirus-related diseases[7,22].

Camostat, a serine protease inhibitor, has shown potential against COVID-19 by inhibiting TMPRSS2, which is necessary for viral entry[23]. In this study, camostat was used as a positive control in tests measuring TMPRSS2 inhibition activity. The TMPRSS2 inhibition activity of malabaricone C derivatives was assessed using a TMPRSS2 fluorogenic assay kit from BPS Bioscience. As indicated in Table 1, compounds 3, 6, and 9 exhibited no TMPRSS2 inhibitory activity. However, compounds 1, 4, 12, and 13 demonstrated TMPRSS2 inhibition on a micromolar scale. This finding does not align well with the observed antiviral activity against SARS-CoV-2. The results suggest that the mechanism of action of malabaricone C in inhibiting SARS-CoV-2 viral infection does not occur through TMPRSS2 inhibition.

TMPRSS2 Inhibition Activity		MTT Assay (WK-521)
Compound	IC_{50} (μM)	EC_{50} (μM) WK-521 virus
1	14.1	1.5
3	n.d	1.4
4	3.6	1.5
6	n.d	1.0
9	n.d	n.d
12	1.58	2.9
13	1.0	6.4
Camostat	1.59 nM	

Table 1. The TMPRSS2 inhibitory activities of malabaricone C derivatives, camostat mesylate acts as a positive control

Visualization of the Distribution of Sphingomyelin on the Plasma Membrane

Cellular sphingolipids play crucial roles in the replication and transmission of viruses in humans. Viruses utilize them for processes such as cell entry, membrane fusion, genome replication, assembly, budding, and propagation[24]. These sphingolipids are tightly regulated by sphingolipid metabolic enzymes, which help maintain cellular sphingolipid homeostasis[25]. Targeting and manipulating these

enzymes, including sphingomyelin synthase (SMS) enzymes in host cells, presents a promising strategy against viral infections[26].

Recent studies have reported that SMS1 is a susceptibility factor for Rubella Virus[27,28] and Japanese Encephalitis[29] infection. Another isomorph, SMS2, has also been reported to be involved in regulating HIV-1 Envelope-mediated membrane fusion through actin rearrangement[30]. Since these viruses are enveloped, similar to SARS-CoV-2, evaluating the roles of SMS1 and SMS2 in SARS-CoV-2 infection is particularly interesting.

Compound	IC_{50} (μM)		EC_{50} (μM)
	SMS1	SMS2	WK-521 virus
1	2.5	1.5	1.5
2	8	4	5.4
3	3	1.5	1.4
4	3	1	1.5
5	>100	>100	14.3
6	30	>100	1.0
7	15	9	6.0
8	4	3	1.5
9	>100	>100	n.d.
10	4	30	21.6
(+) Control (C2-60)	5	0.09	

Table 1. Malabaricone C derivatives inhibition activites towards SMS1 and SMS2 enzymes

Additionally, SMS1 and SMS2 are suspected to be the underlying mechanisms by which malabaricone C may prevent SARS-CoV-2 infection. Therefore, we examined the inhibitory activity of malabaricone C on SMS1 and SMS2 enzymes. As shown in Table 1, malabaricone C demonstrated significant inhibitory activity against both SMS1 and SMS2 enzymes. This result aligns with the EC_{50} values of nearly all tested compounds against the wild-type SARS-CoV-2 (WK-521). However, the SMS inhibition activity for compound 6 does not correspond with its antiviral activity

against the WK-521 virus line. This finding suggests that there may be another target for malabaricone C in inhibiting SARS-CoV-2 infection.

The regulation of SMS activity is crucial to the cell membrane fusion of envelope viruses[30-32]. Lipid rafts, enriched in sphingomyelin (SM) clusters on the plasma membrane, have essential biological functions related to membrane signaling and protein trafficking[33-34]. In addition, recent studies have reported that lipid rafts are an important location for enveloped viral infection[35]. Thus, the distribution of SM in the plasma membrane and its involvement in viral infections has attracted academic interest.

To understand the biological mechanism underlying the inhibition of SARS-CoV-2 infection by malabaricone C, we examined the distribution of SM on the plasma membrane in Vero E6 cells with EGFP-conjugated specific SM-binding proteins, NT-lysenin (NT-Lys) and equinatoxin II (EqtII) that can recognize different membrane distributions of SM. NT-Lys binds clustered SM, whereas EqtII preferentially binds dispersed SM[36-37]. As shown in Figure 4, the fluorescence intensity of EGFP-NT-Lys on the plasma membrane after treatment with malabaricone C was lower than that of the control. However, there was almost no difference in the fluorescence intensity of EqtII-EGFP between the malabaricone C treatment and the control. It was inferred that malabaricone C affected the composition of lipid rafts in the plasma membrane. Therefore, the inhibition of SARS-CoV-2 entry by malabaricone C was suggested to occur by interfering with the assembly of lipid rafts on the cell membrane.

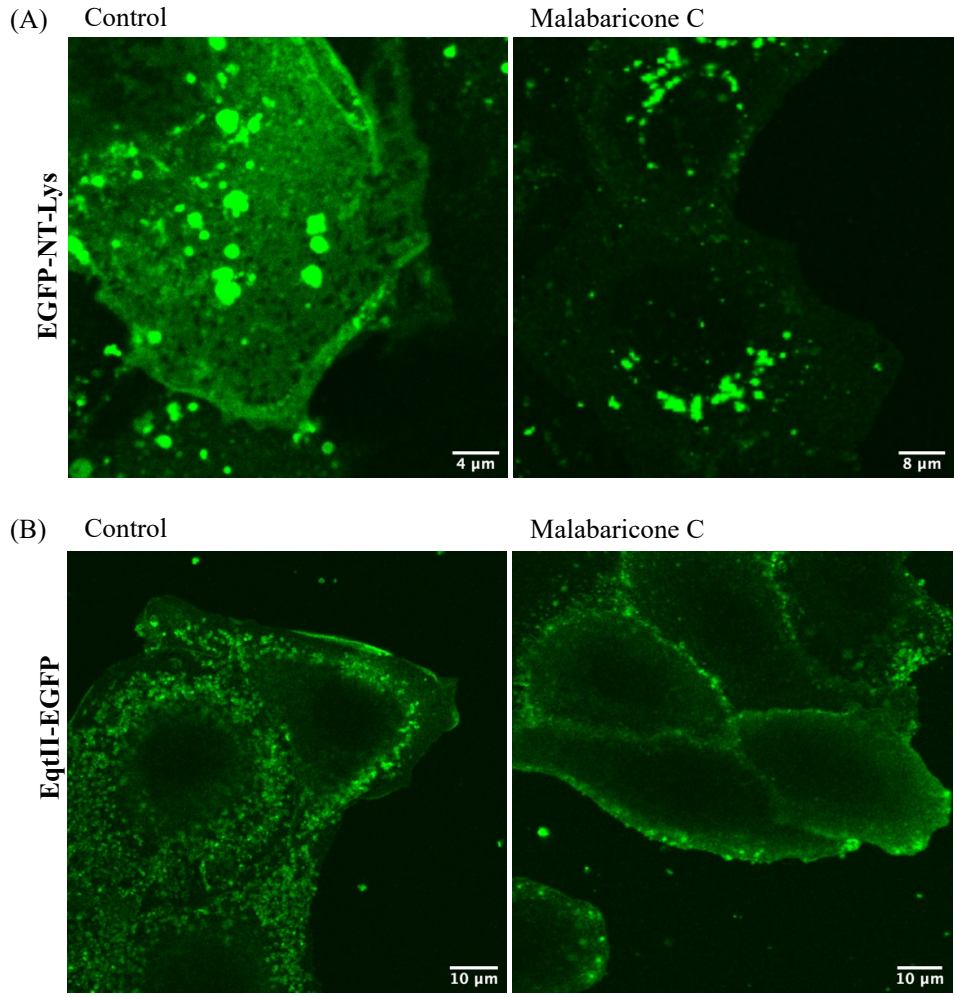

Figure 4: Sphingomyelin (SM) cluster on the plasma membrane stained by EGFP conjugated lysenin (EGFP-NT-Lys) and equinatoxin II (EqtII-EGFP). Vero E6 cells were treated with malabaricone C or DMSO (control). (A-B) Cells were fixed and incubated with EGFP-NT-Lys (A) or EqtII-EGFP (B) at 4 °C overnight and examined by confocal microscopy.

3.4. Conclusion

The molecular and cellular mechanisms of malabaricone C antiviral activity have not been completely elucidated. This study demonstrated the partial mechanism of the anti-SARS-CoV-2 activity of malabaricone via interference with lipid raft formation on the plasma membrane in Vero E6 cells. Further detailed elucidation of the mechanism is required.

3.5. Experimental Section

SMS Assay

Cell lysates were prepared: ZS/SMS1 and ZS/SMS2 cells (protein concentration 0.1 μg/μL) were diluted by Tris-buffer (pH 7.5) 20 mM and sonicated. Aliquots of the cell lysates 100 μL were added 1 μL of inhibitor of the desired concentration and incubated at 37°C. After 30 min, the solutions were added 1 μL of C6-NBD-ceramide and incubated for 3 h at 37°C. The reaction was stopped by the addition of 350 μL of MeOH/$CHCl_3$ [1/2 (v/v)]; the mixture was shaken and centrifuged (1500 rpm x 5 min). The formation of C6-NBD-sphingomyelin was quantified by determining the peak area of C6-NBD-sphingomyelin using HPLC. A reverse-phase HPLC assay using a JACSO HPLC system was developed for the quantitative analysis of the inhibitory activity. The system was equipped with a PU-2089 Plus and FP-2020 Plus set at λex = 470 nm and λem = 530 nm. A 50 x 4.6 YMC-Pack Diol-120-NP column (5-μm particle size) was used with mobile phase (IPA/hexane/water) at a flow rate of 1.0 mL/min.

ACE-2-Spike protein Interaction Inhibition Assay

Commercially-available "COVID-19 Spike-ACE2 binding assay kit II" (RayBiotech, United States, cat. no.: CoV-ACE2-2) in a 96-well plate version, the wells of which were coated with the human ACE2 protein, was used for the assay. In this assay, the total amount of human ACE2-bound RBD protein (with Fc-tag) is measured in the presence of the assayed compounds. To assess the amount of the RBD protein bound to human ACE2, a color reaction was performed using horseradish peroxidase enzyme conjugated with anti-Fc antibodies in the presence of 3,3′,5,5′-tetramethylbenzidine (TMB) substrate. The intensity of the color reaction obtained was inversely proportional to the RBD protein concentration in the wells. The experiments were carried out according to the manufacturer's instructions with slight modification. Malabaricone C derivatives were dissolved in reagent provided with the kit, namely 1x concentrated Assay Diluent. 100 μl of test compound at various concentrations (10, 1, 0.1, and 0.01 μM) mixed with the RBD protein was added to each well. The plate was then incubated overnight at 4°C with gentle shaking. After a series of washes, 100 μl of horseradish peroxidase-conjugated anti-Fc antibody solution was added and

incubated again for 1 h at room temperature with gentle shaking. After another series of washes, 100 µl of TMB One-Step Substrate Reagent was added and incubated (protected from light) for another 30 min at room temperature in the dark with gentle shaking. The reaction was stopped by adding 50 µl of Stop Solution. Immediately after stopping the reaction, the absorbance was measured (at 450 nm) using a microplate reader.

TMPRSS2 Inhibition Assay

TMPRSS2 fluorogenic assay kit (CAT # 78083, BPS Bioscience, San Diego, CA, USA) was used to evaluate the inhibition activity of the compounds on the TMPRSS2 enzyme following the supplier protocol. Briefly, 30 µL TMPRSS2 (5 ng/µL) was added to 10 µL of compound at different concentrations (100, 10, 1, 0.1, and 0.01 µM) in a black flat bottom 96-well plate. Following incubation for 30 min at room temperature, 10 µL of TMPRSS2 fluorogenic substrate (50 µM) was added, and the fluorescence intensity was measured in the dark by a microtiter plate reader at an emission and excitation wavelengths 383 and 455 nm, respectively. Camostat mesylate (10 µM, included in the assay kit) was used as a positive control, according to Hoffmann et al. (2020)[23,] while a reaction without inhibitor and enzyme was used as a negative control.

Visualization of the Distribution of Sphingomyelin

EGFP-NH-Lys and EqtII-EGFP were prepared according to the published method by Bhat, H.B, et al. [38]. Vero E6 cells were seeded at 1.0×10^4 cells density in a microplate suitable for confocal microscopy, culture at 37 °C for 24 h. The cells were washed with PBS and treated with 5 µM malabaricone C in DMEM medium supplemented with 10% FBS and 1% penicillin/streptomycin at 37 °C for 30 min. The medium was removed, and the cells were fixed in 4% paraformaldehyde in PBS at 37 °C for 2 min and continued at room temperature for 30 min in a light-shielded condition. Cells were washed with TBS three times, treated with blocking buffer (3% BSA in PBS) at room temperature for 1 h, and washed with PBS three times. Cells were then incubated with EGFP-NH-Lys (25 µg/ml) or EqtII-EGFP (25 µg/ml) at 4 °C overnight and washed

with PBS three times. After washing, the cells were observed under a confocal microscope.

3.6. References

1. Naqvi, AAT., Fatima, K., Mohammad, T., Fatima, U., Singh, IK., et al. Insight into SARA-CoV-2 Genome, Structure, Evolution, Pathogenesis and Therapies: Structural Genomic Approach, *Biochim. Biophys. Acta, Mol. Basis Dis.* **2020**, 1866, 165878.
2. Lu, R., Zhao, X., Li, J., Niu, P., Yang, B., et al. Genomic Characterissation and Epidemiology of 2019 Novel Coronavirus: Implications for Virus Origins and Receptor Binding, *The Lancet*. **2020**, 395, 565-574.
3. Li, P., Li, W., Farzan, M., Harrison, SC. Structure of SARS Coronavirus Spike Receptor-Binding Domain Complexed with Receptor, *Science*, **2005**, 309, 1864-1868.
4. Yan, R., Zhang, Y., Xia, YL., Guo, Y., Zhou, Q.. Structural Basis for the Recognition of SARS-CoV-2 by Full-length Human ACE2. *Science*, **2020**, 367,1444-1448.
5. Li, W., Moore, M., Vasilieva, N. Sui, J., Wong, SK. et al. Angiotensin-converting Enzyme 2 is a Functional Receptor for the SARS Coronavirus. *Nature*. **2003**, 426, 450–454.
6. Cheng VCC., Lau SKP., Woo PCY., Yuen KY. Severe Acute Respiratory Syndrome Coronavirus as an Agent of Emerging and Reemerging Infection. *Clin Microbiol Rev*, **2007**, 20.
7. Hoffmann, M., Weber, HK., Schroeder, S., Kruger, N., Herrler, T., et al. SARS-CoV-2 Cell Entry Depends on ACE2 and TMPRSS2 and Is Blocked by a Clinically Proven Protease Inhibitor. *Cell* **2020**, 181, 271-280.
8. Hoffman, M., Weber, HK., Pohlmann, S. A Multibasic Cleavage Site in the Spike Protein of SARS-CoV-2 is Essential for Infection of Human Lung Cells, *Mol Cell.* **2020**, 78, 779-784.
9. Xiu, S., Dick, A., Mirzaie, S., Abdi, F., Cocklin, S., et al. Inhibitor s of SARS-CoV-2 Entry: Current and Future Opportunities, *J Med Chem*, **2020**, 63, 12256-12274.

10. Ortega JT., Serrano ML., Pujol FH., Rangel HR. Role of Changes in SARS-CoV-2 Spike Protein in the Interaction with the Human ACE2 Receptor: An in Silico Analysis. *EXCLI J.* **2020**, 18, 410-417.
11. Wrapp, D., Wang, N., Corbett, KS., Goldsmith, JA, Hsieh, CL., et al. Cryo-EM Structure of the 2019-nCoV Spike in the Prefusion Conformation, *Science*, **2020**, 367, 1260-1263.
12. Shirato, K., Kawase, M., Matsuyama, S. Middle East Respiratory Syndrome Coronavirus Infection Mediated by the Transmembrane Serine Protease TMPRSS2, *J Virol*, **2013**, 87, 12552-12561.
13. Carpinteiro, A., Edwards, MJ., Hoffman, M., Kochs, G., Gripp, B., et al. Pharmacological Inhibition of Acid Sphingomyelinase Prevents Uptake of SARS-CoV-2 by Epithelial Cells, *Cell Rep Med*, **2020**, 1, 100142.
14. Ripa, I., Andreu, S., Guerrero, JAL., Morales, RB. Membrane Rafts: Portals for Viral Entry, *Front Microbiol*. **2021**, 4, 631274.
15. Sorice, M., Misasi, R., Riitano, G., Manganelli, V., Martellucci, S., et al. Targeting Lipid Rafts as a Strategy Against Coronavirus, *Front Cell Dev Biol*, **2021**, 4, 618296.
16. Shin, YH., Jeong, K., Lee, J., Lee, HJ., Yim, J., et al. Inhibition of ACE2-Spike Interaction by an ACE2 Binder Suppresses SARS-CoV-2 Entry, *Angew Chem Int Ed Engl*, **2022**, 61, 11.
17. Bojadzic, D., Alcazar, O., Buchwald, P., Methylene Blue Inhibits the SARS-CoV-2 Spike–ACE2 Protein-Protein Interaction–a Mechanism that can Contribute to its Antiviral Activity Against COVID-19, *Front. Pharmacol.* **2021**, 11.
18. Li, C., Zhou, H., Guo, L., Xie, D., He, H., et al. Potential Inhibitors for Blocking the Interaction of the Coronavirus SARS-CoV-2 Spike Protein and Its Host Cell Receptor ACE2. *J Transl Med* , 2022, 20, 314.
19. Gangadevi, S., Badavath, VN., Thakur, A., Yin, N., Jonghe, SD., et al. Kobophenol A Inhibits Binding of Host ACE2 Receptor with Spike RBD Domain of SARS-CoV-2, a Lead Compound for Blocking COVID-19, *J. Phys. Chem. Lett*. **2021**, 12, 1793–1802.

20. Yu, R., Li, P., Screening of Potential Spike Glycoprotein / ACE2 Dual Antagonists Against COVID-19 in Silico Molecular Docking, *J Viro Met*, **2022**, 301, 114424.
21. Fraser, B.J., Beldar, S., Seitova, A., Hutchinson, A., Mannar, D., et al. Structure and Activity of Human TMPRSS2 Protease Implicated in SARS-CoV-2 Activation. *Nat Chem Biol* , 18, 963–971.
22. Bojkova, D., McGreig, JE., McLaughin, KM., Masterson, SG., Widera, M., et al. SARS-CoV-2 and SARS-CoV Differ in Their Cell Tropism and Drug Sensitivity Profiles, *bioRxiv*, **2020**.
23. Hoffman, M., Winkler, HH., Smith, JC., Kruger, N., Arora, P., et al. Camostat Mesylate Inhibits SARS-CoV-2 Activation by TMPRSS2-related Protease and Its Metabolite GBPA Exerts Antiviral Activity, *EBioMed*, **2021**, 65, 103255.
24. Dai, J., Feng, Y., Liao, Y., Tan, L., Sun, Y., et al. Virus Infection and Sphingolipid Metabolism, *Antivir Res*, **2024**, 228, 105942.
25. Hannun, YA., Obeid, LM., Principles of Bioactive Lipid Signalling: Lessons from Sphingolipids, *Nat Rev Mol Cell Biol*. **2008**, 9, 139-150.
26. Wolf, JJ., Studstill, CJ., Hahm, B. Emerging Connections of S1P-Metabolizing Enzymes with Host Defense and Immunity During Virus Infections, *Viruses*, **2019**, 11, 1097.
27. Mori, Y., Sakata, M., Sakai, S., Okamoto, T., Nakatsu, Y., et al. Membrane Sphingomyelin in Host Cells Is Essential for Nucleocapsid Penetration into the Cytoplasm after Hemifusion during Rubella Virus Entry, *mBio*, **2022**, 13.
28. Yagi, M., Hama, M., Ichii, Sayaka., Nakashima, Y., et al. Sphingomyelin Synthase 1 Supports Twi Steps of Rubella Virus Life Cycle, *iScience*, **2023**, 26, 108267.
29. Taniguchi, M., Tasaki, T., Ninomiya, H., Ueda, Y., Kuremoto, KI., et al. Sphingomyelin Generated by Sphingomyelin Synthase 1 is Involved in Attachment and Infection with Japanese Encephalitis Virus, *Scientific Reports*, **2016**, 6, 37829.
30. Hayashi, Y., Sasaki, YN., Tanikawa, T., Oka, S., Tsuchiya, K., et al. Sphingomyelin Synthase 2, but Not Sphingomyelin Synthase 1, is Involved in

HIV-1 Envelope-mediated Membrane Fusion, *J Biol Chem*, **2014**, 289, 30842-30856.

31. Bienias, K.; Fiedorowicz, A.; Sadowska, A.; Prokopiuk, S.; Car, H. Regulation of Sphingomyelin Metabolism. *Pharmacol. Rep.* **2016**, *68*, 570−581.
32. Tafesse, G. F.; Sanyal, S.; Ashour, J.; Guimaraes, P. C.; Hermansson, M. *et al.* Intact sphingomyelin biosynthetic pathway is essential for intracellular transport of influenza virus glycoproteins. *Proc. Natl. Acad. Sci. USA.* **2013**, *110*, 6406–6411.
33. Simons, K.; and Ikonen, E. Functional rafts in cell membranes. *Nature*. **1997**, *387*, 569-572.
34. Lingwood, D.; and Simons, K. Lipid rafts as a membrane-organizing principle. *Science*. **2010**, *327*, 46-50.
35. Suomalainen, M. Lipid rafts and assembly of enveloped viruses. *Traffic*. **2002**, *3*, 705-709.
36. Bhat, H.B.; Kishimoto, T.; Abe, M.; Makino, A.; Inaba, T.; Murate, M.; Dohmae, N.; Kurahashi, A.; Nishibori, K.; Fujimori, F.; Greimel, P.; Ishitsuka, R.; Kobayashi, T. Binding of a pleurotolysin ortholog from Pleurotus eryngii to sphingomyelin and cholesterol-rich membrane domains. *J. Lipid Res.* **2013**, *54*, 2933-2943.
37. Makino, A.; Abe, M.; Murate, M.; Inaba, T.; Yilmaz, N.; Hullin-Matsuda, F.; Kishimoto, T.; Schieber, N.L.; Taguchi, T.; Arai, H.; Anderluh, G.; Parton, R.G.; Kobayashi, T. *FASEB J.* **2015**, *29*, 477-493.

Acknowledgement

I would like to express my sincere gratitude to my supervisor, Prof. Kenji Monde, for his significant support and insights that helped me finish this work. My heartfelt gratitude also goes to Assoc. Prof. Yuta Murai and Assoc. Prof. Tohru Taniguchi for their guidance, patience, and understanding during the years it took to complete my Ph.D. course.

I would like to express my gratitude to Prof. Akihiko Sato, Prof. Yasuyuki Igarashi, Assoc. Prof. Seigo Usuki, Assoc. Prof. Kohei Yuyama, Assoc. Prof. Akira Kitamura, and Dr. Sajeer Koolath, for their contributions to my research, as well as their experimental guidance and helpful discussions.

My appreciation also goes to the laboratory staff, Abe-san, Suga-san, and Ogura-san, for their administrative and technical work assistance during my study at Hokkaido University.

I am forever thankful for my family's unconditional love and support throughout the entire study process and every day.

Finally, I gratefully acknowledge MEXT for the financial support through the International Graduate Program. Without their funding, this work would not have been feasible.

Publications

(1)**Mutmainah**, Murai, Y., Fujimoto, A., Kawamura, R., Kitamura, A., Koolath, S., Usuki, S., Sasaki, M., Orba, Y., Igarashi, Y., Sawa, H., Sato, A., Monde, K. Malabaricone C Isolated from Edible Plants as a Potential Inhibitor of SARS-CoV-2 Infection. *Scientific Reports*. Vol XX, p.XX (**Accepted December 2024**).

(2)Taniguchi, T., **Mutmainah**, Takimoto, S., Suzuki, T., Watanabe, S., Matsuda, F., Umezawa, T., Monde, K. Scope and Limitations of Absolute Configuration Determination of Allenic Natural Products Using the C=C=C Stretching VCD Signal. *Organic & Biomolecular Chemistry*. Vol 21, p.569-574 (**2023**).

(3)Swamy, M.M.M., Zubir, M.Z.M., **Mutmaina**h, Tsuboi, S., Murai, Y., Monde, K., Hirano, K., Jin, T. A Near-infrared Fluorescent Long-chain Fatty Acid Toward Optical Imaging of Cardiac Metabolism in Living Mice. *Analyst*. Vol 147, p.4206-4212 (**2022**).